OPERATION OF INTERIOR PERMANENT MAGNET SYNCHRONOUS MACHINES WITH FRACTIONAL SLOT CONCENTRATED WINDINGS UNDER BOTH HEALTHY AND FAULTY CONDITIONS

By

Shanelle Nicole Foster

A DISSERTATION

Submitted to
Michigan State University
in partial fulfillment of the requirements
for the degree of

Electrical Engineering - Doctor of Philosophy

2013

ABSTRACT

OPERATION OF INTERIOR PERMANENT MAGNET SYNCHRONOUS MACHINES WITH FRACTIONAL SLOT CONCENTRATED WINDINGS UNDER BOTH HEALTHY AND FAULTY CONDITIONS

By

Shanelle Nicole Foster

Design for fault tolerance and early detection of insulation failure are critical for automotive and aerospace applications to ensure passenger safety. Permanent magnet machines can be designed to better withstand stator insulation failures. In this work, the performance of three fault tolerant fractional slot concentrated winding machine designs experiencing stator winding insulation failure are evaluated. Two of the machines are designed with double-layer windings and one with single-layer. The single-layer fractional slot concentrated winding design is shown most reliable; however this design has the worst torque performance. A ripple reduction control technique is developed based on an analytical description of torque. This technique is shown to improve the torque performance of the single-layer fractional slot design.

Fault tolerant design alone does not provide high reliability since thermal stress from aging, overloading, cycling or fast switching of the inverter causes most stator insulation failures. Early detection of incipient stator winding faults could avoid catastrophic machine failure, allow implementation of mitigation techniques to continue operation, reduce the occurrence of secondary faults and allow adequate time to plan maintenance. In this work, two of the machines designed were manufactured with windings that allow the introduction of faults with three severity levels and varying degrees of incipient faults. Through a parametric

identification method, the characteristic flux linkages of the machines are extracted under both healthy and faulty conditions. It is shown that incipient stator windings faults are reflected in the machine's characteristic parameters. These parametric changes are reflected in the phase voltage for current-controlled applications. Incipient stator winding faults can be detected online, if accurate knowledge of the healthy machine parameters is available.

To my husband, children, mother and brother

ACKNOWLEDGMENTS

First and foremost, I thank my Lord and Savior Jesus Christ for without Him none of this would have been possible. I'd also like to thank my husband, Kyle Foster, and my children, Shayna, Kyle, Jr. and Kailen, for their patience and forgiveness as I attempted to juggle being a wife, mother and researcher. Without your assistance, this balancing act would have been impossible. I must thank my mother, Defoird Rochelle Hogan, for being an example of strength and courage all of my life. Thank you for your prayers and encouragement over the years. Also, a big thank you to my brother, Shannon Hogan, and my cousin, Dr. Marlon Mitchell, for all the words of encouragement. I can't forget my mother-in-law, Toni Lee, my beautiful sisters-in-law, Carmen Hogan and Michelle Lee, and my God-sister, Shanequa Dennie . There are too many family members to name them all, but I love each of you and appreciate all of the support and encouragement over the years.

I'd like to thank Dr. Elias G. Strangas for his patience, guidance, support and encouragement. I'd also like to thank Dr. John Miller, Dr. Harold Schock, Dr. Bingsen Wang and Dr. George Zhu for their time and effort as part of my guidance committee.

A big thank you to present and past members of the Electrical Machines and Drives Laboratory team for all of their support. I must also thank Mrs. Meagan Kroll, Mrs. Pauline Vandyke, Mrs. Roxanne Peacock, Mr. Brian Wright, Mr. Gregg Mulder, Ms. Laurie Rashid, Ms. Jennifer Woods and Ms. Joyce Foley for their assistance.

The assistance with child care that I've received over the years has made balancing motherhood and research much easier. Thank you to Mrs. Lauren Mitchner Brown, Ms. Racheal Mitchner, Ms. Ciera Magee-Wiggins, Mrs. Jacqueies Thomas, Ms. Deanna Anderson and AppleTree Christian Learning Center for the magnificent care that you provided for my children. The peace of mind that I had when my precious children were in your care allowed me to the time to focus on my research. I also have to thank a few people for their care friendship, support and encouragement. Dr. Aurles U. Wiggins, Mrs. Jennifer Mitchner, Mrs. Jamillah Gross-Caldwell, Mr. Theodore Caldwell and Mrs. Lisa Raths you are all very special to me.

I'd also like to thank Mr. Rickey Caldwell, Ms. Lisa Henry and Mrs. Maggie Blair-Ramsey from the Diversity Programs Office, Ms. Audrey Smith and Mrs. Evette Chavez Lockhart from the MSU Women's Resource Center, Ms. Paulette Granberry Russell from the Office of Inclusion and Intercultural Initiatives, Dr. Percy Pierre and the Alfred P. Sloan Foundation for their support.

TABLE OF CONTENTS

LIST OF TABLES

LIST OF FIGURES

Chapter 1

Introduction

Permanent magnet synchronous machines are appealing for aerospace and hybrid/electric transportation applications due to their many advantages over other machine designs, such as higher efficiency, higher power density and faster dynamics in a compact package. However, permanent magnet machines are subject to electrical, magnetic and mechanical failures. These failures are a challenge because the rotating magnets cannot be turned off.

In aerospace and automotive industries a very high importance is placed on passenger safety. Machine failures in these industries put human lives at risk [1]. For this reason, high reliability and robustness are required of permanent magnet synchronous machines. Machines used in aerospace and automotive applications must have a low possibility of failure as well as continue to operate or fail safely in the event of a failure. Technology has advanced the reliability of electrical machines; however, machine failures still occur.

1.1 Objectives and Contributions

Stator winding failures are among the most common. About 35% of electrical machine failures are stator related. 70% of the stator related failures are due to failures in the insulation [2]. Low probability of stator winding failure together with the ability to continue operating if the winding insulation fails can be accomplished through fault tolerant machine design. According to [3], the turn-to-turn short-circuit in a single phase is more severe than a phase-to-phase short-circuit. For this reason, the authors conclude that a double-layer fractional slot concentrated winding permanent magnet synchronous machine design is as reliable as a single-layer. In this work, the reliability of both a double- and single-layer fractional slot concentrated winding interior permanent magnet synchronous machine is compared.

Both the double- and single-layer fractional slot concentrated winding designs options offer advantages. The primary difference is two phases share a stator slot with double-layer windings. The MMF sub-harmonics in double-layer windings typically have lower amplitude. However, in single-layer windings, the MMF consists of the main and sub-harmonics which lead to unbalanced magnetic loading of the rotor resulting in saturation, decreased average torque, unbalanced pull forces and high torque ripple. The advantage of selecting the double-layer winding design is reduced sub-harmonics and losses. Single-layer fractional slot concentrated windings provide the best isolation between phases; however, the inherent characteristics of this design negatively impact the machine performance. In this work, a control technique is developed that improves the machine performance by reducing torque ripple.

Permanent magnet synchronous machines are typically modeled in the two-axes synchronous frame of reference. DQ theory assumes sinusoidal MMF; however, the arrangement of fractional slot concentrated windings produces a non-sinusoidal MMF. According to [4], the DQ model remains reliable. Self- and cross-saturation are non-linear effects that have been proven important for development of high performance permanent magnet synchronous machine controllers. In [5], it was determined that cross-coupling is not significant in permanent magnet machines with fractional slot concentrated windings. The frozen permeability method was utilized to prove that the classical d-q model of permanent magnet synchronous machines is accurate when fractional slot concentrated windings are used. In this work, the cross-coupling parameters of both double- and single-layer fractional slot concentrated winding interior permanent magnet synchronous machines are evaluated.

The need for fail-safe operation of permanent magnet synchronous machines in applications requiring high reliability has prompted development of techniques for detecting incipient faults. Without knowledge of degrading stator winding insulation, a stator inter-turn short could develop and lead to catastrophic failure. It is desired to detect the insulation degradation during normal machine operation to avoid these failures. In this work, use of extracted machine parameters to monitor the condition of the stator winding insulation is evaluated. Degrading insulation leads to variations in the machine characteristic parameters; the flux linkages will change as the fault progresses. It is well known that the use of accurate machine parameters for control improves a machine's operating performance. Accurate knowledge of the parameters is also useful for condition monitoring.

The contributions of this work are:

- Development of an analytical expression of torque developed by permanent magnet synchronous machines with fractional slot concentrated windings, including permeance variations.

- Development of a control technique for reducing torque ripple in permanent magnet synchronous machines with fractional slot concentrated windings.

- Demonstrating that indicators of incipient stator winding faults are present in the d- and q-axis flux linkages of permanent magnet synchronous machines with fractional slot concentrated windings.

1.2 Organization

In Chapter 2 stator winding insulation stator winding insulation failure in permanent magnet synchronous machines with sinusoidally distributed windings is examined. An analytical model of a permanent magnet synchronous machine with stator winding insulation failure is presented. Additionally, a finite element model is used to evaluate the machine's performance when a turn-to-turn short-circuit is present. Chapter 3 describes techniques that are available for improving permanent magnet synchronous machine reliability. Designs for two fractional slot concentrated winding interior permanent magnet synchronous machine designs are presented in Chapter 4. One machine is designed with double-layer windings, while the other with single-layer windings. Experimental setup and characterization results are provided. Additionally, a finite element model of the fault tolerant machine designs is used to evaluate the machine characteristic inductances and machine performance under stator inter-turn failure. Chapter 5 presents an analytical description of torque including the sources of torque ripple. A technique for reducing torque ripple is presented in Chapter 6. In Chapter 7 the finite element and experimental parameters of the two fault tolerant design under incipient fault conditions. Finally, conclusions and anticipated future work are presented in Chapter 8.

Chapter 2

Stator Winding Insulation Failure

Permanent magnet machine failures include core insulation degradation, stator winding or insulation failures, electrical trips, demagnetization of the magnets, bearing failures and loss of stator/rotor mechanical integrity. Root causes of these failures have been identified as defective design/manufacturing, defective materials/components, incorrect installation/operation, ambient conditions, fatigue/stress and debris/corrosion [6].

The stator of a permanent magnet machine can experience faults in both the winding and core. Root cause analysis of failed stators has shown that thermal deterioration of the insulation, short/long term electrical stress on the insulation, mechanical stress induced by vibration of the winding, dirt or moisture contaminating the winding and manufacturing/design flaws (i.e., loose bracing for the end winding, slack in the core laminations, slot wedges and joints) lead to faults in stators [6, 7].

Stator winding failures are among the most common in electric machines [1, 6–9]. Most winding faults are caused by insulation deterioration, resulting from thermal stress due to aging, overloading or cycling. Also, demagnetization of the magnets, even partially, causes current to flow in the stator windings that exceed the ratings and degrade the winding insulation. Degradation of the insulation, as shown in Figure 2.1, could result in a turn-to-turn

Figure 2.1: Stator Winding with Damaged Insulation. (For interpretation of the references to color in this and all other figures, the reader is referred to the electronic version of this disseration.)

short-circuit which increases the current flowing in that phase and the amount of heat generated.

Turn-to-turn short-circuit faults are among the most common faults occurring in electrical machines. This fault could permanently demagnetize the magnets by producing a magnetic field intensity that exceeds the coercivity of the magnets. High temperature could increase the fault severity, leading to phase-to-phase or phase-to-ground faults. Due to heat, short-circuit faults progress quickly and can lead to a fire.

A turn-to-turn short-circuit generates a circulating current which increases temperature. The heat can lead to insulation of other turns failing, a phase-to-phase short-circuit or even phase-to-ground short circuit. The circulating current also affects the performance of the permanent magnet synchronous machine. The machine model is useful for identifying how stator turn-to-turn short circuits affect the permanent magnet synchronous machine performance.

In this chapter both an analytical model and a finite element model of permanent magnet synchronous machines with stator inter-turn faults are examined.

2.1 Analytical Model of PMSM with Stator Inter-turn Faults

Several authors have used equivalent circuit models to study the effects of inter-turn winding faults [10–12]. The equivalent circuit model of a permanent magnet synchronous machine with an inter-turn winding fault in one phase is shown in Figure 2.2. The fault is modeled as a resistance, R_f, across a portion of the series connected phase a winding. The machine equations provide an indication of how the fault affects the machine performance. Total phase a voltage, Equation (2.1), is the sum of the voltages across the healthy, v_{a1}, and faulty, v_{a2}, portions of the winding. The healthy and faulty portions of the phase are identified as a_1 and a_2, respectively. Their voltages are described in Equations (2.2) and (2.3) where $r_{s1,s2}$ are the resistances of the healthy and faulty portions of the phase a winding, i_a is the phase a current, i_f is the fault current and $\lambda_{as1,as2}$ are the flux linkages of the healthy and faulty portions of the phase a winding. Voltages of phase b and c, v_b and v_c, are described in Equations (2.4) and (2.5) where r_s is the phase resistance, i_b and i_c are the phase currents and λ_{bs} and λ_{cs} are the flux linkages. The phase back-EMFs are e_{as1}, e_{as2}, e_{bs} and e_{cs}.

$$v_a = v_{a1} + v_{a2} \tag{2.1}$$

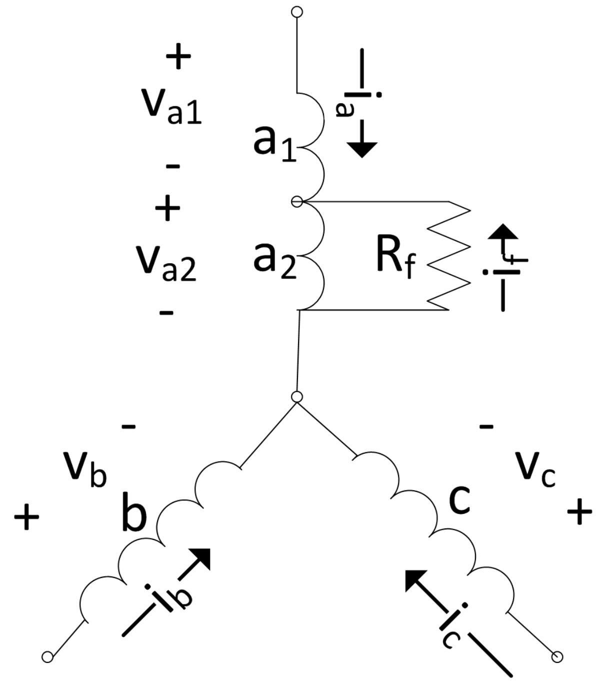

Figure 2.2: Equivalent circuit model of winding with inter-turn fault

$$v_{a1} = r_{s1} i_a + \frac{d\lambda_{as1}}{dt} + e_{as1} \tag{2.2}$$

$$v_{a2} = r_{s2}(i_a + i_f) + \frac{d\lambda_{as2}}{dt} + e_{as2} = -R_f i_f \tag{2.3}$$

$$v_b = r_s i_b + \frac{d\lambda_{bs}}{dt} + e_{bs} \tag{2.4}$$

$$v_c = r_s i_c + \frac{d\lambda_{cs}}{dt} + e_{cs} \tag{2.5}$$

Assuming that each phase has the same number of conductors, N_s and the windings are sinusoidally distributed, the MMFs for all of the phases can be described, where $N_{s,a}$, $N_{s,b}$ and $N_{s,c}$ are the number of conductors for each phase. The number of conductors involved in the fault is $N_{s,a2}$ and $N_{s,a1}$ is the number of healthy phase a conductors, ϕ_s is the stator angular displacement.

$$N_{s,a} = N_{s,b} = N_{s,c} = N_s \tag{2.6}$$

$$N_{s,a} = N_{s,a1} + N_{s,a2} = N_s \tag{2.7}$$

$$MMF_{as} = MMF_{as1} + MMF_{as2} \tag{2.8}$$

$$MMF_{as1} = \frac{N_{s,a1}}{2} i_a \cos(\phi_s) \tag{2.9}$$

$$MMF_{as2} = \frac{N_{s,a2}}{2} (i_a + i_f) \cos(\phi_s) \tag{2.10}$$

$$MMF_{bs} = \frac{N_s}{2} i_b \cos(\phi_s - \frac{2\pi}{3}) \tag{2.11}$$

$$MMF_{cs} = \frac{N_s}{2} i_c \cos(\phi_s + \frac{2\pi}{3}) \tag{2.12}$$

μ, the ratio of faulted turns to total turns, can be used to describe the number of turns involved in the fault as shown in Equations (2.13) to (2.15).

$$\mu = \frac{N_{s,a2}}{N_s} \tag{2.13}$$

$$N_{s,a2} = \mu N_s \tag{2.14}$$

$$N_{s,a1} = (1-\mu)N_s \tag{2.15}$$

The flux linkages are described in Equations (2.16) to (2.19) as functions of self and mutual inductances.

$$\lambda_{as1} = L_{a1a1}i_a + L_{a1a2}(i_a + i_f) + L_{a1b}i_b + L_{a1c}i_c \tag{2.16}$$

$$\lambda_{as2} = L_{a2a1}i_a + L_{a2a2}(i_a + i_f) + L_{a2b}i_b + L_{a2c}i_c \tag{2.17}$$

$$\lambda_{bs} = L_{ba1}i_a + L_{ba2}(i_a + i_f) + L_{bb}i_b + L_{bc}i_c \tag{2.18}$$

$$\lambda_{cs} = L_{ca1}i_a + L_{ca2}(i_a + i_f) + L_{cb}i_b + L_{cc}i_c \tag{2.19}$$

The phase back-EMFs are described in Equations (2.20) to (2.22) where λ_{pm} is the permanent magnet flux linkage, the rotor speed is ω_r and the rotor position is θ_r.

$$e_{as} = e_{as1} + e_{as2} = \omega_r \lambda_{pm} cos\theta_r \tag{2.20a}$$

$$e_{as1} = (1-\mu)\omega_r \lambda_{pm} cos\theta_r \tag{2.20b}$$

$$e_{as2} = \mu\omega_r \lambda_{pm} cos\theta_r \tag{2.20c}$$

$$e_{bs} = \omega_r \lambda_{pm} cos(\theta_r - \frac{2\pi}{3}) \quad (2.21)$$

$$e_{cs} = \omega_r \lambda_{pm} cos(\theta_r + \frac{2\pi}{3}) \quad (2.22)$$

The machine inductances can be described from the airgap flux densities.

$$B = \frac{\mu_0}{g} MMF \quad (2.23)$$

Self inductance of the healthy and faulty portions of phase a, L_{a1a1} and L_{a2a2}, are shown in Equations (2.24) and (2.25), where L_{ls} and L_m are the leakage and magnetizing inductances, respectively. The mutual inductances between the healthy and faulty portions, L_{a1a2}, of phase a is shown in Equation (2.26). Self inductance of phases b and c, L_{bb} and L_{cc}, are shown in Equation (2.27). Mutual inductances between phases b and c, L_{bc} and L_{cb}, are described in Equation (2.28). Mutual inductances between the healthy portion of phase a and the other two phases, L_{a1b} and L_{a1c}, are described in Equation (2.29). Mutual inductances between the faulty portion of phase a and the other two phases, L_{a2b} and L_{a2c}, are described in Equation (2.30).

$$L_{a1a1} = (1 - \mu)^2 (L_{ls} - L_m) \quad (2.24)$$

$$L_{a2a2} = \mu^2 (L_{ls} - L_m) \quad (2.25)$$

$$L_{a1a2} = L_{a2a1} = -\mu(1-\mu)L_m \tag{2.26}$$

$$L_{bb} = L_{cc} = L_{ls} + L_m \tag{2.27}$$

$$L_{bc} = L_{cb} = -\frac{1}{2}L_m \tag{2.28}$$

$$L_{a1b} = L_{ba1} = L_{a1c} = L_{ca1} = -\frac{1}{2}(1-\mu)L_m \tag{2.29}$$

$$L_{a2b} = L_{ba2} = L_{a2c} = L_{ca2} = -\frac{1}{2}\mu L_m \tag{2.30}$$

As shown in Equations (2.24) to (2.30), turn-to-turn faults in the stator winding will be reflected in the machine characteristic inductances. Since the flux linkages are functions of the inductances, they are also affected by turn-to-turn faults.

The open-circuit voltage of healthy permanent magnet synchronous machines is simply produced by the magnet flux. Equations (2.2) to (2.5) can be used to evaluate the open-circuit voltage for a permanent magnet synchronous machines with turn-to-turn short circuits.

$$\begin{aligned} v_{a1} &= L_{a1a2}\frac{di_f}{dt} + (1-\mu)\omega_r\lambda_{pm}cos\theta_r \\ &= -\mu(1-\mu)L_m\frac{di_f}{dt} + (1-\mu)\omega_r\lambda_{pm}cos\theta_r \end{aligned} \tag{2.31}$$

$$
\begin{aligned}
v_{a2} &= L_{a2a2}\frac{di_f}{dt} + \mu\omega_r\lambda_{pm}cos\theta_r \\
&= \mu^2(L_{ls} - L_m)\frac{di_f}{dt} + \mu\omega_r\lambda_{pm}cos\theta_r
\end{aligned}
\tag{2.32}
$$

$$
\begin{aligned}
v_b &= L_{ba2}\frac{di_f}{dt} + \omega_r\lambda_{pm}cos(\theta_r - \frac{2\pi}{3}) \\
&= -\frac{1}{2}\mu L_m\frac{di_f}{dt} + \omega_r\lambda_{pm}cos(\theta_r - \frac{2\pi}{3})
\end{aligned}
\tag{2.33}
$$

$$
\begin{aligned}
v_c &= L_{ca2}\frac{di_f}{dt} + \omega_r\lambda_{pm}cos(\theta_r + \frac{2\pi}{3}) \\
&= -\frac{1}{2}\mu L_m\frac{di_f}{dt} + \omega_r\lambda_{pm}cos(\theta_r + \frac{2\pi}{3})
\end{aligned}
\tag{2.34}
$$

The circulating current, due to the turn-to-turn short-circuit, affects the open-circuit voltage as shown in Equations (2.31) to (2.34). Evaluation of the equations indicates that this effect can be minimized by reducing the mutual inductance.

The machine torque can be evaluated through the energy stored in the coupling field. Assuming a linear magnetic system, the energy stored in the coupling field is described in Equation (2.35).

$$
\begin{aligned}
W_f = &\frac{1}{2}L_{a1a1}{i_a}^2 + L_{a1a2}i_a(i_a + i_f) + \frac{1}{2}L_{a2a2}(i_a + i_f)^2 \\
&+ L_{a1b}i_ai_b + L_{a2b}(i_a + i_f)i_b + \frac{1}{2}L_{bb}{i_b}^2 \\
&+ L_{a1c}i_ai_c + L_{a2c}(i_a + i_f)i_c + L_{bc}i_bi_c + \frac{1}{2}L_{cc}{i_c}^2
\end{aligned}
\tag{2.35}
$$

The machine torque can be calculated by Equation (2.36). The circulating current also affects the machine torque.

$$T = p\frac{\partial W_f}{\partial \theta_r} \tag{2.36}$$

2.2 Finite Element Model of PMSM with Stator Inter-turn Faults

The effects of stator inter-turn faults, described analytically in Section 2.1 can be verified through finite element analysis. A 2 slot per pole per phase PMSM with sinusoially distributed windings was modeled in finite element. Design parameters for the model are provided in Table 2.1. The geometry of both the healthy and faulty cases are shown in Figure 2.3. The red regions in the stator slots of Figure 2.3b, represent the turns involved in the short-circuit. The primary difference between the two models is the circuit, shown in Figure 2.4. The circuit for the faulty model has two additional coil conductors in the phase where the fault is introduced. One of the additional coil conductors has a resistor connected in parallel to simulate the fault severity. The region associated with this coil conductor is red in Figure 2.3b. The other coil conductor simulates the healthy turns of the faulty phase that share the slot with faulted turns.

The torque due to the interaction between the permanent magnets in the rotor and the stator slots, or cogging torque, was evaluated using finite element. The cogging torque is shown in Figure 2.5.

The open-circuit voltage for the healthy machine model is shown in Figure 2.6. The faulty machine model is used to evaluate the open-circuit voltage for different number of

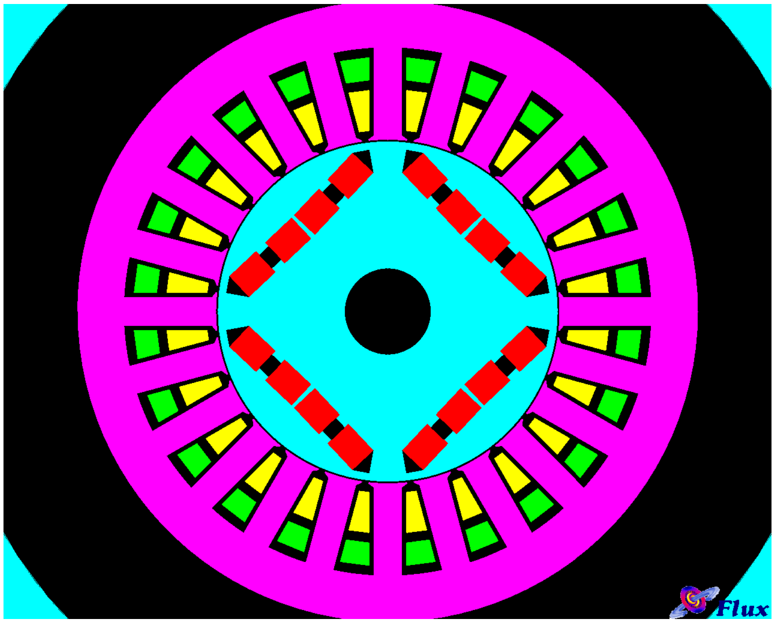

(a) Healthy

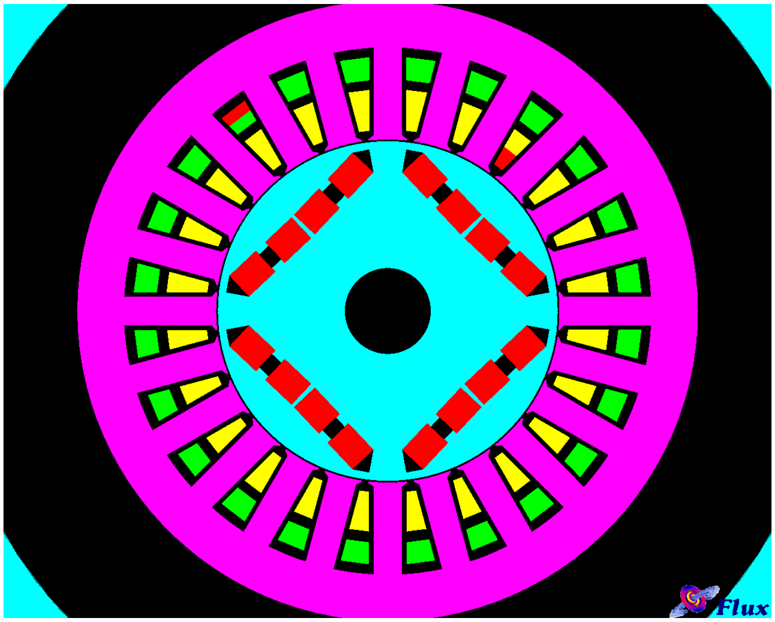

(b) Faulty

Figure 2.3: FEA geometry of PMSM with 2 slots per pole per phase:(a)healthy (b)faulty.

Number of stator slots	24
Number of poles	4
Coil Pitch	150°(5 slots)
Number of turns per coil	32
Number of turns per slot	64
Stack Length	$72mm$
Maximum Current	$18Arms$
Stator Line Voltage	$480V$
Maximum Power	$10kW$

Table 2.1: Design Parameters of PMSM modeled in FEA

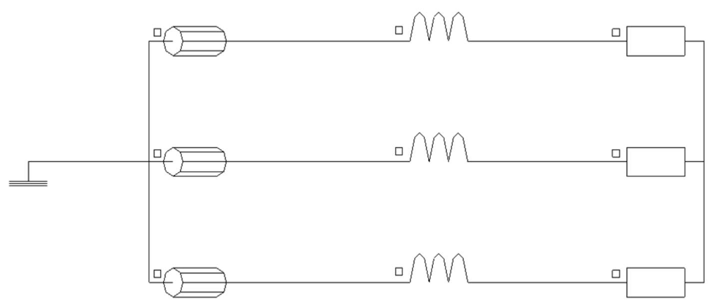

(a) Healthy

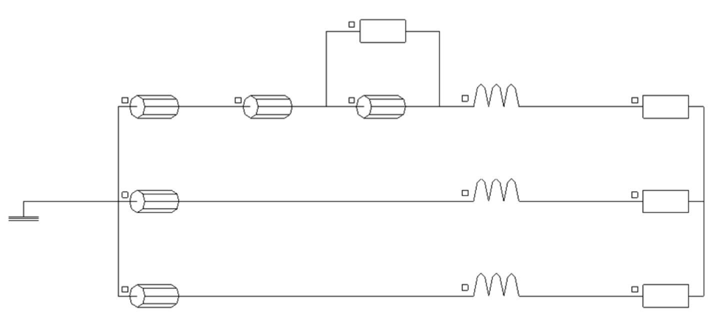

(b) Faulty

Figure 2.4: FEA circuit model of PMSM with 2 slots per pole per phase:(a)healthy (b)faulty

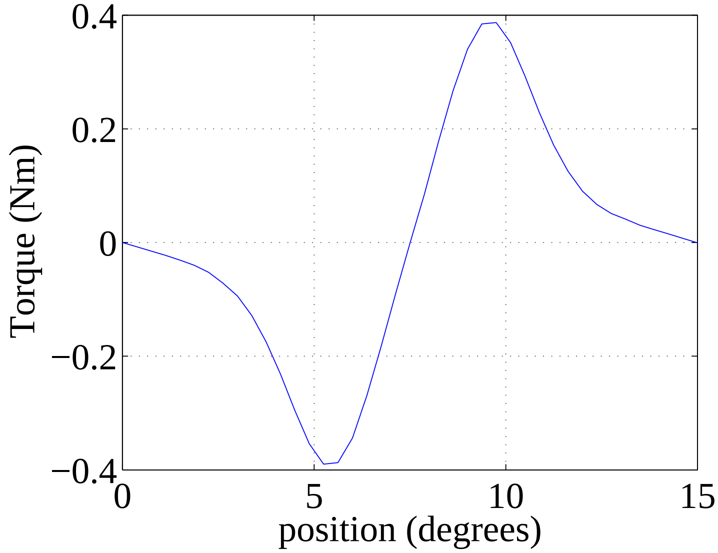

Figure 2.5: Cogging Torque of Healthy PMSM with 2 slots per pole per phase (finite element results)

turns involved in the slot. The effect of the short-circuited turns is apparent in the open-circuit voltage, as expected from Equations (2.31) to (2.34). The open-circuit voltage of the faulty machine with a short-circuit involving a single-turn, 10% of the turns in the slot and 20% of the turns in the slot are shown in Figures 2.7 to 2.9. This effect is due to the current circulating in the shorted turns, shown in Figures 2.10 to 2.12. The circulating current is more than 9 times higher than the motor's maximum current given in Table 2.1, in each case. Torque ripple also increases as the number of turns involved in the short-circuit increases, as summarized in Table 2.2.

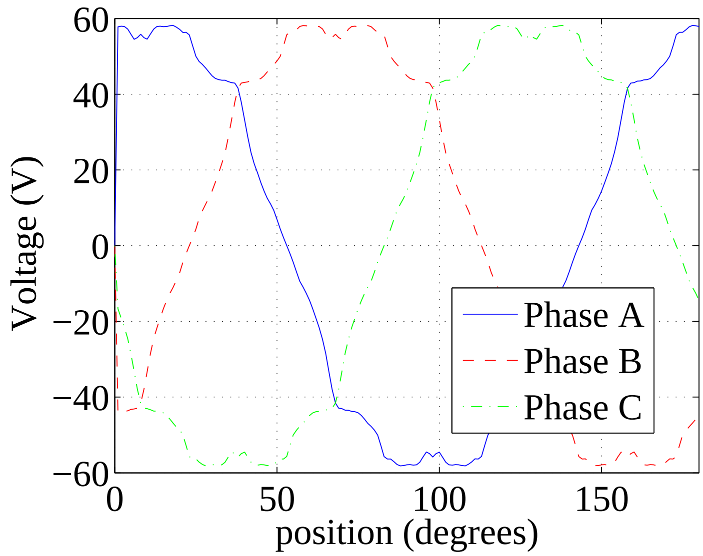

Figure 2.6: Healthy back-EMF of PMSM with 2 slots per pole per phase (finite element results)

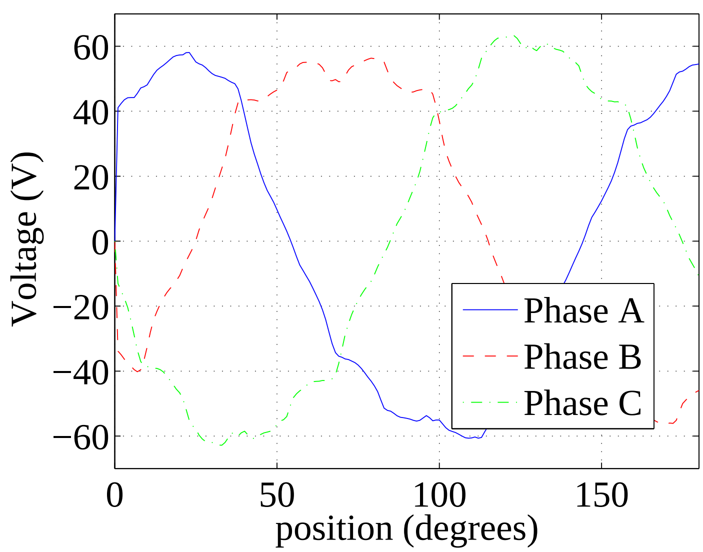

Figure 2.7: Back-EMF of PMSM with 2 slots per pole per phase and a single turn in a slot short-circuited (finite element results)

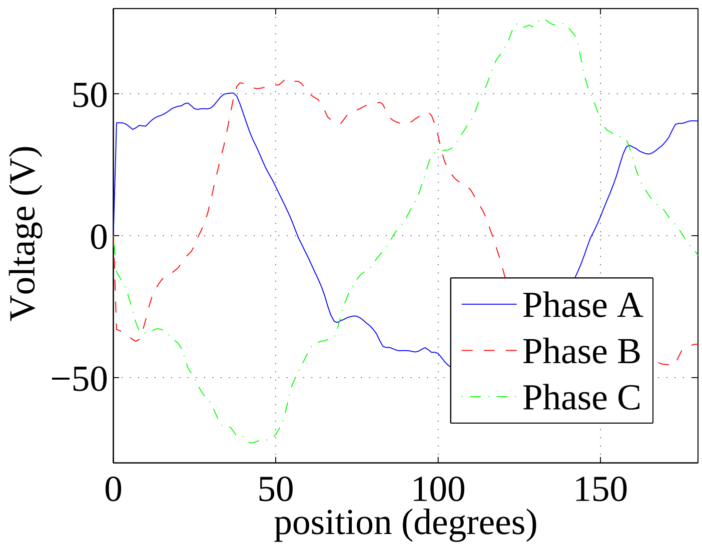

Figure 2.8: Back-EMF of PMSM with 2 slots per pole per phase and 10% of turns in a slot short-circuited (finite element results)

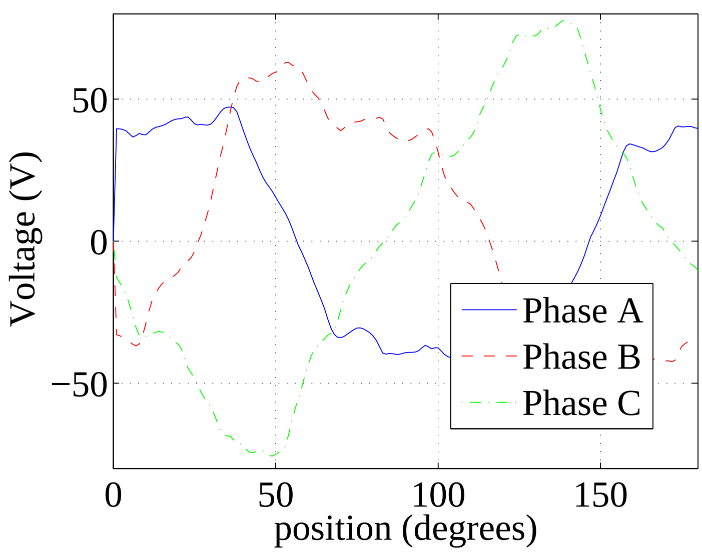

Figure 2.9: Back-EMF of PMSM with 2 slots per pole per phase and 20% of turns in a slot short-circuited (finite element results)

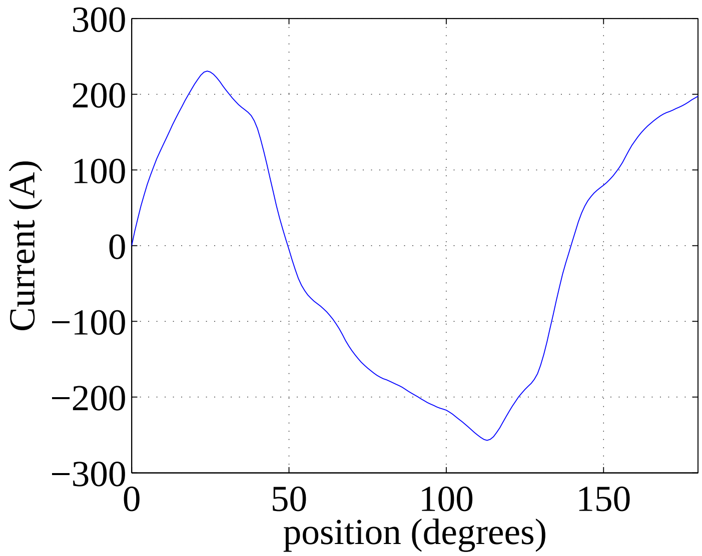

Figure 2.10: Circulating current due to a single turn in a slot involved in a short-circuit (finite element results)

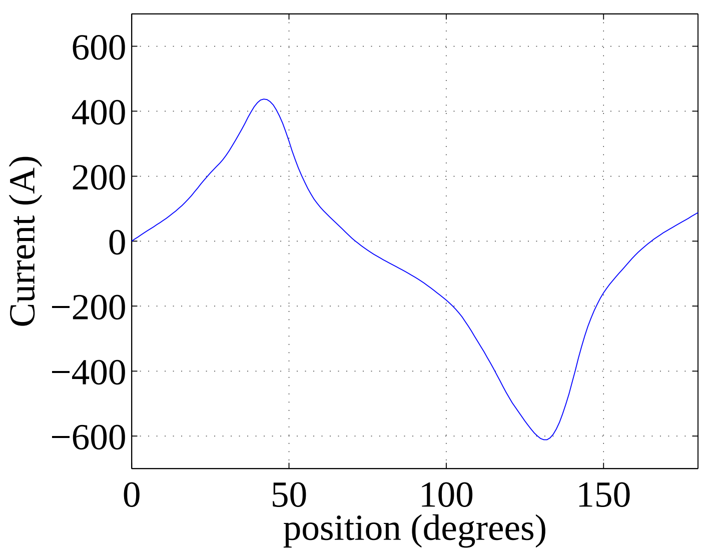

Figure 2.11: Circulating current due to a 10% of the turns in a slot involved in a short-circuit (finite element results)

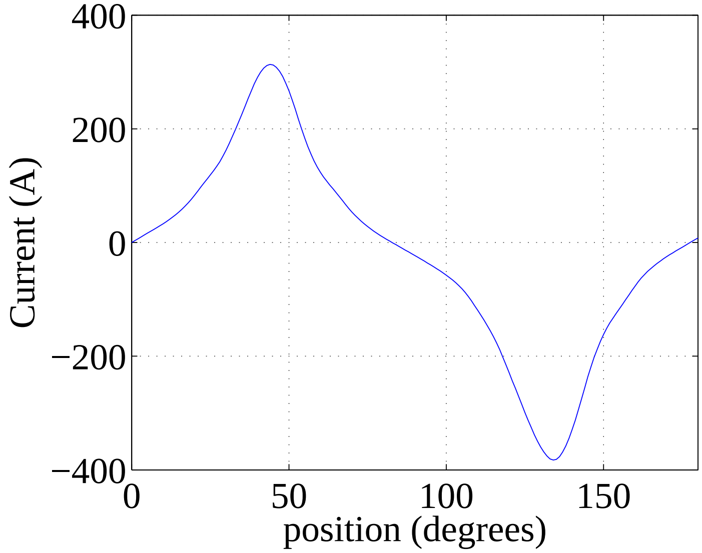

Figure 2.12: Circulating current due to 20% of the turns in a slot involved in a short-circuit (finite element results)

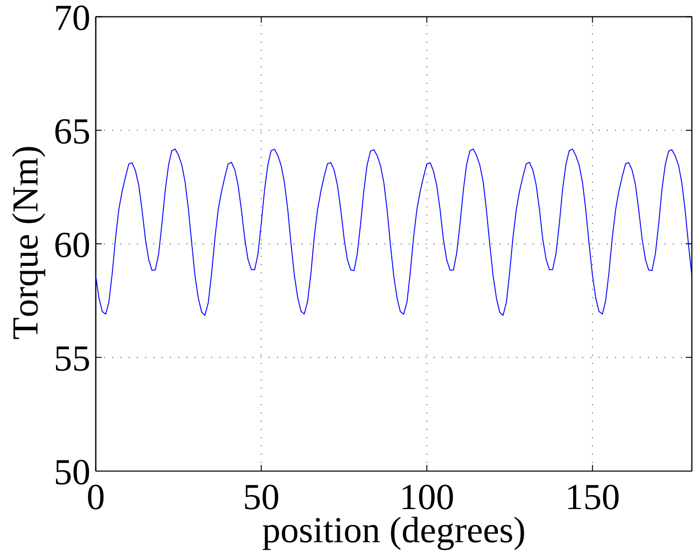

Figure 2.13: Torque of healthy PMSM with 2 slots per pole per phase (finite element results)

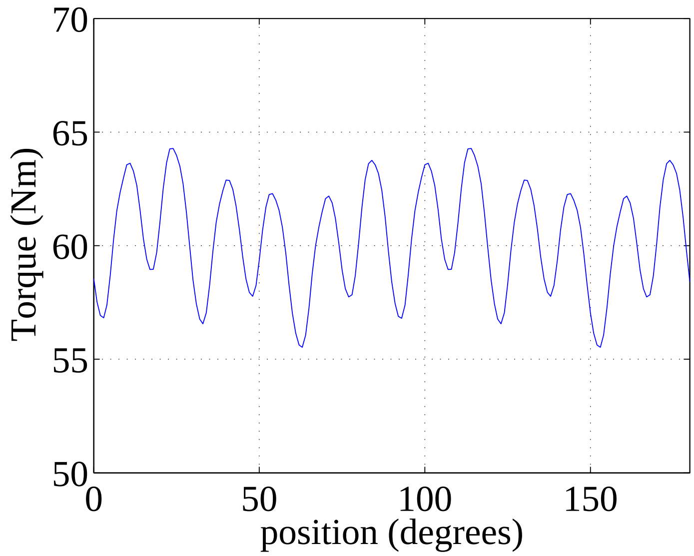

Figure 2.14: Torque of 2 slots per pole per phase PMSM with a single turn in a slot short-circuited (finite element results)

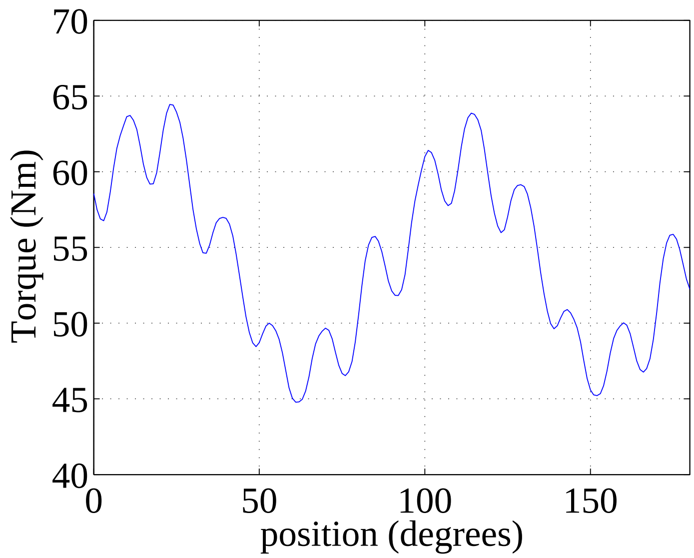

Figure 2.15: Torque of 2 slots per pole per phase PMSM with 10% of turns in a slot short-circuited (finite element results)

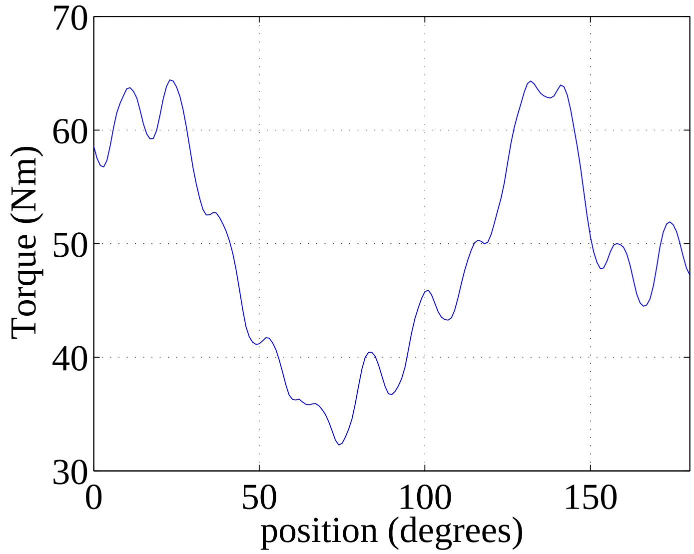

Figure 2.16: Torque of 2 slots per pole per phase PMSM with 20% of turns in a slot short-circuited (finite element results)

Machine Condition	Circulating Current	Torque Ripple
Healthy		11.99%
Single-Turn	$163.61A_{rms}$	14.33%
10% Turns	$273.61A_{rms}$	32.21%
20% Turns	$174.75A_{rms}$	52.65%

Table 2.2: Circulating current in a PMSM designed with sinusoidally distributed windings under short-circuit faults. Torque ripple as a percentage of the average torque in a healthy machine.

Chapter 3

PMSM Reliability

One approach to improving machine reliability is through design. Permanent magnet synchronous machines can be designed to better tolerate stator winding inter-turn short-circuits. Machines designed to tolerate failures are called fault tolerant machines. However, designing for fault tolerance alone will not provide the desired level of reliability for ensuring passenger safety. Accurate detection and diagnosis of a pending fault would provide an additional level of reliability.

This chapter introduces available techniques for improving reliability through design and fault detection.

3.1 Fault Tolerant Design

Stator inter-turn short-circuits in permanent magnet machines can experience high values of circulating currents in the shorted turns magnitudes above the machine rated current. The circulating current results in higher temperatures. In [7] the authors state that the winding degrades twice as fast as under normal operating conditions for every $10°C$ above the insulation rated temperature. With increased winding temperature a turn-to-turn short circuit may advance to include additional turns or even lead to a secondary fault, i.e., phase-to-phase short, phase-to-ground short or even demagnetization.

The authors of [13] identify requirements for fault tolerant permanent magnet synchronous machines. The requirements include considerations for:

1. Number of phases
2. Limiting of fault currents
3. Magnetic isolation between phases
4. Thermal isolation between phases
5. Physical isolation between phases

The first requirement listed, increasing the number of phases, reduces the fault current by minimizing the coupling between the magnet flux and stator windings. Meeting the second requirement reduces the effect that an inter-turn short-circuit has on the open-circuit voltage and torque. According to [14], using additional phases provides a few benefits.

- Lower amplitude of torque pulsations
- Lower stator current per phase without increasing the voltage per phase
- Higher torque per amp for the same volume machine

However, machines with more than three phases are overrated to provide the desired operation in case of failure, in which case the failed phase is disconnected. The tradeoff for complexity, F, is a function of the number of phases, m, as shown in Equation (3.1). [15].

$$F = \frac{m}{m-1} \tag{3.1}$$

The fault tolerance of permanent magnet machines with more than three phases has been demonstrated by several researchers [14–20]; however, these machines are more complex to control and require additional power electronic components. Machine reliability is high priority for aerospace and automotive applications; however, cost of manufacturing is also a priority. The cost associated with the complexity may not be as appealing for mass production in these industries.

In [13,21], inter-turn short-circuits sharing a stator slot were examined. It was determined that the circulating current opposes the air-gap flux and increases the slot leakage flux in [21]. The authors show that by modifying the stator tooth shape, the slot leakage inductance increases resulting in reduced short-circuit current. Stator winding configuration also affects the phase inductance and can be used to effectively limit the short-circuit current.

3.2 Stator Winding Configurations

There are two categories of stator winding configurations: overlapping and non-overlapping end-windings [22], shown in Figures 3.1 and 3.2, respectively. The categories are distinguished by the end-windings. Windings in the overlapping end-windings category have different phases in close proximity of each other; the configurations are distributed or concentrated. Distributed windings, shown in Figure 3.1a are arranged to produce a sinusoidal MMF. Concentrated windings, shown in Figure 3.1b are wrapped around a tooth. In this category, concentrated windings have 1 slot per pole per phase.

Windings in the non-overlapping end-windings category are arranged such that different

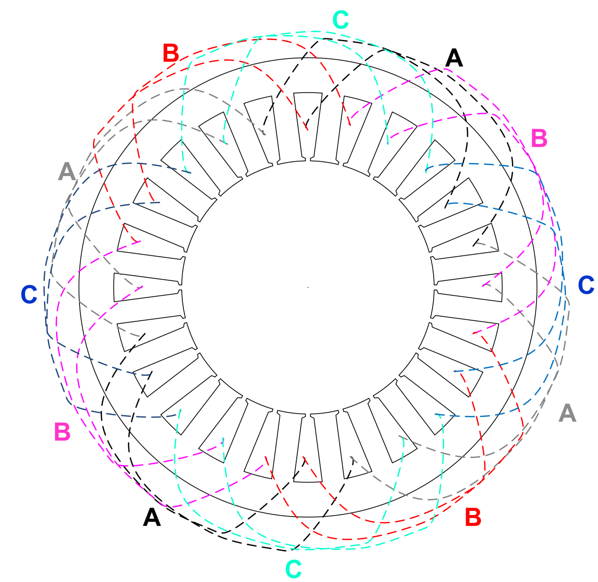

(a) Distributed

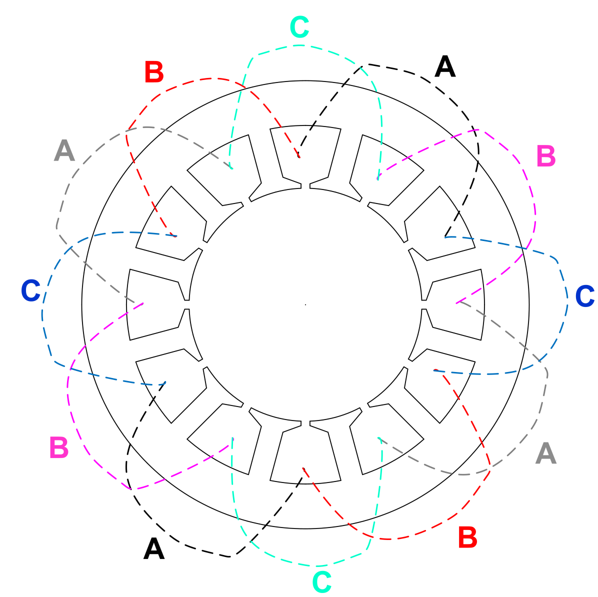

(b) Concentrated

Figure 3.1: Overlapping Winding Category - (a)Distributed and (b)Concentrated

phases do not touch. This winding configuration has less than one slot per pole per phase and is called fractional slot concentrated windings. The configurations are concentrated, wrapped around a single tooth, and are arranged as either double- or single-layer. In the double-layer windings, every tooth is wound, as shown in Figure 3.2a. Single-layer windings have every other tooth wound, as shown in Figure 3.2b.

The characteristics of fractional slot concentrated winding machines make them a viable solution for applications requiring fault tolerance [23]. Designs with fractional slot concentrated windings provide magnetic, thermal and physical separation of phases.Single-layer windings eliminate the possibility of overlapping between end windings of different phases. This lends to low mutual coupling between phases and provide better thermal isolation since different phases do not share stator slots. The low mutual coupling indicates that the short circuit current in one phase will not affect the other phases.

3.3 Effects of Winding Configurations

The MMF of permanent magnet synchronous motors with different winding configurations are shown in Figures 3.3a and 3.3b. Due to the arrangement of the windings, the overlapped distributed windings, shown in Figure 3.1a, produce a nearly sinusoidal MMF as shown in Figure 3.3a. The arrangement of the non-overlapped double-layer windings, shown in Figure 3.2a, produces a less sinusoidal MMF as shown in Figure 3.3b. The fractional slot concentrated winding MMF contains extra harmonic components when compared to an integral slot distributed winding, as shown in Figure 3.4. The MMF harmonics also create flux in the machine that induce voltages at fundamental frequency in the windings.

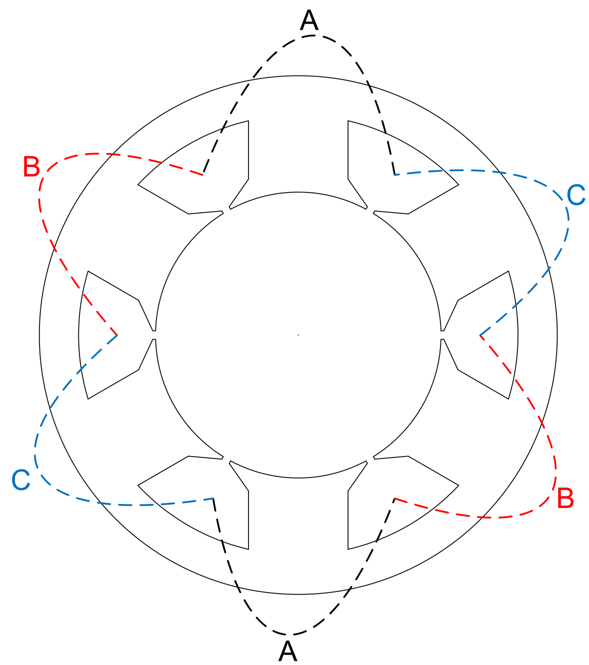

(a) Double-layer

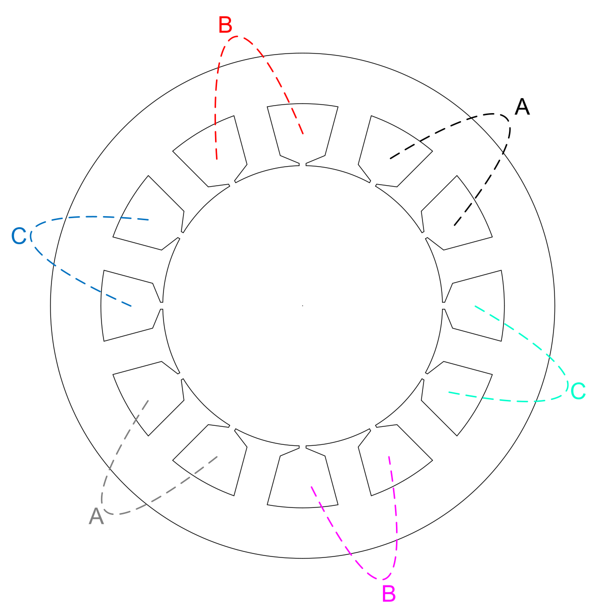

(b) Single-layer

Figure 3.2: Non-overlapping Winding Category - (a)Double-layer and (b)Single-layer

As with conventional machine analysis, the winding function can be used to calculate the self and mutual inductances of fractional slot concentrated windings; however, the effect of the harmonics must be considered. In [24] it is stated that in fractional slot concentrated winding machines saturation influences both the d-and q-axis inductance more than in distributed windings. It is also noted that higher order harmonics in the mutual inductance affect saliency. In [25], there are four components of leakage inductance, L_σ, presented that should be considered when evaluating winding configurations. Equation (3.2) describes the total leakage inductance due to the winding configuration.

1. Airgap leakage inductance, L_δ
2. Slot leakage inductance, L_u
3. Tooth-tip leakage inductance, L_t
4. End winding leakage inductance, L_w

$$L_\sigma = L_\delta + L_u + L_t + L_w \tag{3.2}$$

The airgap leakage component is described in Equation (3.3) is a function of the machine geometry. The permeability of air, μ_0, the number of phases, m, the effective airgap length, δ, the machine diameter, D, the effective core length, l', and the slot permeance factor, λ_u are all used to calculate the airgap leakage component.

$$L_\delta = \frac{\mu_0 m}{\pi \delta} D l' \left(\frac{N}{p}\right)^2 \sum_{\nu \neq 1}^{\infty} \left(\frac{k_w \nu}{\nu}\right)^2 \tag{3.3}$$

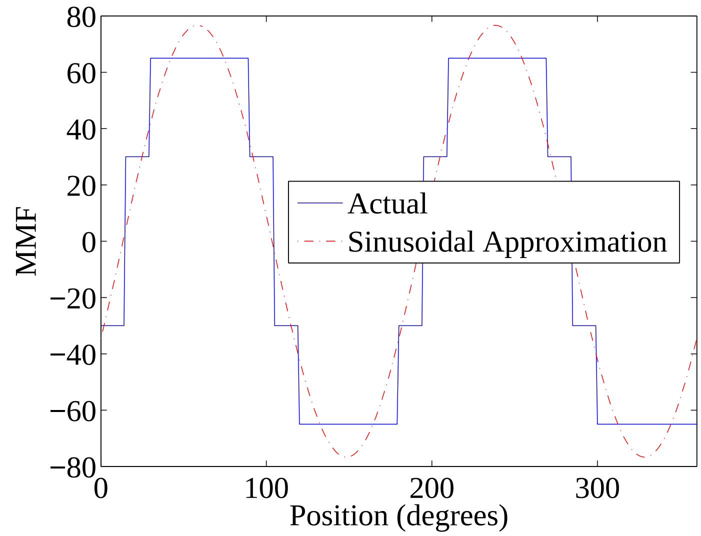

(a) Distributed Winding

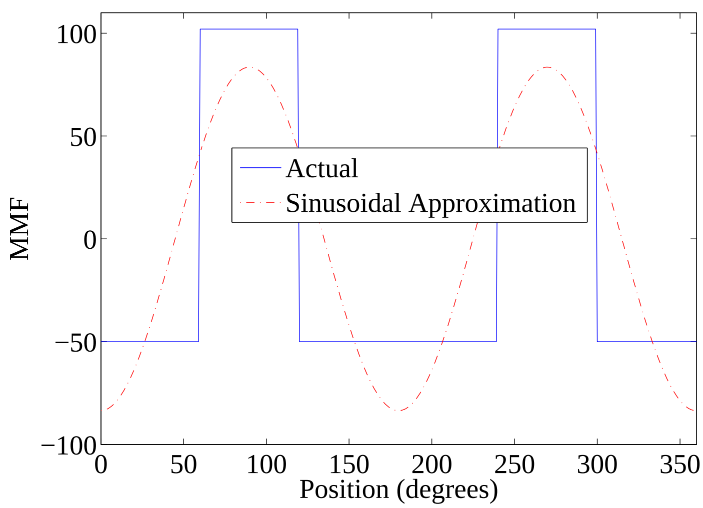

(b) Fractional Slot Concentrated Winding

Figure 3.3: MMF of different winding configurations - (a)Distributed windings with 2 SPP and (b)Fractional Slot Concentrated Windings with $\frac{1}{2}SPP$

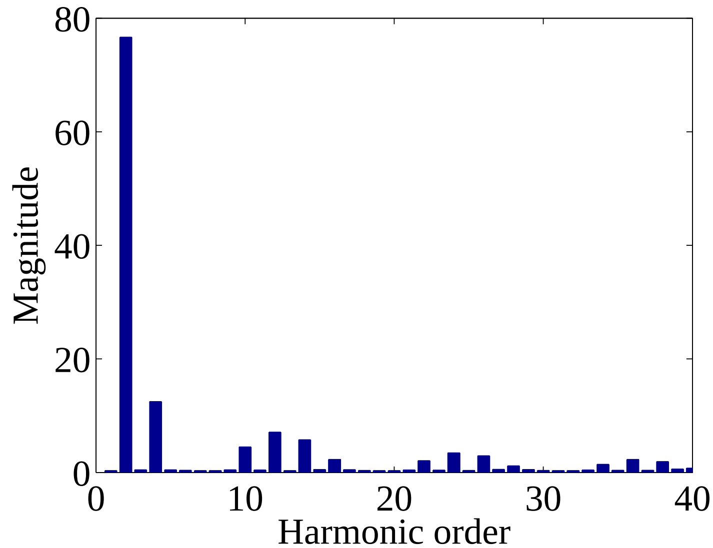

(a) Distributed Winding

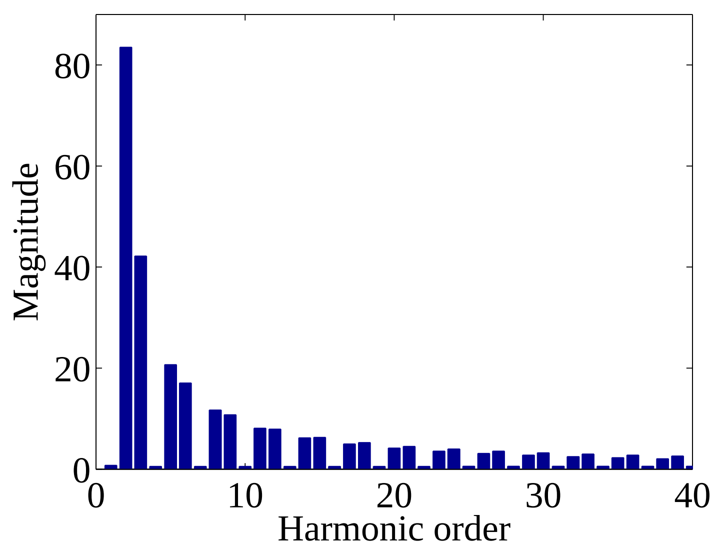

(b) Fractional Slot Concentrated Winding

Figure 3.4: MMF harmonic spectrum of different winding configurations - (a)Distributed windings with 2 SPP and (b)Fractional Slot Concentrated Windings with $\frac{1}{2}SPP$

The slot leakage inductance, in Equation (3.4) is significantly higher in fractional slot concentrated winding machines when compared to machines with distributed windings [26]. For this reason, an accurate estimation of the slot leakage inductance is suggested, including mutual slot leakage for double-layer windings.

$$L_u = \frac{4m}{Q}\mu_0 l' N^2 \lambda_u \tag{3.4}$$

According to [26], the tooth-tip, in Equation (3.5), and end leakage, in Equation (3.6) inductances are negligible.

$$L_t = \frac{4m}{Q}\mu_0 l' \lambda_d N^2 \tag{3.5}$$

$$L_w = \frac{4m}{Q} q N^2 \mu_0 l_w \lambda_w \tag{3.6}$$

As described in [27], joule loss for one phase, shown in Equation (3.7), is a function of the average conductor length, L_c, the slot fill factor, c_f, and the winding factor, k_w. Fractional slot concentrated windings can also have a low winding factor which leads to higher heat generation, iron saturation and lower efficiency.

$$P_{winding} = \frac{L_c}{c_f {K_w}^2} \tag{3.7}$$

The MMF harmonics that are asynchronous with the rotor, $\nu \neq p$, induce current in the rotor. In [28], it is stated that due to the higher wavelength of subharmonics, the flux lines enter deeply in the rotor, implying that subharmonics lead to higher rotor loss. The subharmonics also lead to an increased torque ripple, as concluded in [29].

Several authors have presented design techniques for reducing losses and torque ripple. The authors of [30] demonstrate in finite element that by using a different number of turns for each coils side and adding flux barriers to the back iron of every other slot the magnet and iron loss associated with fractional slot concentrated windings is reduced. In [31], two stators with the same slot per pole per phase combination shifted by an electrical angle will cancel harmonics that contribute to rotor loss. The authors of [32] develop an analytical expression of torque neglecting permeance variations. They conclude that selecting stator windings with an odd number of slots per pole pair reduces the torque ripple. In [33], the torque expression developed in [32] is used to demonstrate the the number of stator and rotor slots used in the machine design affect the losses and torque ripple. The authors of [34] add slits on the q-axis of the rotor surface and modify the stator tooth face to reduce the torque harmonics. The addition of flux barriers and stators provide for more complex manufacturing.

The MMF harmonics of fractional slot concentrated windings contribute extra stator leakage inductance; this however, may be helpful in reducing current for field weakening and reducing short-circuit current. As presented in [35], a fault tolerant PMSM design should have high magnetizing inductance to limit short-circuit current. Fractional slot concentrated windings offer other advantages.

- A reduction in the volume of copper in the end region
- A reduction of the joule loss in the end region due to the shorter end turns
- Reduced mutual coupling between the phases because no tooth carries coils for more

than one phase

- Higher slot fill factor
- Reduced cost because the manufacturing is simplified
- Lower cogging torque, due to the higher cogging torque frequency, f_c

The cogging torque frequency is described as frequency, f, multiplied by the least common multiple of the number of poles, where p is the number of pole pairs, and the number of stator slots, Q, as shown in Equation (3.8). Higher cogging frequency yields lower cogging amplitude.

$$f_c = LCM(2p, Q)f \tag{3.8}$$

3.4 Stator Winding Failure Detection

Machine reliability can also be improved through accurate detection and diagnosis of pending stator winding inter-turn faults. Stator winding inter-turn faults lead to unbalanced air gap voltages and line currents, increased torque pulsations, decreased average torque, increased losses, reduced efficiency and excessive heating. Stator inter-turn faults are effectively imbalances reflected in signals. However, these signals may be stationary, cyclostationary, non-stationary or even buried in a machine-borne noise.

Condition monitoring is a means of measuring signals and through analysis extract a detection and diagnosis of a fault. Techniques have been developed to diagnose faults from various measured signals, including stray flux, air gap flux, rotor field voltage, torque and stator current. These techniques can be separated into two categories: 1) intrusive and 2) non-intrusive. Intrusive techniques require additional equipment whereas non-intrusive techniques do not. The goal of condition monitoring is to diagnose the machine with minimal measurements. Inter-turn short-circuits can be detected in torque, air-gap flux and stator currents, to name a few.

The voltage reference has been used as a fault indicator. A turn-to-turn fault in one winding has been shown to reduce the number of effective turns in that winding. This parametric variation is reflected at the voltage references. The difference between the non-fault and fault voltage references indicates a fault when the preset threshold is exceeded. The fault estimation threshold may vary since the voltage reference is speed and load dependent [36].

The negative-sequence voltage component has also been used to diagnose stator winding faults. One disadvantage is the zero-sequence voltage component measurement requires access to the machine neutral [37].

Stator turn-to-turn faults can increase slot leakage flux and decrease the main air gap flux [37]. The torque is also affected by the increased slot leakage flux [21]. In reference [38] the permeance network is used to identify the inductances of a surface mounted permanent magnet machine, including the effects of saturation and leakage. The authors validate their results through comparison to finite element analysis finding good accuracy for use in a machine model. Under fault, the inductances are no longer only functions of the number of turns and slot geometry but dependent on the location of the fault in the slot [39].

Machine parameters have been used in [40–42] to detect inter-turn short circuit faults. In [40] the authors present a scheme for estimating the winding resistance and rotor flux linkages by injecting a short pulse in the d-axis current. The authors validate that their method can detect changes in the winding resistance due to heat; however, state that the scheme is suitable for monitoring non-salient pole permanent magnet synchronous machines. In [41] the recursive least squares algorithm and the Extended Park model are used to estimate the machine parameters. The authors show that winding short circuit faults can be detected through variations in the estimated parameters. The parametric variations indicate the number of turns involved in the short circuit. In [42], a parametric model of a 5-phase permanent magnet machine is used to detect winding short circuit faults from the second-order harmonic of the q-axis current. The authors of [41, 42] both validate their methods through simulation for short-circuit winding faults.

The time between a single inter-turn short circuit and catastrophic failure of the machine is short. Catastrophic permanent magnet machine failure can be avoided if a degrading stator winding insulation was detected during normal operation. Detecting the degradation prior to the existence of a turn-to-turn short circuit would allow for timely maintenance and repair.

Chapter 4

Design and Analysis of Fault Tolerant Machines

Challenges with fractional slot concentrated windings include high harmonic content in the MMF distribution, the production of losses in the rotor, unbalanced saturation that leads to torque ripple, high slot leakage inductance and high acoustic noise for some slot/pole combinations. It is shown in [35] that through careful selection of the slot/pole combination the rotor losses, torque ripple and acoustic noise can be reduced.

The most common slot per pole per phase selections are $\frac{1}{2}$ and $\frac{2}{5}$. According to [11], $\frac{1}{2}$ slot per pole per phase is a good selection for reduced rotor losses in both double and single-layer windings. However, $\frac{1}{2}$ slot per pole per phase machines may have high torque ripple. $\frac{2}{5}$ slot per pole per phase machines may have lower cogging torque and torque ripple.

In this chapter two fractional slot concentrated winding interior permanent magnet machines are designed with the most common slot per pole per phase selections, $\frac{1}{2}$ and $\frac{2}{5}$. The $\frac{1}{2}$ slot per pole per phase machine is designed with double-layer windings and the $\frac{2}{5}$ slot per pole per phase with single-layer windings. Experimental characterization and finite element results are presented for both machines. It is shown through finite element analysis that single-layer fractional slot concentrated windings with null mutual inductance provide highest reliability at the cost of machine torque performance.

4.1 Tools

4.1.1 Star of Slots Theory

The star of slots theory presented by Bianchi [35] is a tool used to design permanent magnet machines with fractional slot concentrated windings and evaluate the machine performance. The star of slots is a complex representation of the main EMF harmonic induced in the coil side of each slot of the machine, drawn only for the left-hand coil sides. The machine periodicity, t, is the greatest common divisor of the number of stator slots, Q, and the number of pole pairs, p, as shown in Equation (4.1).

$$t = GCD(Q, p) \tag{4.1}$$

$\frac{Q}{t}$ spokes form the star of slots and each spoke contains t phasors. Equation (4.2) is used to examine the feasibility of a certain slot/pole combination. The winding is considered feasible if the number of spokes per phase, q_{ph}, is an integer. The number of spokes is determined by the number of stator slots divided by the product of the number of phases, m, and the machine periodicity.

$$q_{ph} = \frac{Q}{mt} \in N \tag{4.2}$$

The angle between the phasors of adjacent slots, α_s^e, is the electrical angle in Equation (4.3). The angle between adjacent spokes, α_{ph}, is the electrical angle in Equation (4.4). A phase contains the phasors of opposite sectors each covering $\frac{\pi}{m}$ radians, rotate both sectors by $\frac{2\pi}{m}$ radians to identify other phases.

$$\alpha_s^e = \frac{2\pi p}{Q} \tag{4.3}$$

$$\alpha_{ph} = \frac{2\pi t}{Q} \tag{4.4}$$

The star of slots can also be used to analyze the harmonic content of the EMF waveform and the air-gap MMF distribution. If $\frac{Q}{t}$ is even, the main winding distribution will only include harmonics of odd order; however, if $\frac{Q}{t}$ is odd, the main winding distribution will include both even and odd order harmonics. Additionally, if the number of spokes per phase is even, there is an even number of EMF phasors to sum and the main distribution factor, k_d, is found by Equation (4.5). If the number of spokes per phase is odd, the distribution is given by Equation (4.6).

$$k_d = \frac{\sin\left(\frac{\pi}{2m}\right)}{\frac{q_{ph}}{2}\sin\left(\frac{\alpha_{ph}}{2}\right)} \tag{4.5}$$

$$k_d = \frac{\sin\left(\frac{\pi}{2m}\right)}{q_{ph}\sin\left(\frac{\alpha_{ph}}{4}\right)} \tag{4.6}$$

The coil span angle, σ_w, and pitch factor, k_p, are described by Equations (4.7) and (4.8), respectively.

$$\sigma_w = \frac{2\pi p y_q}{Q} \tag{4.7}$$

$$k_p = \sin\left(\frac{\sigma_w}{2}\right) \tag{4.8}$$

The main winding factor, k_w, is given by Equation (4.9).

$$k_w = k_d k_p \tag{4.9}$$

A high winding factor does not guarantee desirable machine performance because if all coil sides of one phase are on the same side of the machine, the winding will produce unwanted unbalanced magnetic pull resulting in noise.

The star of slots theory also provides a means of transforming a double-layer winding to single-layer and evaluating its performance, simply by removing all of the even phasors from the star of slots; however, there are a few constraints, both geometrical and electrical. The two geometrical constraints are 1) Q must be even to maintain symmetry between the phases and 2) the coil throw must be odd so that each slot contains only one coil side. The electrical constraints can be divided into two categories: even and odd periodicity. If the periodicity is even, the transformation is always possible; however, the harmonic content and winding factor are determined by $\frac{Q}{t}$. The evaluation of the harmonic content and winding factor for the transformation to a single-layer can be described by several cases, as shown in Table 4.1.

The star of slots theory provides a method for designing a machine with null mutual inductance. In double-layer windings, the ratio of stator slots to periodicity must be an even number. Single-layer windings will have null mutual inductance when the ratio of the slots to twice the periodicity is even.

Case #	Periodicity	$\frac{Q}{t}$	$\frac{Q}{2t}$	Distribution Harmonic Order	Distribution Factor
1	even	odd		even & odd	same
2	even	even	even	odd	increase
3	even	even	odd	even & odd	same
4	odd	even	odd	odd	same
5	odd	even	even	even & odd	increase

Table 4.1: MMF harmonic order and distribution factor for transformation of double-layer winding to single-layer winding for various cases based on machine periodicity and number of stator slots.

4.1.2 Software

Two software packages were used to design and analysis the permanent magnet synchronous machines with fractional slot concentrated windings: SPEED and Flux2D. SPEED, a lumped-parameter model, has a graphical interface that was used to design the stator laminations, define the stator windings and analyze the resulting MMF harmonic content and winding factors. Flux2D, time-dependent nonlinear finite element method with circuit coupling, was used to analyze torque, voltage, current for each machine design. This finite element software was also used to analyze iron loss, eddy current loss in the magnets and copper loss. The iron loss calculations, both eddy current and hysteresis, were computed from Bertotti coefficients. Flux2D magneto-static simulations were used to calculate inductances.

4.2 Double-layer PM Machine Design

An available 4-pole neodymium iron boron permanent magnet rotor was used to design a double-layer $\frac{1}{2}$ slot per pole per phase machine. Star of slots theory was applied to select the number of stator slots and examine the MMF harmonic content and the winding factor.

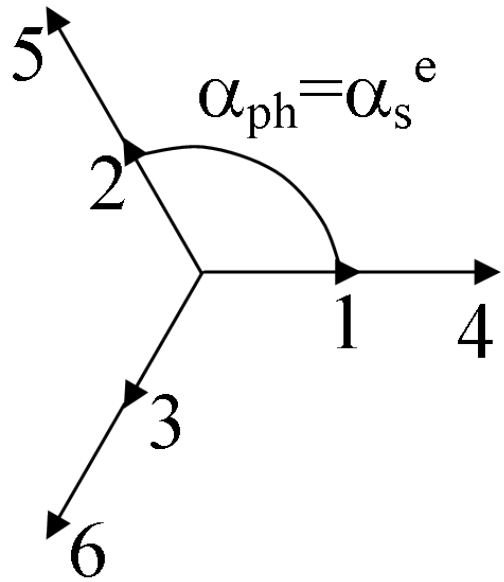

Figure 4.1: Star of slots for double-layer $\frac{1}{2}SPP$ PM machine

The star of slots evaluation is shown in Equations (4.10) to (4.16) and Figure 4.1.

$$Q = 6 \tag{4.10}$$

$$p = 2 \tag{4.11}$$

$$m = 3 \tag{4.12}$$

$$t = GCD(Q, p) = 2 \tag{4.13}$$

$$q_{ph} = \frac{Q}{mt} = 1, feasible \tag{4.14}$$

$$\alpha_s^e = \frac{2\pi p}{Q} = \frac{2\pi}{3} \tag{4.15}$$

$$\alpha_{ph} = \frac{2\pi t}{Q} = \frac{2\pi}{3} \tag{4.16}$$

Since $\frac{Q}{t}$ is odd, the main winding distribution will contain both even and odd harmonic orders. This also indicates that mutual inductance is a factor. It is observed that there are no sub-harmonics present, since $t = p$. The winding factor calculations are shown

Design Parameter	Value	Design Parameter	Value
Stator Diameter	$182.03mm$	Magnet Type	NdFeB N38EH
Rotor Diameter	$98.34mm$	Winding Type	Double-layer Concentrated
Stack Length	$72mm$	Number of Turns	152 turns per coil
Number of Stator Slots	6	Stator Line Voltage	$480V$
Number of poles	4	Maximum Current	$18A_{rms}$
Air gap length	$1mm$	Maximum Power	$8kW$

Table 4.2: Double-layer $\frac{1}{2}$ SPP machine design parameters.

in Equations (4.17) to (4.20).

$$k_d = \frac{\sin(\frac{\pi}{2m})}{q_{ph}\sin(\frac{\alpha_{ph}}{4})} = 1 \tag{4.17}$$

$$\sigma_w = \frac{2\pi p y_q}{Q} = \frac{2\pi}{3} \tag{4.18}$$

$$k_p = \sin(\frac{\sigma_w}{2}) = \frac{\sqrt{3}}{2} \tag{4.19}$$

$$k_w = k_p k_d = \frac{\sqrt{3}}{2} \tag{4.20}$$

An outline of the machine is shown in Figure 4.2 and machine design parameters are given in Table 4.2. The stator and rotor of the manufactured prototype are pictured in Figures 4.3a and 4.3b, respectively.

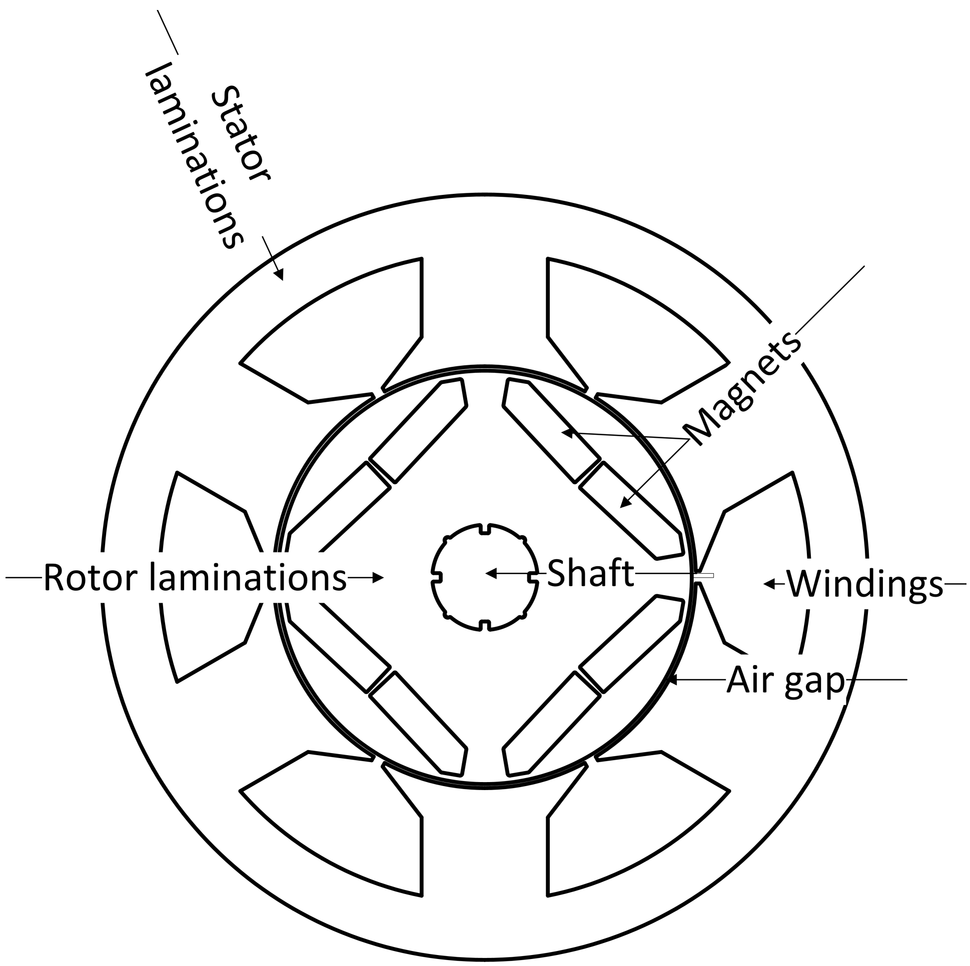

Figure 4.2: Double-layer $\frac{1}{2}SPP$ PM machine laminations

(a) Stator

(b) Rotor

Figure 4.3: Manufactured parts of $\frac{1}{2}$ SPP PM machine - (a)Stator and (b)Rotor with NdFeB magnets-N38EH nickel coated

4.3 Single-layer PM Machine Design

A prototype single-layer $\frac{2}{5}$ slot per pole per phase machine was designed. Star of slots theory was applied to examine the MMF harmonic content and the winding factor. The star of slots evaluation begins with the double-layer design as shown in Equations (4.21) to (4.26)

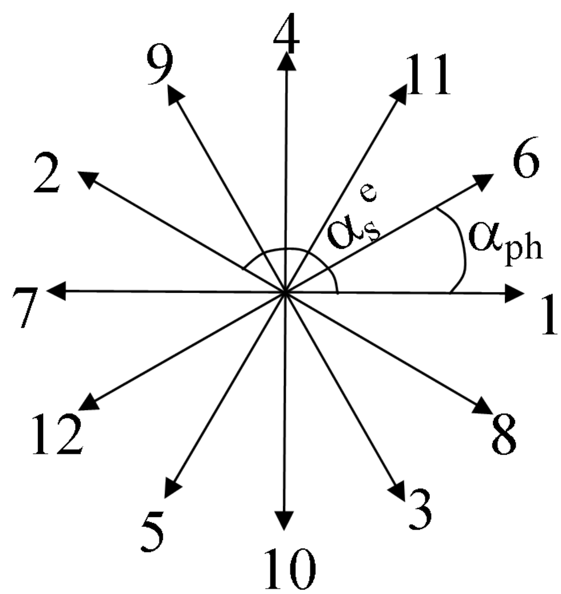

Figure 4.4: Star of slots for double-layer $\frac{2}{5}SPP$ PM machine

and Figure 4.4.

$$Q = 12 \tag{4.21}$$

$$p = 5 \tag{4.22}$$

$$t = GCD(Q, p) = 1 \tag{4.23}$$

$$q_{ph} = \frac{Q}{mt} = 4, feasible \tag{4.24}$$

$$\alpha_s^e = \frac{2\pi p}{Q} = \frac{5\pi}{6} \tag{4.25}$$

$$\alpha_{ph} = \frac{2\pi t}{Q} = \frac{\pi}{6} \tag{4.26}$$

Since $\frac{Q}{t}$ is even, the main winding distribution will contain only odd harmonic orders and the design yields null mutual inductance. The winding factor calculations are shown in Equations (4.27) to (4.30).

$$k_d = \frac{\sin(\frac{\pi}{2m})}{\frac{q_{ph}}{2} sin(\frac{\alpha_{ph}}{2})} = \frac{\sin(\frac{\pi}{6})}{2\sin(\frac{\pi}{12})} = 0.966 \tag{4.27}$$

$$\sigma_w = \frac{2\pi p y_q}{Q} = \frac{5\pi}{6} \tag{4.28}$$

$$k_p = \sin(\frac{\sigma_w}{2}) = 0.966 \tag{4.29}$$

$$k_w = k_p k_d = 0.933 \tag{4.30}$$

t, $\frac{Q}{t}$, $\frac{Q}{2t}$ are all even, according to Table 4.1 the harmonic orders remain unchanged however, the distribution factor increases which yields a higher winding factor, shown in Equations (4.31) and (4.32). The change in the distribution factor is a result of removing half of the phasors, as shown in Figure 4.5. The winding harmonics include sub-harmonics, since $t \neq p$, with magnitudes higher than the main harmonic.

$$k_d = \frac{\sin(\frac{\pi}{2m})}{\frac{q_{ph}}{2} sin(\frac{\alpha_{ph}}{2})} = \frac{\sin(\frac{\pi}{6})}{\sin(\frac{\pi}{6})} = 1 \tag{4.31}$$

$$k_w = k_p k_d = 0.966 \tag{4.32}$$

An outline of the machine is shown in Figure 4.6 and machine design parameters are given in Table 4.3. The stator and rotor laminations of the resulting prototype are pictured in Figures 4.7a and 4.7b, respectively.

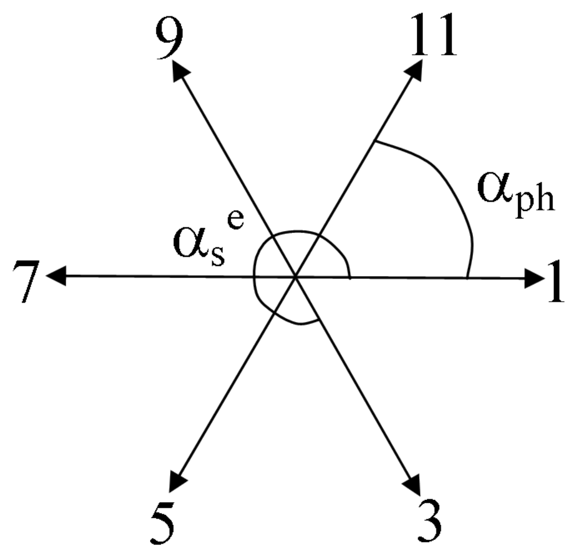

Figure 4.5: Star of slots for single-layer $\frac{2}{5}SPP$ PM machine

Design Parameter	Value	Design Parameter	Value
Stator Diameter	$220mm$	Magnet Type	NdFeB N38EH
Rotor Diameter	$138mm$	Winding Type	Single-layer Concentrated
Stack Length	$72mm$	Number of Turns	150 turns per coil
Number of Stator Slots	12	Stator Line Voltage	$480V$
Number of poles	10	Maximum Current	$18A_{rms}$
Air gap length	$1mm$	Maximum Power	$3.8kW$

Table 4.3: Single-layer $\frac{2}{5}$ SPP machine design parameters.

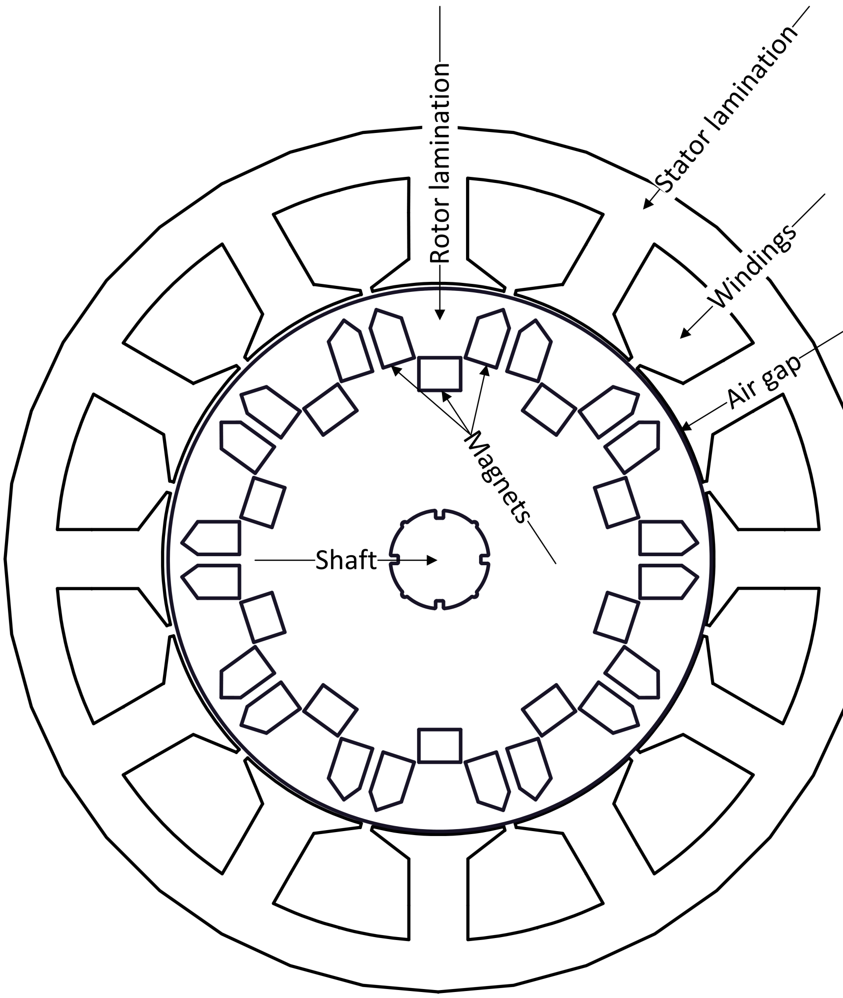

Figure 4.6: Single-layer $\frac{2}{5}SPP$ PM machine laminations

(a) Stator

(b) Rotor

Figure 4.7: Laminations for $\frac{2}{5}$ SPP PM machine - (a)Stator and (b)Rotor

4.4 Experimental Characterization

Permanent magnet synchronous machines are typically modeled in the two axes synchronous frame of reference. DQ theory assumes sinusoidal MMF; however, the arrangement of fractional slot concentrated windings produces a non-sinusoidal MMF. According to [4], the DQ model remains reliable. Self- and cross-saturation are non-linear effects that have been proven important for development of high performance permanent magnet synchronous machine controllers. The d- and q-axis model, including self- and cross-saturation, is given in by Equations (4.35) to (4.37).

$$\lambda_d(i_d, i_q) = L_d(i_d)i_d + L_{dq}(i_d, i_q)i_q + \lambda_{pm} \tag{4.33}$$

$$\lambda_q(i_d, i_q) = L_q(i_q)i_q + L_{qd}(i_d, i_q)i_d \tag{4.34}$$

$$\begin{aligned} v_d &= R_s i_d + [L_d(i_d)\frac{di_d}{dt} + L_{dq}(i_d, i_q)\frac{di_q}{dt}] - \omega_e[L_q(i_q)i_q + L_{qd}(i_d, i_q)i_d] \\ &= R_s i_d + \frac{d\lambda_d(i_d, i_q)}{dt} - \omega_e \lambda_q(i_d, i_q) \end{aligned} \tag{4.35}$$

$$\begin{aligned} v_q &= R_s i_q + [L_q(i_q)\frac{di_q}{dt} + L_{qd}(i_d, i_q)\frac{di_d}{dt} + \omega_e[L_d(i_d)i_d + L_{dq}(i_d, i_q)i_q + \lambda_{pm}] \\ &= R_s i_q + \frac{d\lambda_q(i_d, i_q)}{dt} + \omega_e \lambda_d(i_d, i_q) \end{aligned} \tag{4.36}$$

$$T = \frac{3p}{2}[\lambda_d(i_d, i_q)i_q - \lambda_q(i_d, i_q)i_d] \tag{4.37}$$

In [5], it was determined that cross-coupling is not significant in permanent magnet machines with fractional slot concentrated windings. The frozen permeability method was utilized to prove that the classical d-q model of permanent magnet synchronous machines is accurate when fractional slot concentrated windings are used. It was concluded that cross-coupling in fractional slot concentrated winding permanent magnet machines is negligible, implying that the simplified model in Equations (4.40) to (4.42) provides sufficient accuracy.

$$\lambda_d(i_d) = L_d(i_d)i_d + \lambda_{pm} \tag{4.38}$$

$$\lambda_q(i_q) = L_q(i_q)i_q \tag{4.39}$$

$$\begin{aligned} v_d &= R_s i_d - \omega_e L_q(i_q)i_q \\ &= R_s i_d - \omega_e \lambda_q(i_q) \end{aligned} \tag{4.40}$$

$$\begin{aligned} v_q &= R_s i_q + \omega_e[L_d(i_d)i_d + \lambda_{pm}] \\ &= R_s i_q + \omega_e \lambda_d \end{aligned} \tag{4.41}$$

$$T = \frac{3p}{2}[\lambda_d(i_d)i_q - \lambda_q(i_q)i_d] \tag{4.42}$$

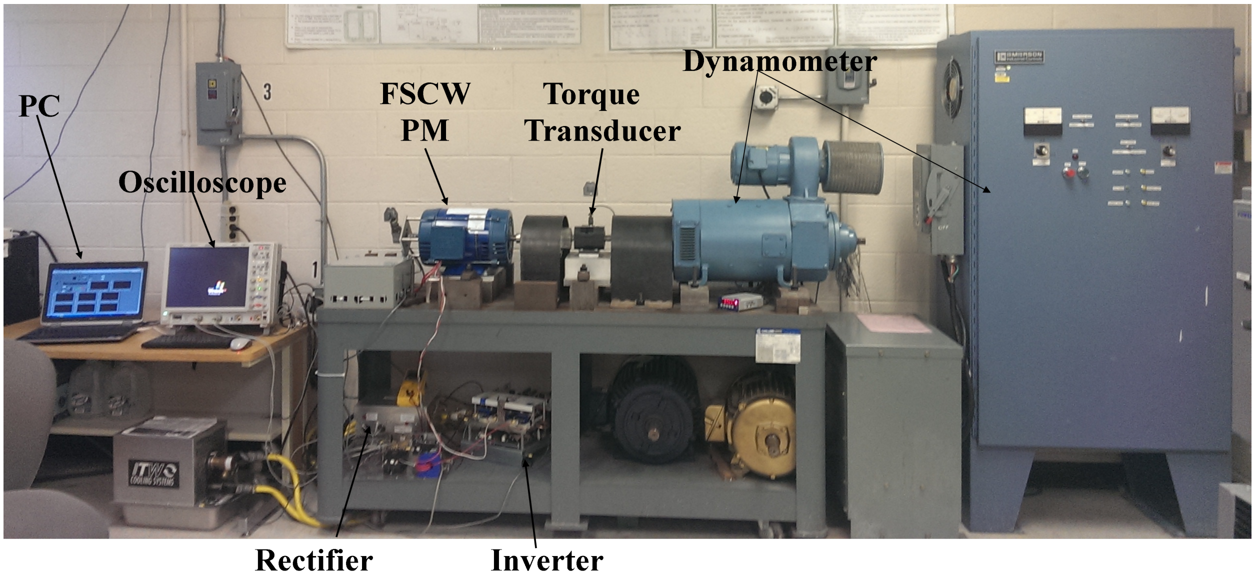

Figure 4.8: Experimental setup

4.4.1 Experimental Setup

The permanent magnet synchronous machines with fractional slot concentrated windings were individually mounted on an Emerson 20hp DC dynamometer to extract characteristic parameters, as shown in Figure 4.8. A PCB torque transducer is connected between the dynamometer and the machine under test. The machine under test is connected to an APS inverter, equipped with current sensors for each phase and a voltage transducer for the DC link. The inverter DC link is connected to an uncontrolled rectifier. The inverter gate driver is connected to an ESI controller board equipped with a Texas Instrument DSP. The DSP's controller area network is used to transmit and receive data from a PC running LabVIEW. An Agilent oscilloscope is used to monitor the phase current measured with an LEM current transducer.

The machine characteristic inductances for both the double-layer $\frac{1}{2}$ slot per pole per phase and single-layer $\frac{2}{5}$ slot per pole per phase designs are experimentally extracted to evaluate the significance of the cross-coupling terms [43]. A two step process is used to acquire the machine characteristic parameters.

1. Experimental Data Acquisition
2. Experimental Data Processing

4.4.2 Experimental Data Acquisition

The experimental setup is shown in Figure 4.9 is used to acquire the data required for extracting the machine's characteristic inductances. The dynamometer controls the speed of the motor under test. The AC currents and DC voltage are fed back for control. The Texas Instrument floating point DSP is flash programmed to control the machine current. Controller area network (CAN) is used to transfer the machine variables required for characterization from a DSP to a computer running a LabVIEW virtual instrument. The LabVIEW virtual instrument is used to transmit the desired current magnitude and angle, as well as save data to the computer hard disk. As shown in the permanent magnet synchronous machine model including cross-coupling terms, shown in Equations (4.35) and (4.36), the variables required to extract the machine characteristic inductances are:

- Phase Voltage
- Phase Current
- Rotor Position
- Machine Speed

The phase voltage is estimated instead of using voltage transducers. This is as accurate as measuring, since DSP internal variables are used to perform the estimation [43]. Current

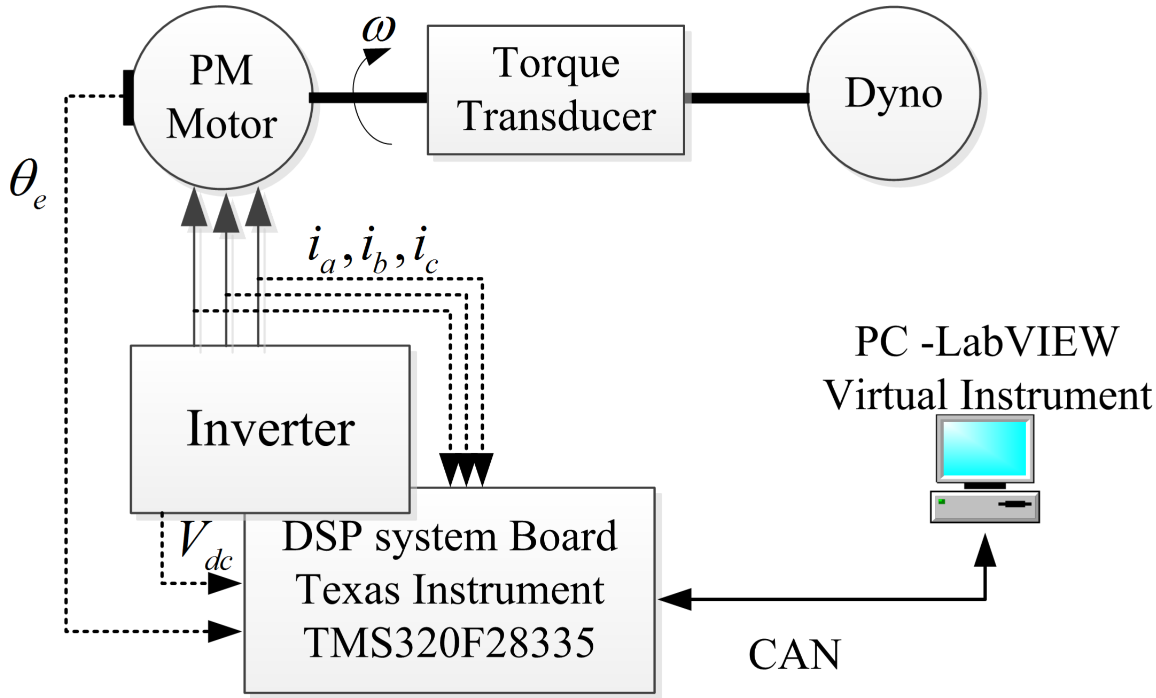

Figure 4.9: Experimental setup for collecting data to extract the machine characteristic inductances.

transducers provide phase current measurement. An optical rotary position encoder is used for position feedback and speed calculation. The encoder must be aligned to the rotor magnet axis in software. The motor's open circuit voltage is used for alignment [43, 44]. After verifying proper rotor alignment, the current command is set to $0\angle 90^{\circ}A$ and the variables are recorded. This process is repeated for all of the $I_s\angle\delta^{\circ}A$ combinations shown in Table 4.4.

4.4.3 Experimental Data Processing

The acquired data is processed off-line to extract the flux linkages, which inherently include self- and cross-saturation effects. The acquired data during $0\angle 90^{\circ}A$ command is processed first to extract the permanent magnet flux linkage, λ_{pm}. The fundamental component of the

	δ									
I_s	$90°$	$100°$	$110°$	$120°$	$130°$	$140°$	$150°$	$160°$	$170°$	$180°$
$5A$										
$10A$										
$15A$										
$20A$										
$25A$										

Table 4.4: Table used for data acquisition.

estimated voltage and the position are used to determine the d- and q-axis components, v_d and v_q. Manipulating Equation (4.36) with $i_d = 0$ and $i_q = 0$ results in Equation (4.43).

$$\lambda_{pm} = \frac{v_q}{\omega_e} \tag{4.43}$$

The d- and q-axis flux linkages are determined from the data acquired for each current command. Phase resistance is measured using a multimeter. Solving Equations (4.35) and (4.36) in steady-state for d- and q-axis flux linkages result in Equations (4.44) and (4.45).

$$\lambda_d(i_d, i_q) = \frac{v_q - i_q R_s}{\omega_e} \tag{4.44}$$

$$\lambda_q(i_d, i_q) = \frac{i_d R_s - v_d}{\omega_e} \tag{4.45}$$

The inductances in Equations (4.33) and (4.34) are calculated using Equations (4.46) to (4.49).

$$L_d(i_d) = \frac{\lambda_d(i_d, 0) - \lambda_{pm}}{i_d} \tag{4.46}$$

$$L_q(i_q) = \frac{\lambda_q(0, i_q)}{i_q} \tag{4.47}$$

$$L_{dq}(i_d, i_q) = \frac{\lambda_d(i_d, 0) - \lambda_d(i_d, i_q)}{i_q} \tag{4.48}$$

$$L_{qd}(i_d, i_q) = \frac{\lambda_q(0, i_q) - \lambda_q(i_d, i_q)}{i_d} \tag{4.49}$$

4.4.4 Experimental Results

The dynamometer rotated the double-layer $\frac{1}{2}$ slot per pole per phase machine at 700rpm during the data acquisition process. The extracted flux linkages are shown in Figures 4.10 and 4.11. The single-layer $\frac{2}{5}$ slot per pole per phase machine was rotated by the dynamometer at 300rpm. The resulting flux linkages are shown in Figures 4.13 and 4.14. These experimental flux linkages were used to determine the torque-speed characteristics of each machine at rated current and voltage. The resulting torque-speed envelopes are shown in Figure 4.12 for the double-layer $\frac{1}{2}$ slot per pole per phase machine and Figure 4.15 for the single-layer $\frac{2}{5}$ slot per pole per phase machine.

The extracted inductances of the double-layer $\frac{1}{2}$ slot per pole per phase design are shown in Figures 4.16 and 4.17. The single-layer $\frac{2}{5}$ slot per pole per phase design extracted inductances are shown in Figures 4.18 and 4.19. It is noted that cross-coupling is significant and should not be neglected.

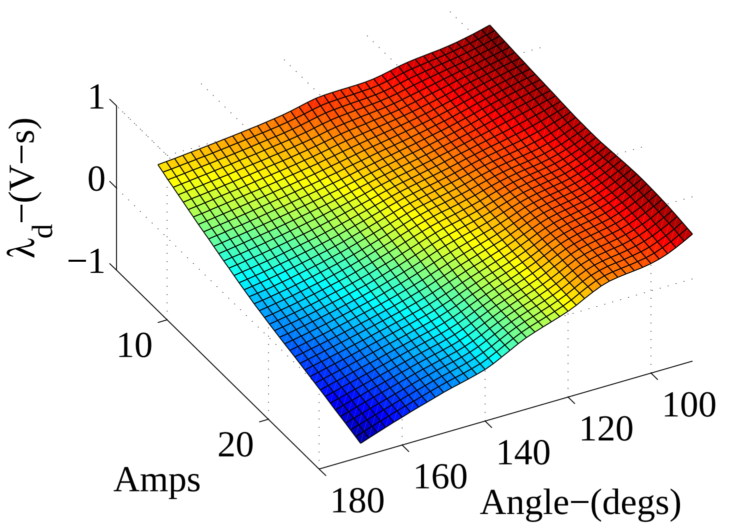

Figure 4.10: Experimental D-axis Flux Linkage of $\frac{1}{2}$ SPP PM Machine

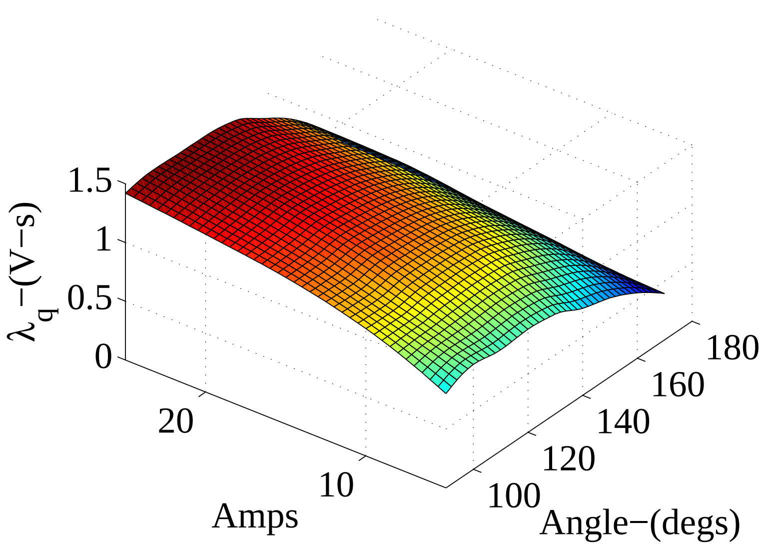

Figure 4.11: Experimental Q-axis Flux Linkage of $\frac{1}{2}$ SPP PM Machine

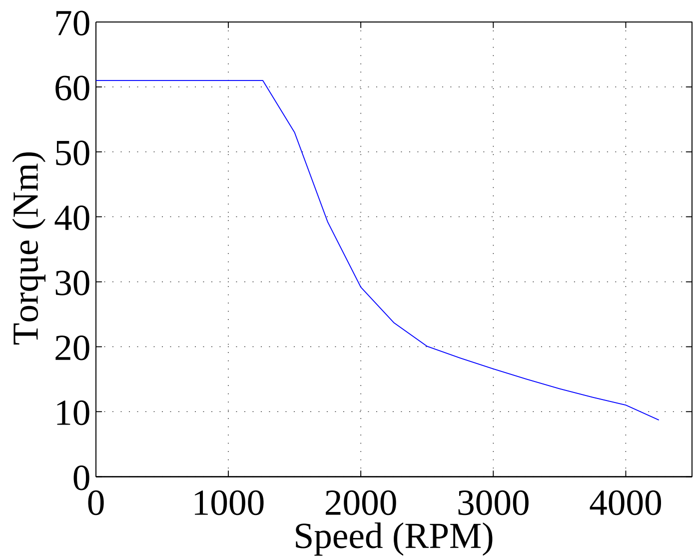

Figure 4.12: Experimental Torque-speed envelope for $\frac{1}{2}$ SPP PM Machine

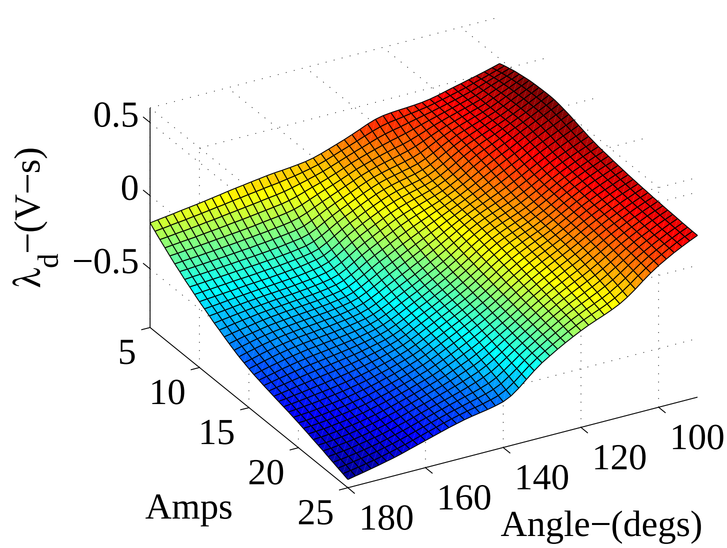

Figure 4.13: Experimental D-axis Flux Linkage of $\frac{2}{5}$ SPP PM Machine

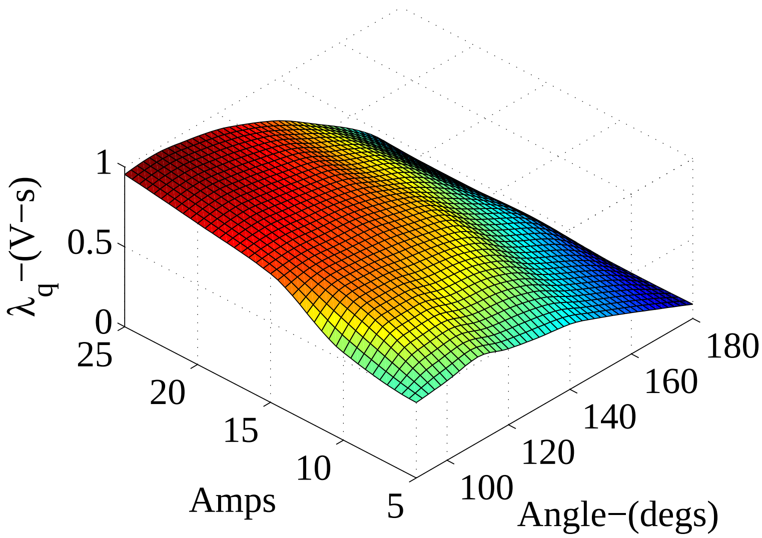

Figure 4.14: Experimental Q-axis Flux Linkage of $\frac{2}{5}$ SPP PM Machine

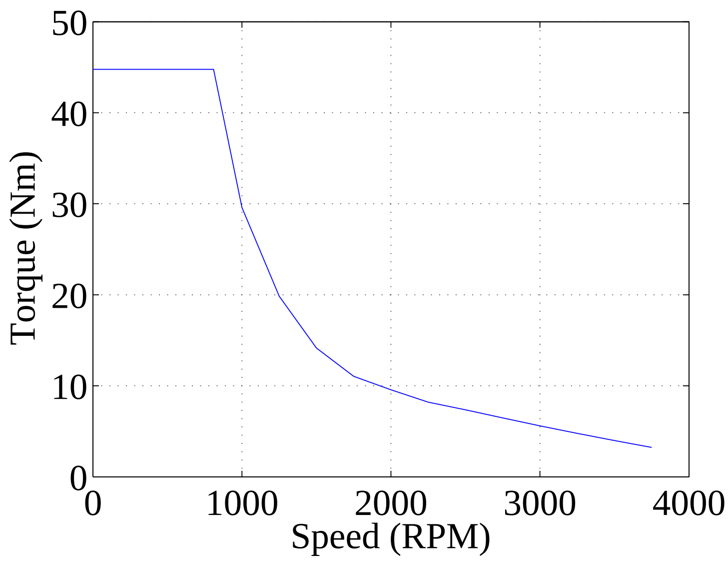

Figure 4.15: Experimental Torque-speed envelope for $\frac{2}{5}$ SPP PM Machine

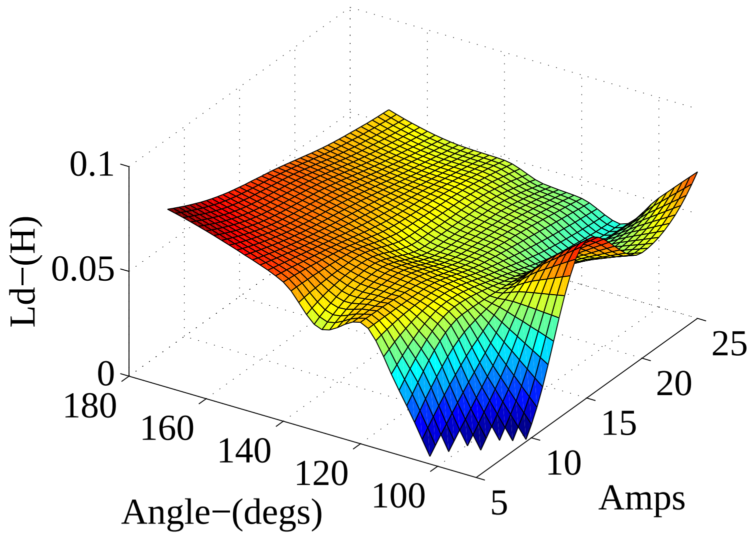

Figure 4.16: Experimental D-axis Inductance of $\frac{1}{2}$ SPP PM Machine

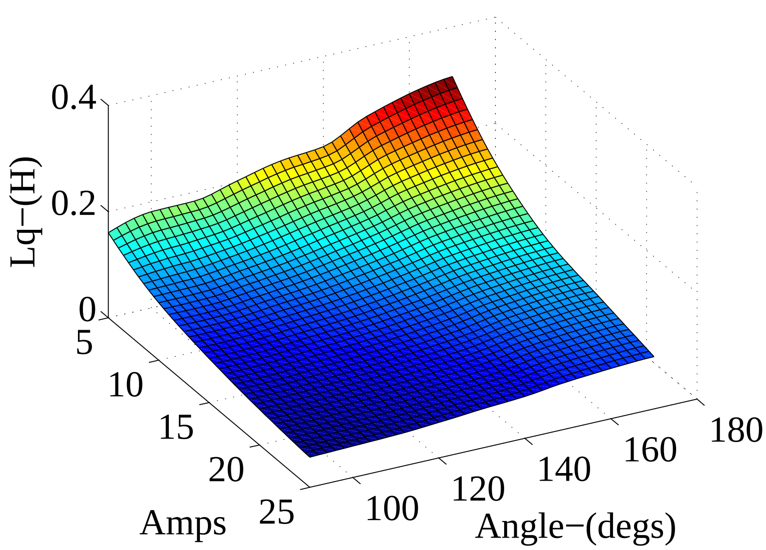

Figure 4.17: Experimental Q-axis Inductance of $\frac{1}{2}$ SPP PM Machine

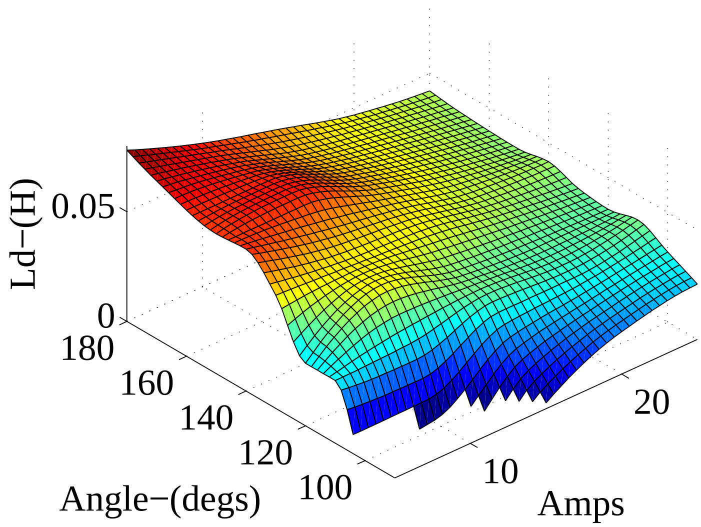

Figure 4.18: Experimental D-axis Inductance of $\frac{2}{5}$ SPP PM Machine

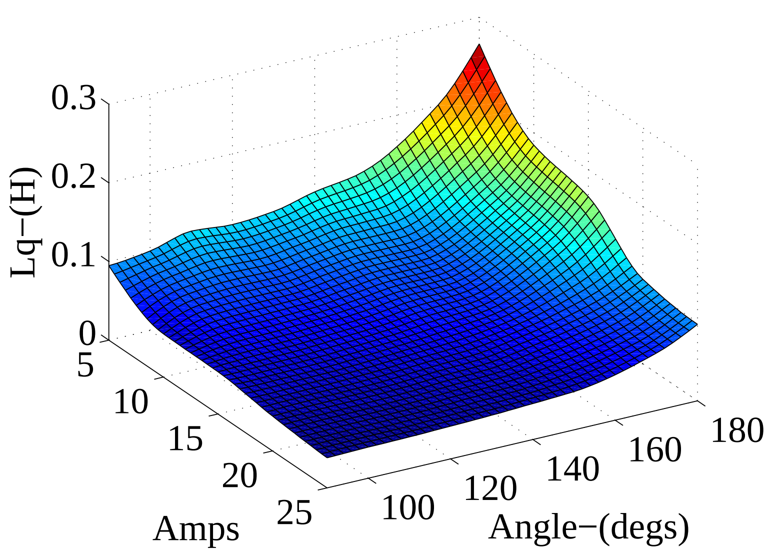

Figure 4.19: Experimental Q-axis Inductance of $\frac{2}{5}$ SPP PM Machine

4.5 Finite Element Analysis

Finite element analysis of both healthy machines was completed to analyze the cogging torque, back-emf, torque ripple and q- and d-axis inductances. As expected, cogging is lower in the $\frac{2}{5}$ slot per pole per phase design, shown in Figure 4.20.

The open-circuit voltage of the double-layer $\frac{1}{2}$ slot per pole per phase design and the single-layer $\frac{2}{5}$ slot per pole per phase design are shown in Figures 4.21 and 4.23, respectively. Higher order harmonics are present in the open-circuit voltages of both designs as shown in Figures 4.22 and 4.24.

The double-layer $\frac{1}{2}$ slot per pole per phase permanent magnet design delivered more torque than the single-layer $\frac{2}{5}$ slot per pole per phase design on average. The $\frac{1}{2}$ slot per pole per phase design delivered an average 55Nm with a 10Nm ripple, shown in Figure 4.25, whereas the $\frac{2}{5}$ slot per pole per phase design delivered an average 34Nm with a 10Nm ripple, shown in Figure 4.26.

The inductance of the double-layer design was also calculated from finite element data, including self-saturation only. The results are shown in Figure 4.27. Inductances of the single-layer $\frac{2}{5}$ slot per pole per phase permanent magnet machine design are shown in Figure 4.28. Iron permeability was confirmed as an inductance factor using the single-layer machine finite element model. A second model of the machine was developed describing a constant permeability for both the stator and rotor iron. The resulting inductances are shown in Figure 4.29.

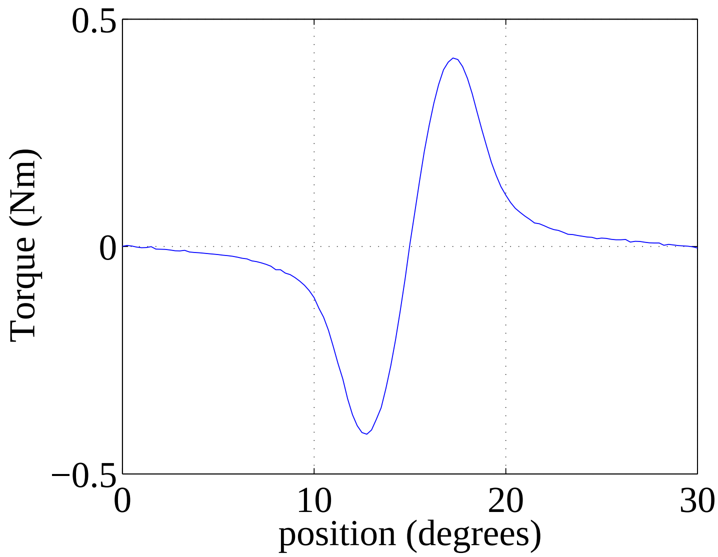

(a) $\frac{1}{2}$ SPP

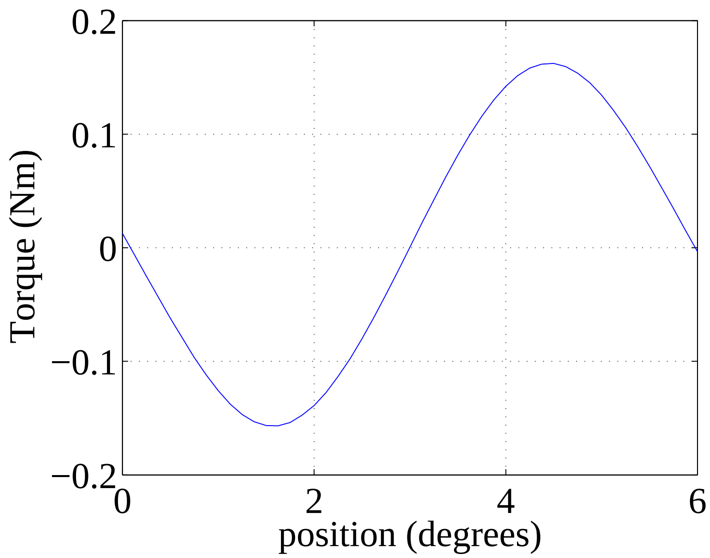

(b) $\frac{2}{5}$ SPP

Figure 4.20: Double-layer $\frac{1}{2}$ SPP and Single-layer $\frac{2}{5}$ SPP PM Machine Cogging Torque (finite element results).

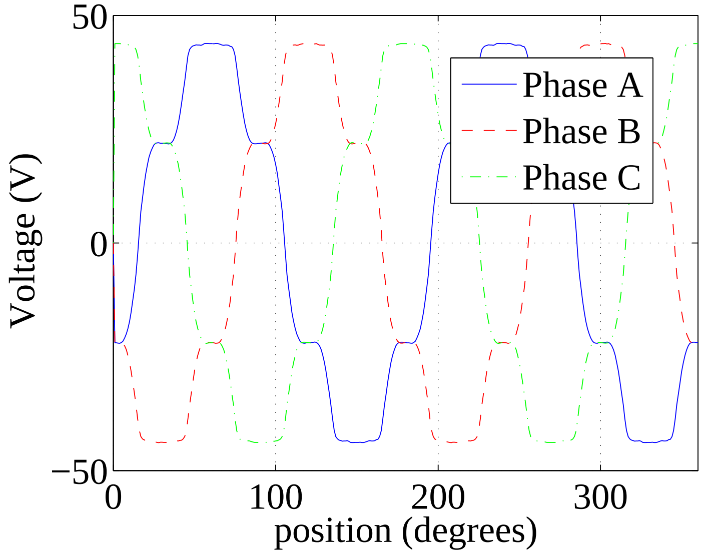

Figure 4.21: Double-layer $\frac{1}{2}$ SPP PM Machine BackEMF (finite element results).

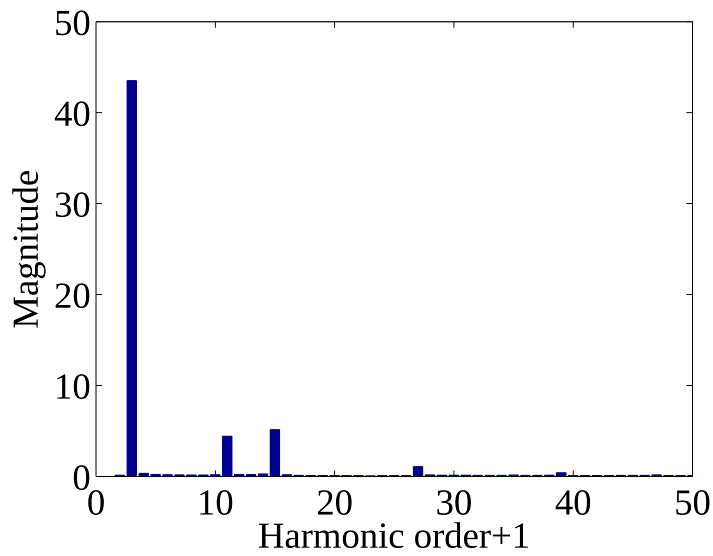

Figure 4.22: Harmonic Content in Double-layer $\frac{1}{2}$ SPP PM Machine.

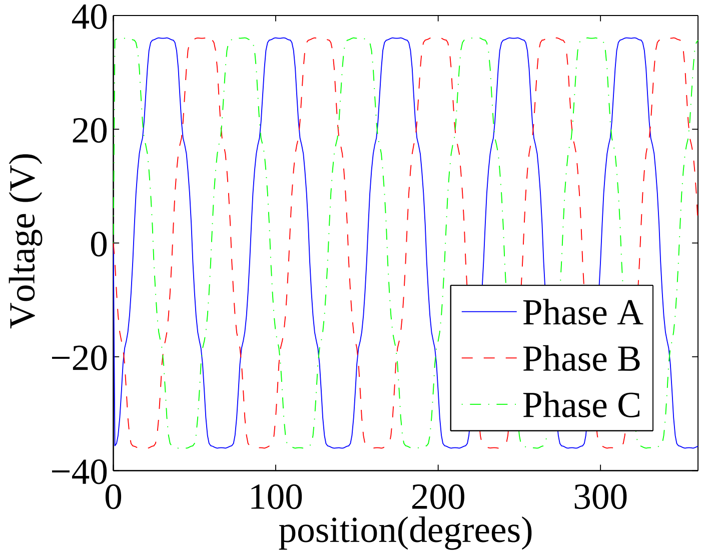

Figure 4.23: Single-layer $\frac{2}{5}$ SPP PM Machine BackEMF (finite element results).

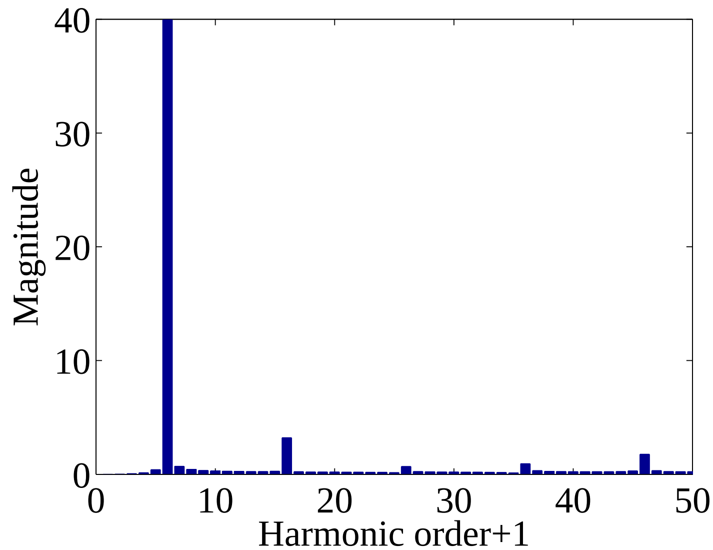

Figure 4.24: Harmonic Content in Single-layer $\frac{2}{5}$ SPP PM Machine.

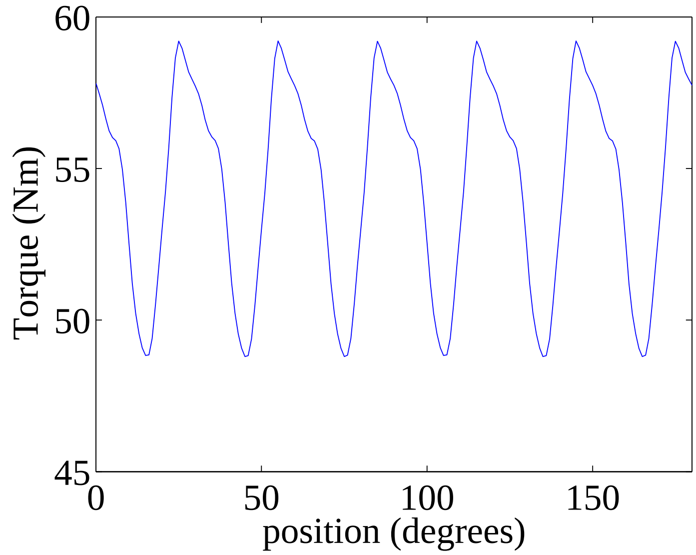

Figure 4.25: Double-layer $\frac{1}{2}$ SPP PM Machine Torque (finite element results).

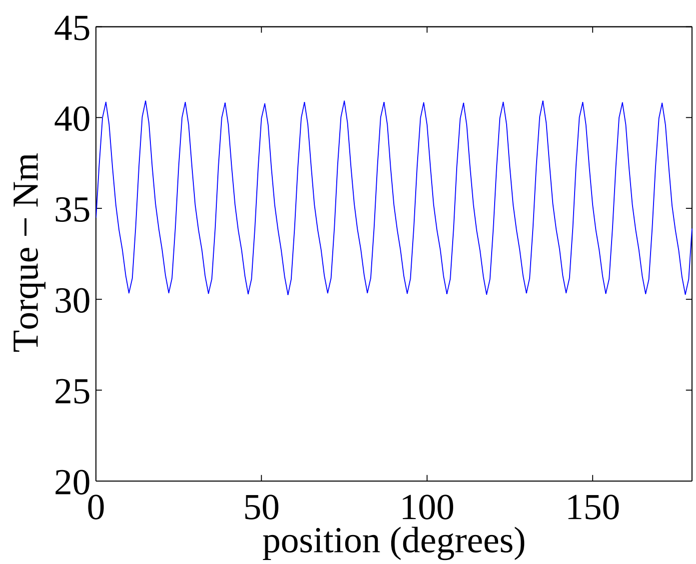

Figure 4.26: Single-layer $\frac{2}{5}$ SPP PM Machine Torque (finite element results).

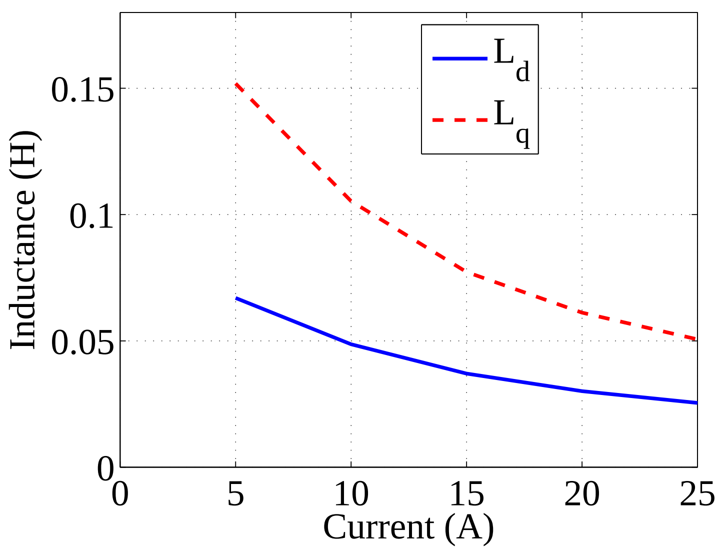

Figure 4.27: Double-layer $\frac{1}{2}$ SPP PM Machine Inductances (finite element results).

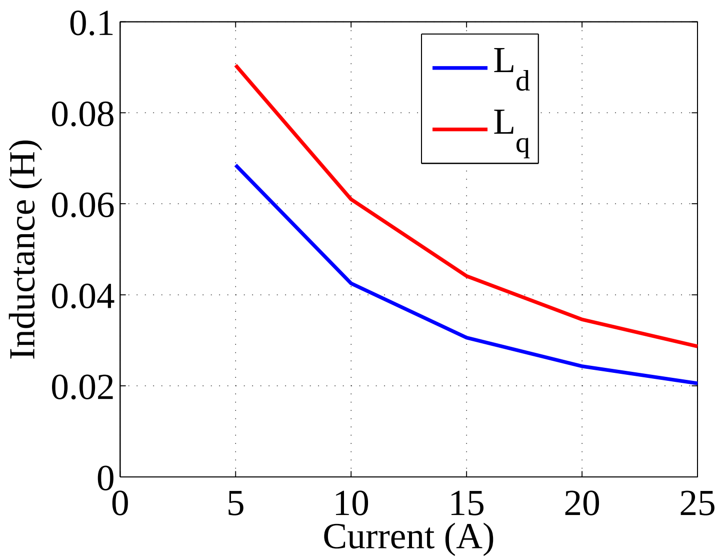

Figure 4.28: Single-layer $\frac{2}{5}$ SPP PM Machine Inductances (finite element results).

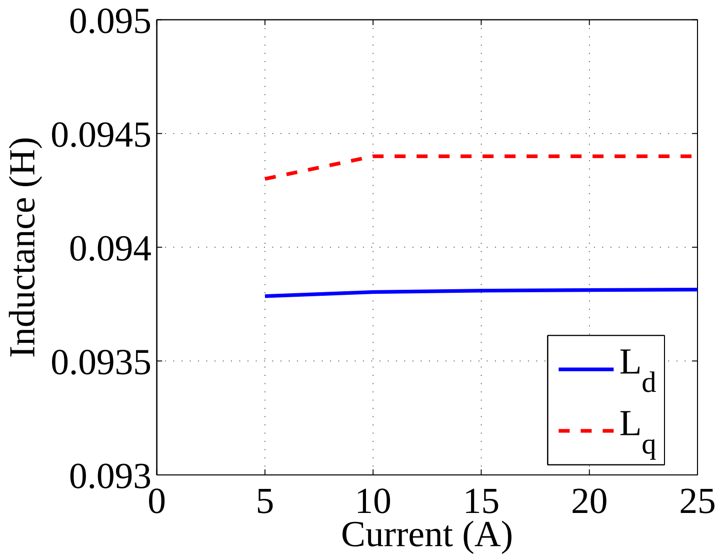

Figure 4.29: Inductance of single-layer FSCW PMSM with iron having constant permeability (finite element results)

4.6 Performance with Stator Inter-turn Failure

The addition of inter-turn short-circuits of varying number of turns to the finite element models revealed that the circulating current due to a short circuit in the single-layer machine design is highest for a single-turn fault, as reported in [45]. However, the circulating current due to a short-circuit across 10% of turns in the double-layer machine design is highest. The back-emf of the machine with inter-turn faults was also analyzed using finite element. The back-emf of the non-faulted phases in double-layer winding machine was affected by the inter-turn faults, however, not in the machine with single-layer windings. The torque ripple was found to increase with number of turns involved for both designs.

4.6.1 Double-layer $\frac{1}{2}$ SPP PM Machine

The open-circuit voltage of each phase is affected by the current circulating in the shorted turns, shown in Figures 4.30 to 4.32. As the number of turns increases, the voltage of the

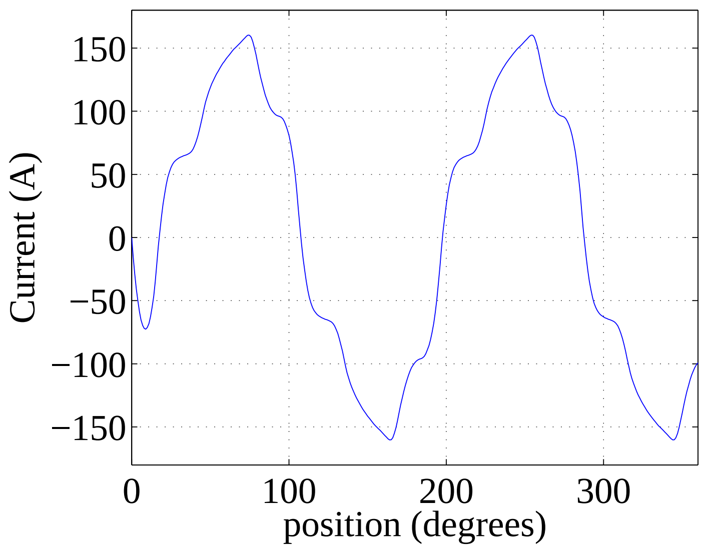

Figure 4.30: Circulating Current in Double-layer $\frac{1}{2}$ SPP PM Machine with Single-Turn Short-Circuited (finite element results).

Machine Condition	Torque Ripple (Nm)	Fault Current (Arms)	Fault Current Average (A)
Healthy	10		
Single-turn Short-Circuited	11.13	106.88	1.26
10% Turns in Slot Short-Circuited	46.11	125.79	72.38
20% Turns in Slot Short-Circuited	50.59	72.42	45.82

Table 4.5: Comparison of Torque Ripple and Current Circulating in Windings of Double-layer $\frac{1}{2}$ SPP PM Machine Due to Short-Circuited Inter-turns.

faulted phase reduces, as shown in Figures 4.33 to 4.35. The torque ripple increased as the number of turns involved in the short increased, as shown in Figures 4.36 to 4.38. The average torque of a healthy machine is 55 Nm and the rated current is 18 Arms. The effects of a shorted turn on the machine torque and the current flowing in the faulted phase is shown in Table 4.5.

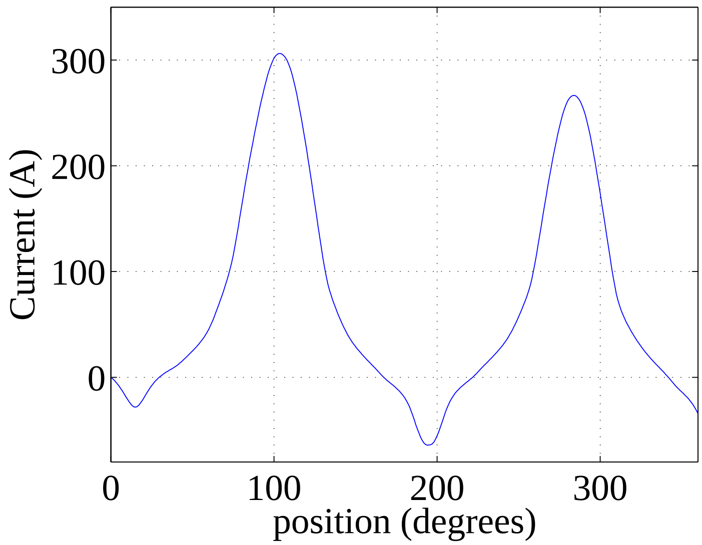

Figure 4.31: Circulating Current in Double-layer $\frac{1}{2}$ SPP PM Machine with 10% of Turns in Slot Short-Circuited (finite element results).

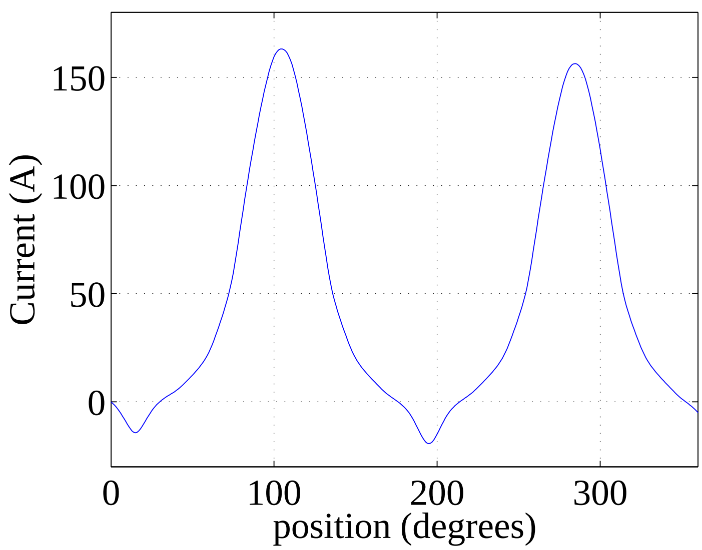

Figure 4.32: Circulating Current in Double-layer $\frac{1}{2}$ SPP PM Machine with 20% of Turns in Slot Short-Circuited (finite element results).

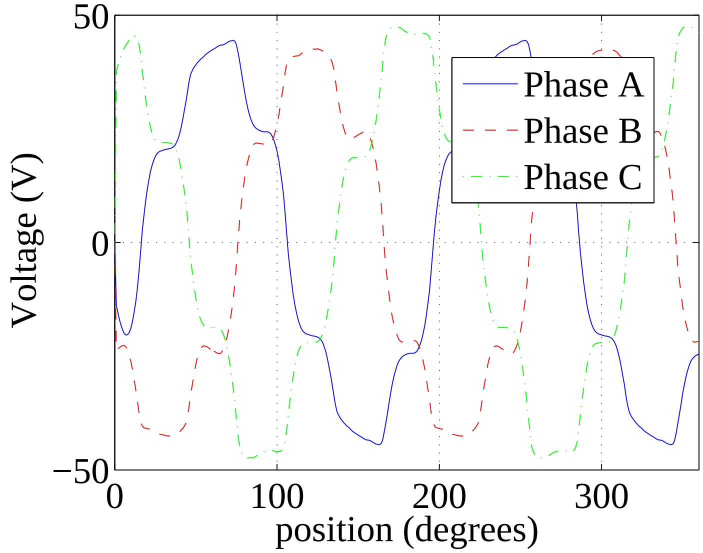

Figure 4.33: Open-Circuit Voltage in Double-layer $\frac{1}{2}$ SPP PM Machine with Single-Turn Short-Circuited (finite element results).

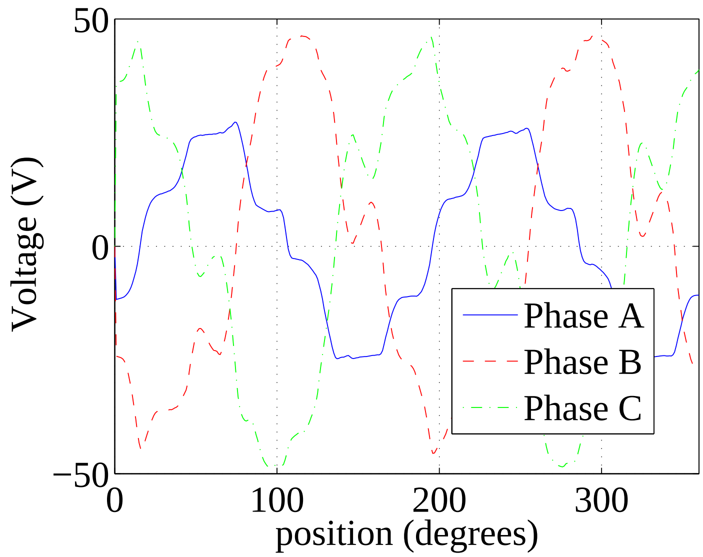

Figure 4.34: Open-Circuit Voltage in Double-layer $\frac{1}{2}$ SPP PM Machine with 10% of Turns in Slot Short-Circuited (finite element results).

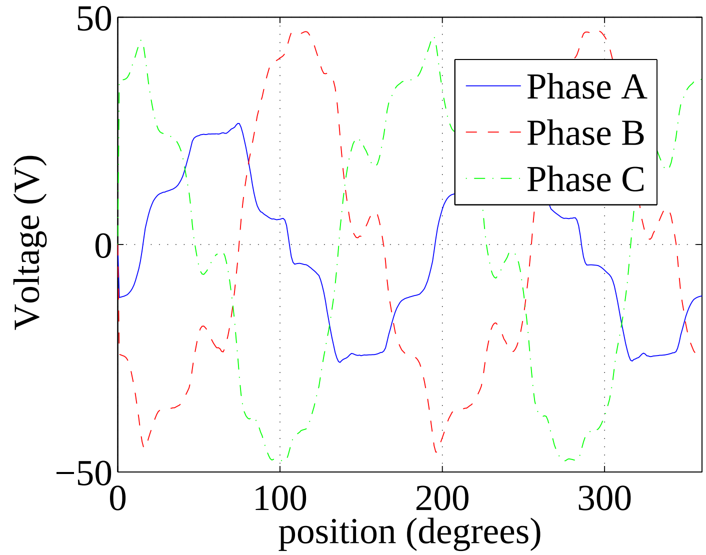

Figure 4.35: Open-Circuit Voltage in Double-layer $\frac{1}{2}$ SPP PM Machine with 20% of Turns in Slot Short-Circuited (finite element results).

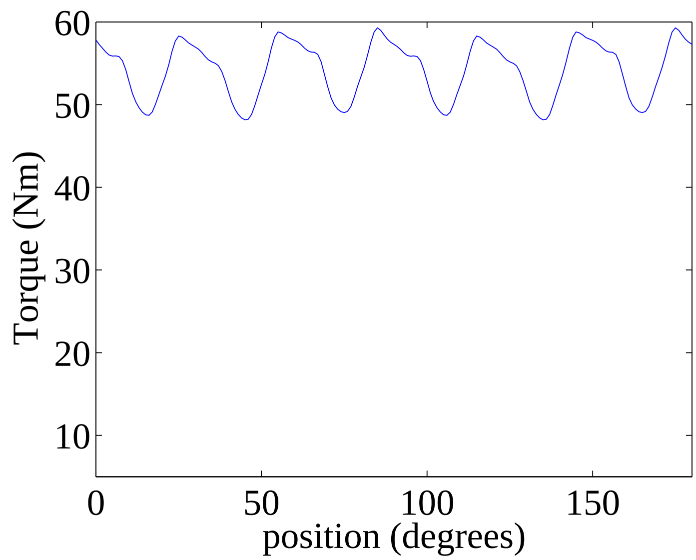

Figure 4.36: Torque of Double-layer $\frac{1}{2}$ SPP PM Machine with Single-Turn Short-Circuited (finite element results).

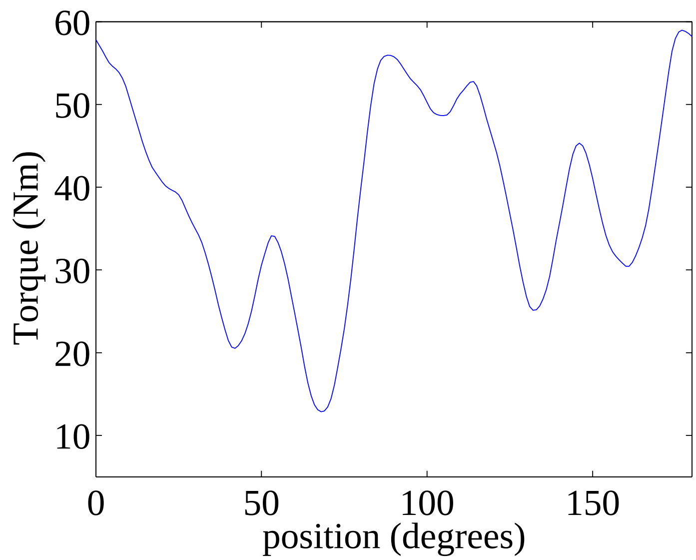

Figure 4.37: Torque of Double-layer $\frac{1}{2}$ SPP PM Machine with 10% of Turns in Slot Short-Circuited (finite element results).

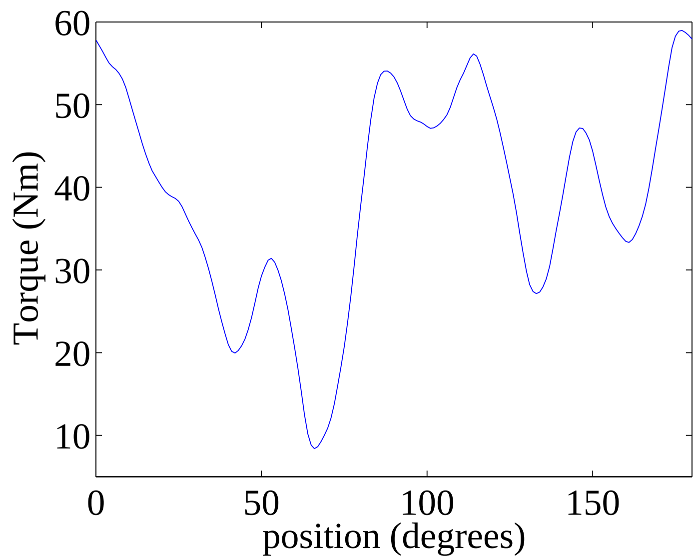

Figure 4.38: Torque of Double-layer $\frac{1}{2}$ SPP PM Machine with 20% of Turns in Slot Short-Circuited (finite element results).

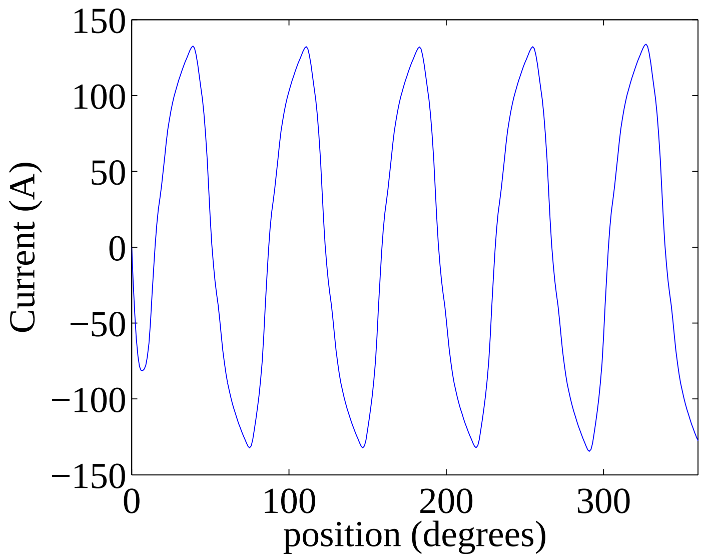

Figure 4.39: Circulating Current in Single-layer $\frac{2}{5}$ SPP PM Machine with Single-Turn Short-Circuited (finite element results).

4.6.2 Single-layer $\frac{2}{5}$ SPP PM Machine

The open-circuit voltage of the faulted phase is affected by the current circulating in the shorted turns, shown in Figures 4.39 to 4.41. The open-circuit voltage of the non-faulted phases is not affected. As the number of turns increases, the voltage of the faulted phase reduces, as shown in Figures 4.42 to 4.44. The torque ripple increased as the number of turns involved in the short increased, as shown in Figures 4.45 to 4.47. The average torque of a healthy machine is 35 Nm and the rated current is 18 Arms. The effects of a shorted turn on the machine torque and the current flowing in the faulted phase is shown in Table 4.6.

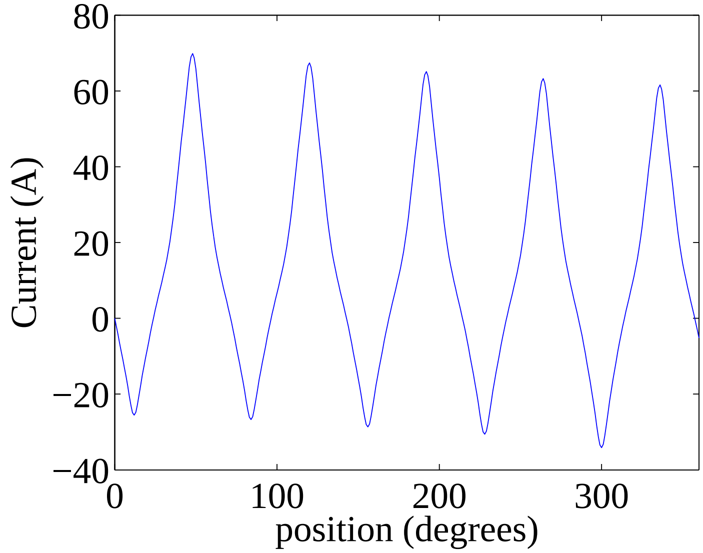

Figure 4.40: Circulating Current in Single-layer $\frac{2}{5}$ SPP PM Machine with 10% of Turns in Slot Short-Circuited (finite element results).

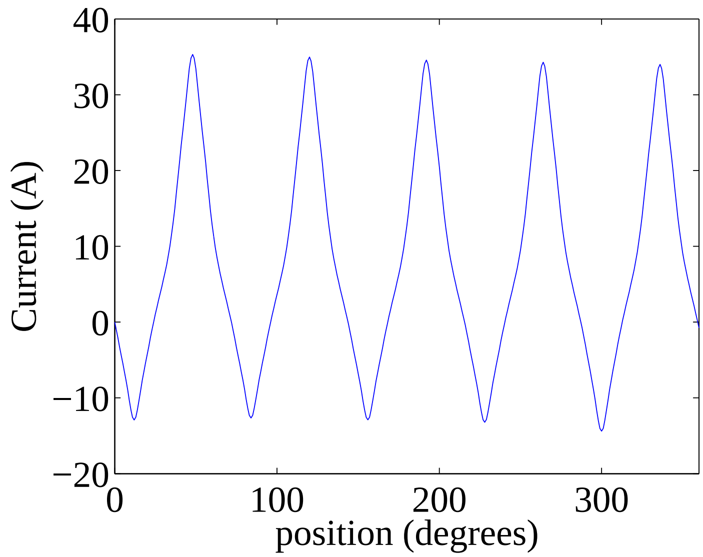

Figure 4.41: Circulating Current in Single-layer $\frac{2}{5}$ SPP PM Machine with 20% of Turns in Slot Short-Circuited (finite element results).

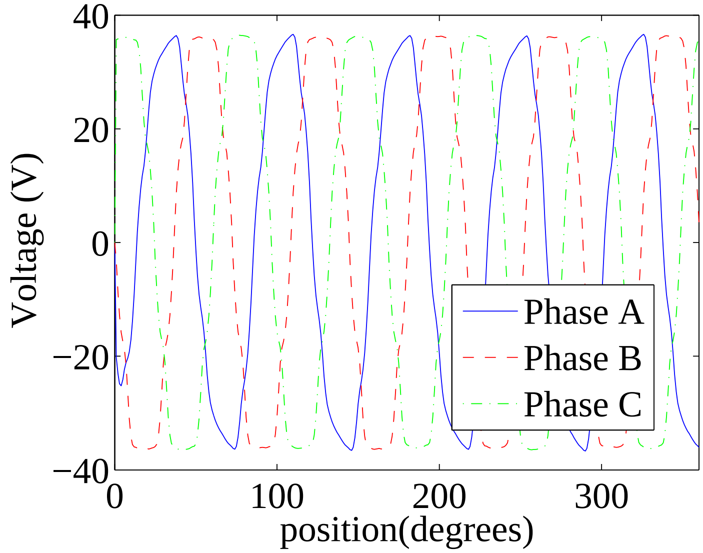

Figure 4.42: Open-Circuit Voltage in Single-layer $\frac{2}{5}$ SPP PM Machine with Single-Turn Short-Circuited (finite element results).

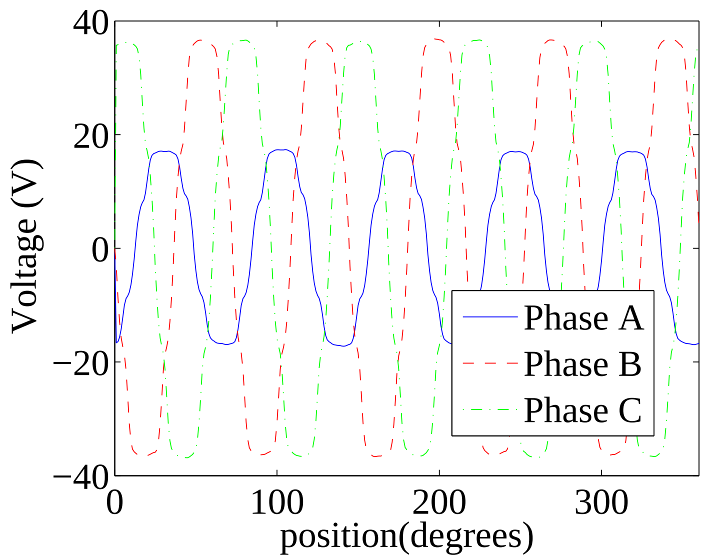

Figure 4.43: Open-Circuit Voltage in Single-layer $\frac{2}{5}$ SPP PM Machine with 10% of Turns in Slot Short-Circuited (finite element results).

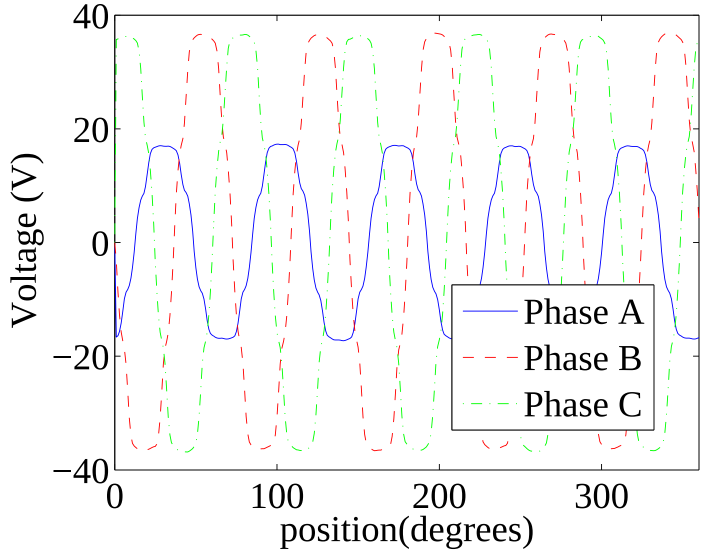

Figure 4.44: Open-Circuit Voltage in Single-layer $\frac{2}{5}$ SPP PM Machine with 20% of Turns in Slot Short-Circuited (finite element results).

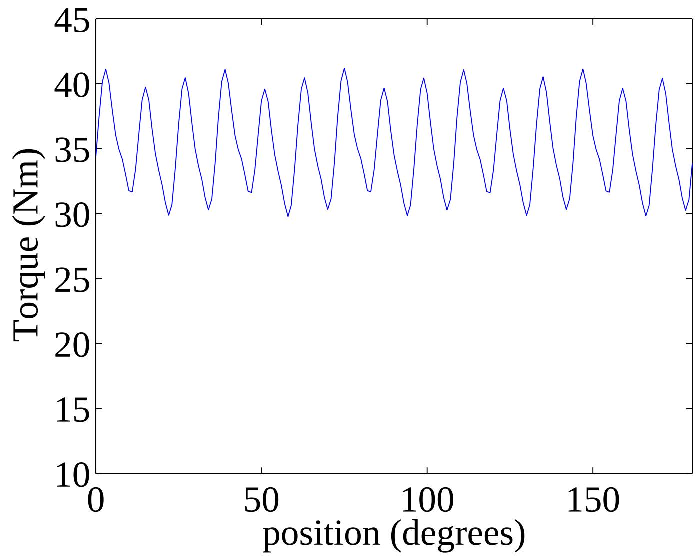

Figure 4.45: Torque of Single-layer $\frac{2}{5}$ SPP PM Machine with Single-Turn Short-Circuited (finite element results).

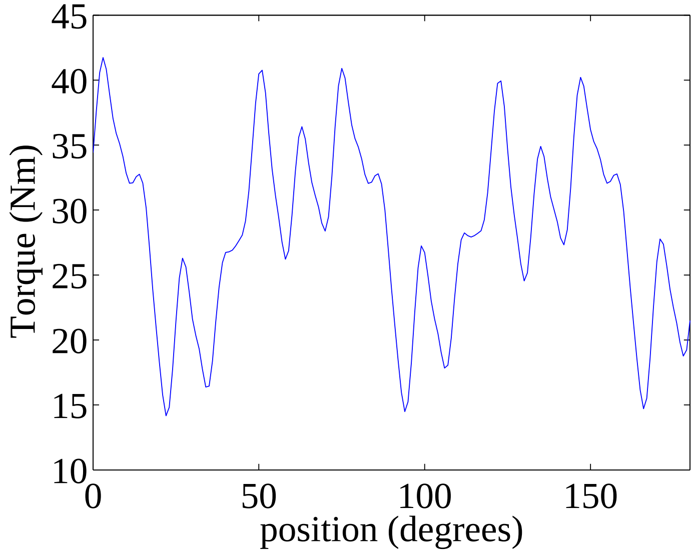

Figure 4.46: Torque of Single-layer $\frac{2}{5}$ SPP PM Machine with 10% of Turns in Slot Short-Circuited (finite element results).

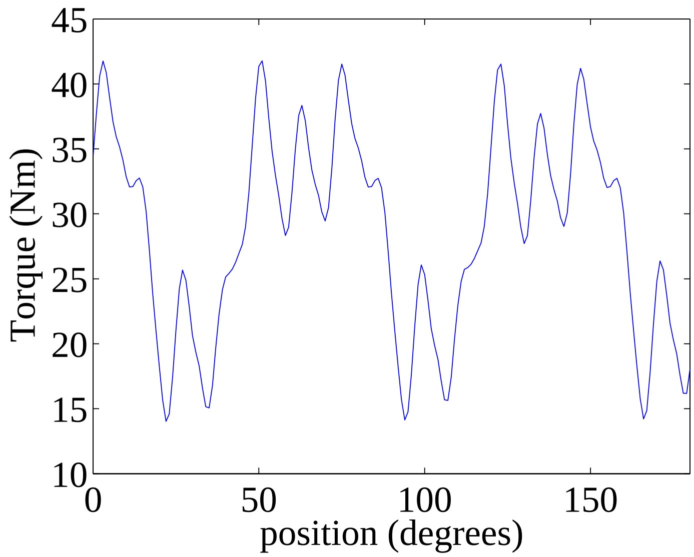

Figure 4.47: Torque of Single-layer $\frac{2}{5}$ SPP PM Machine with 20% of Turns in Slot Short-Circuited (finite element results).

Machine Condition	Torque Ripple (Nm)	Fault Current (Arms)	Fault Current Average (A)
Healthy	10.66		
Single-turn Short-Circuited	11.42	93.75	1.72
10% Turns in Slot Short-Circuited	27.56	30.18	12.88
20% Turns in Slot Short-Circuited	27.75	15.85	7.65

Table 4.6: Comparison of Torque Ripple and Current Circulating in Windings of Single-layer $\frac{2}{5}$ SPP PM Machine Due to Short-Circuited Inter-turns.

4.7 Reliability and Performance of PM Machines Designed with FSCW

A finite element model of a double-layer $\frac{2}{5}$ slot per pole per phase PM machine, using the same rotor and stator laminations as the single-layer described in Section 4.6.2, was analyzed to determine if mutual inductance is the largest contributor to the magnitude of the circulating current and torque ripple. According to the star of slots theory the double-layer $\frac{2}{5}$ slot per pole per phase design has null mutual inductance because $\frac{Q}{2t}$ is even. The circulating currents in the double-layer design are shown in Figure 4.48. The torque ripple associated with insulation failures in this design are shown in Figure 4.49.

Results indicate that mutual inductance affects the magnitude of circulating current produced as a result of short-circuited inter-turns; however, the number of layers used in the fractional slot concentrated winding is also a factor. Double-layer windings, even those designed with zero mutual inductance according to the star of slots, yield higher circulating current except in the case of a single-turn short, as shown in Table 4.7. Single-layer fractional slot concentrated winding designed with null mutual inductance provide increased reliability.

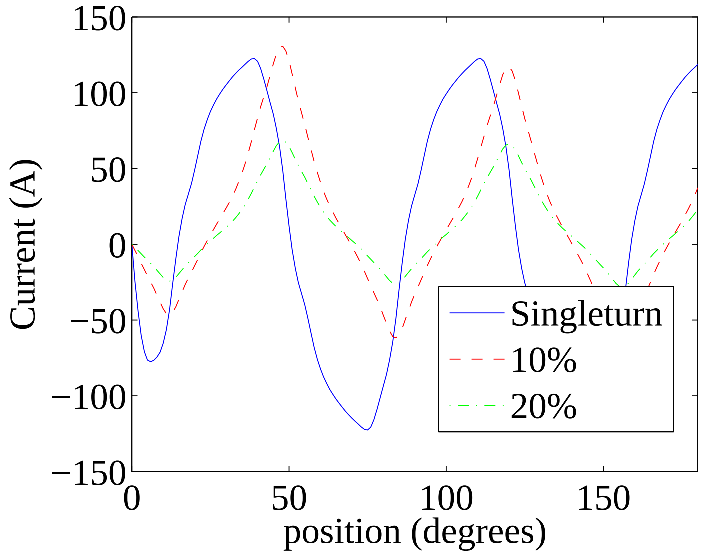

Figure 4.48: Circulating current in short-circuited turns of double-layer $\frac{2}{5}$ SPP PM (finite element results).

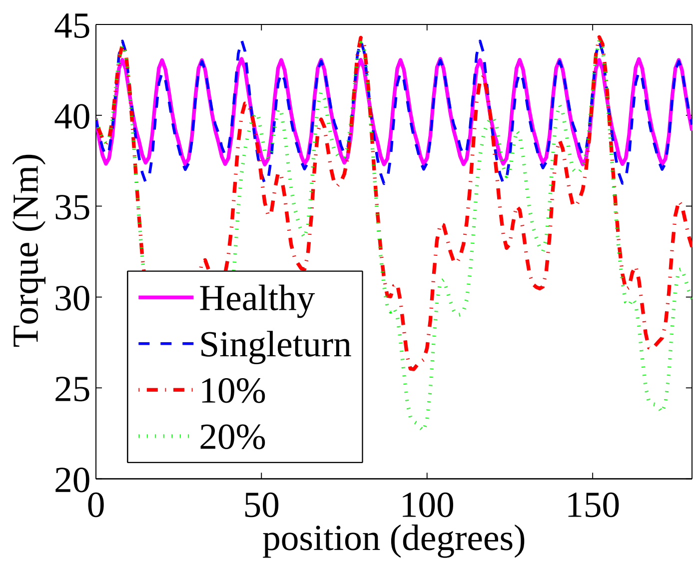

Figure 4.49: Torque for double-layer $\frac{2}{5}$ SPP PM with short-circuited turns (finite element results).

Machine Design	Number in Slot Short-Circuited		
	Single-Turn	10% Turns	20% Turns
Double-layer $\frac{1}{2}$ SPP	5.94	6.99	4.02
Double-layer $\frac{2}{5}$ SPP	4.8	3	1.58
Single-layer $\frac{2}{5}$ SPP	5.21	1.68	.8

Table 4.7: Circulating Current in PM Machines Designed with Fractional Slot Concentrated Windings as a Factor of Rated Current.

Machine Design	Machine Condition			
		Number in Slot Short-Circuited		
	Healthy	Single-Turn	10% Turns	20% Turns
Double-layer $\frac{1}{2}$ SPP	18.18%	20.55%	83.84%	91.98%
Double-layer $\frac{2}{5}$ SPP	14.53%	19.78%	51.48%	56.4%
Single-layer $\frac{2}{5}$ SPP	30.21%	32.36%	78.1%	78.63%

Table 4.8: Torque Ripple in PM Machines Designed with Fractional Slot Concentrated Windings as a Percentage of Average Torque.

This increased reliability is achieved with a compromise in machine performance. The torque ripple of the healthy single-layer machine with zero mutual inductance is 30% of the average torque produced, as shown in Table 4.8. Additionally, higher average torque is achieved with double-layer windings. Higher average torque and lower torque ripple are achieved with double-layer windings. Double-layer windings with null mutual inductance provide higher reliability and less torque ripple when more than one turn is involved in a short.

Chapter 5

PMSM Torque Ripple

The high harmonic content in the stator MMF distribution is attributed to the torque ripple associated with single-layer fractional slot concentrated windings permanent magnet synchronous machines; however, there are four sources of torque ripple in permanent magnet synchronous machines. These sources are the harmonics in the stator MMF distribution, the harmonics in the rotor MMF distribution, the variations in permeance due to stator slotting and the variations in permeance due to rotor slotting.

In this chapter, analytical descriptions of each source are developed for a permanent magnet synchronous machine with a single-layer fractional slot concentrated winding. Finally, an analytical description of the torque is presented for the single-layer design.

5.1 Stator MMF Distribution

The stator magnetomotive force (MMF) distribution is directly related to the stator winding configuration. A simplified description of the single-layer fractional slot concentrated winding is shown in Figure 5.1. In this figure the phase a coil conductors are represented as a single conductor in a slot, neglecting the presence of teeth. The direction of the current flowing in the conductor is denoted by $\odot$, out of the page, and $\otimes$, into the page. The resulting MMF can be approximated as a square-wave, as shown in Figure 5.2 with amplitude equivalent to

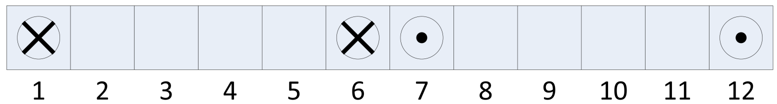

Figure 5.1: Simplified phase A winding distribution of single-layer fractional slot concentrated winding design

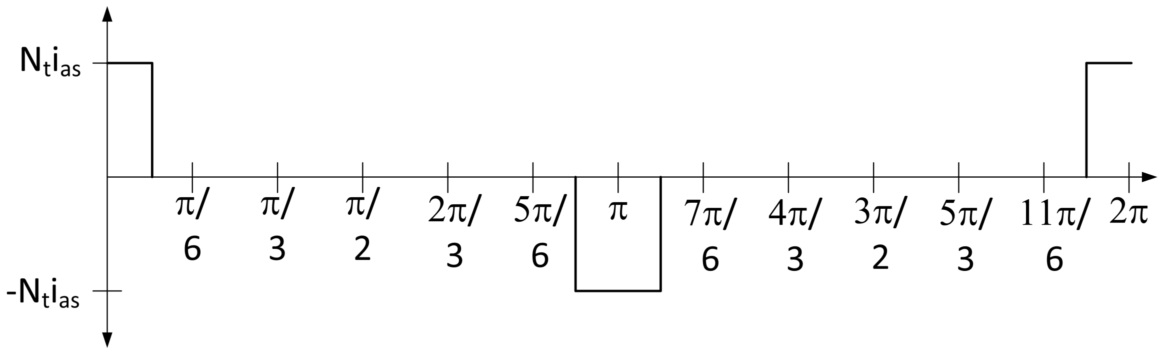

Figure 5.2: Square-wave approximation of the single-layer fractional slot concentrated winding design stator phase A MMF distribution

the product of the number of turns per slot, N_t, and the phase current, i_{as}. The trigonometric Fourier series of the square-wave function is shown in Figure 5.3 and Equation (5.1). The MMF of phases B and C are offset by 120°, as shown in Equations (5.2) and (5.3). Three phase balance currents are described in Equations (5.4) to (5.6). The resulting stator MMF is shown in Equation (5.7).

$$MMF_{as}\left(\phi_s\right) = \sum_{\nu=1}^{\infty} \frac{2N_t i_{as}}{\nu\pi} \sin\left(\nu\frac{\pi}{Q}\right)\left[1-\cos\left(\nu\pi\right)\right]\cos\left(\nu\phi_s\right) \tag{5.1}$$

$$MMF_{bs}\left(\phi_s\right) = \sum_{\nu=1}^{\infty} \frac{2N_t i_{bs}}{\nu\pi} \sin\left(\nu\frac{\pi}{Q}\right)\left[1-\cos\left(\nu\pi\right)\right]\cos\left(\nu\left(\phi_s-\frac{2\pi}{3}\right)\right) \tag{5.2}$$

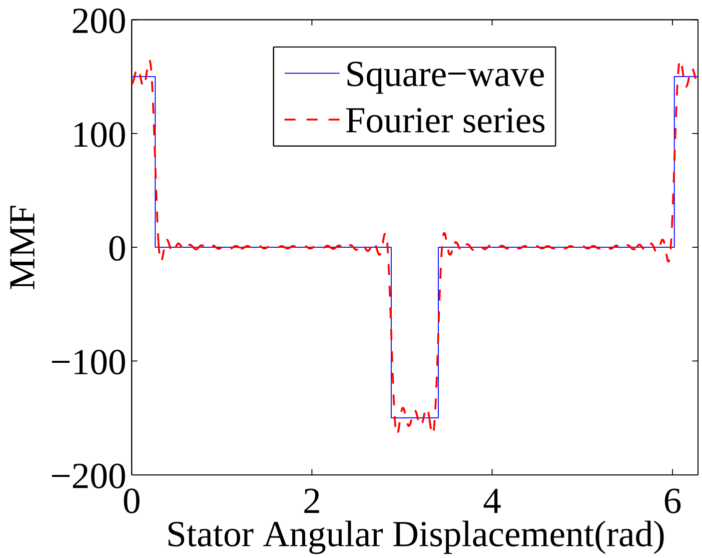

Figure 5.3: Trigonometric Fourier series of the single-layer fractional slot concentrated winding design stator phase A MMF distribution

$$MMF_{cs}\left(\phi_s\right) = \sum_{\nu=1}^{\infty} \frac{2N_t i_{cs}}{\nu\pi} \sin\left(\nu\frac{\pi}{Q}\right)\left[1-\cos\left(\nu\pi\right)\right]\cos\left(\nu\left(\phi_s+\frac{2\pi}{3}\right)\right) \tag{5.3}$$

$$i_{as}(t) = \hat{I}cos(\omega_r t+\delta) = \hat{I}cos(p\theta_r+\delta) \tag{5.4}$$

$$i_{bs}(t) = \hat{I}cos(\omega_r t+\delta-\frac{2\pi}{3}) = \hat{I}cos(p\theta_r+\delta-\frac{2\pi}{3}) \tag{5.5}$$

$$i_{cs}(t) = \hat{I}cos(\omega_r t+\delta+\frac{2\pi}{3}) = \hat{I}cos(p\theta_r+\delta+\frac{2\pi}{3}) \tag{5.6}$$

$$MMF_{s}\left(\phi_s\right) = \sum_{\nu=1}^{\infty} \frac{3N_t \hat{I}}{\nu\pi} \sin\left(\nu\frac{\pi}{Q}\right)\left[1-\cos\left(\nu\pi\right)\right]\cos\left(\nu\phi_s-p\theta_r-\delta\right) \tag{5.7}$$

5.2 Rotor MMF Distribution

The MMF of the rotor is directly related to the rotor configuration. The amplitude of the magnetomotive force of permanent magnets is given by the product of the coercive field intensity of the permanent magnets, H_c, and the magnet thickness, t_m, as shown in Equation (5.8). In surface mounted designs, the flux density on the rotor surface is equivalent to that on the magnet surface; however, this is not true for interior permanent magnet designs.

In [46], the open-circuit flux density on the rotor surface for interior permanent magnet machines with multiple magnets per pole is described analytically with a lumped magnetic circuit model. The reluctances in the model are calculated using the geometry of the rotor configuration. It is desired to describe the MMF and describe the permeance, separately. According to [47, 48], the flux density on the rotor surface, B_r, for buried magnet designs is proportional to the the flux density on the magnet surface, B_m, neglecting the magnet flux leakage. The constant of proportionality is the ratio of the total magnet width used in one pole, w_{mpp} to the pole-arc in meters, τ, as shown in Equation (5.9). This same constant of proportionality is used to describe the MMF on the rotor surface, Equation (5.10).

$$\mathcal{F}_m = H_c t_m \tag{5.8}$$

$$B_r = \frac{w_{mpp}}{\tau} B_m \tag{5.9}$$

$$\mathcal{F}_r = \frac{w_{mpp}}{\tau} \mathcal{F}_m \tag{5.10}$$

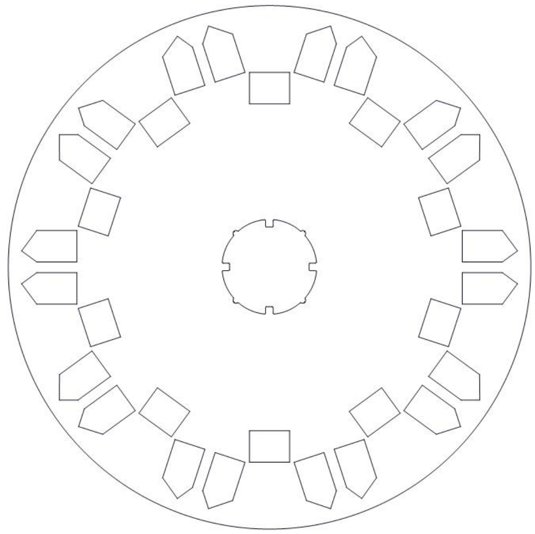

Figure 5.4: Single-layer Fractional Slot Concentrated Winding Rotor Configuration

The amplitude of the MMF for the $\frac{2}{5}SPP$ rotor configuration shown in Figure 5.4, where rectangular magnets are used to populate the slots, can also be described with Equation (5.10). The rotor MMF can be approximated as a square-wave approximation. The amplitude of the square-wave is determined by the angular position along the rotor. Above the magnets in each pole-arc the full amplitude of the MMF is assumed, as shown in Figure 5.5 for one pole pair. The trigonometric Fourier series of the square-wave function is shown in Figure 5.6 and Equation (5.11).

$$MMF_r\left(\phi_r\right) = \sum_{\eta=1}^{\infty} \frac{2\mathcal{F}_r}{\pi\eta} \sin\left(\eta p \frac{\tau}{2}\right) \left[\cos\left(\eta\pi\right) - 1\right] cos\left(\eta p \phi_r\right) \tag{5.11}$$

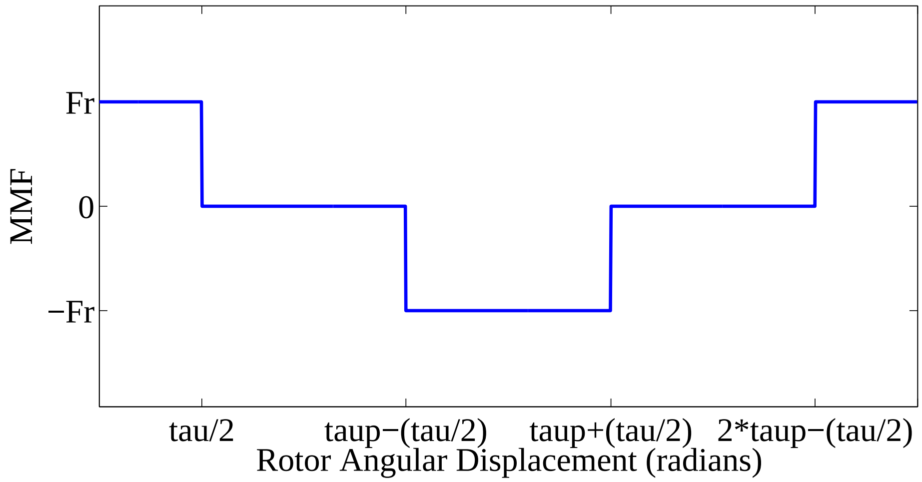

Figure 5.5: Square-wave Approximation of the single-layer fractional slot concentrated winding design rotor MMF distribution over one pole pair

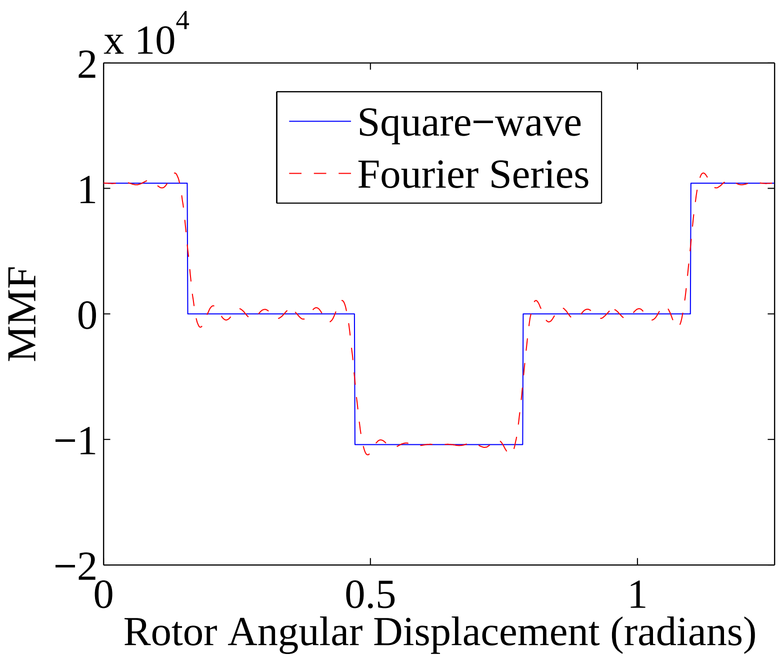

Figure 5.6: Trigonometric Fourier series of the single-layer fractional slot concentrated winding design rotor MMF distribution

5.3 Air-gap Permeance Variations Due to Rotor Slotting

The rotor configuration of the single-layer fractional slot concentrated winding design is shown in Figure 5.4. The slots in the rotor laminations lead to variations in the permeance. In [47, 48], the permeance function due to rotor slotting is described through the magnetic reluctance with the following assumptions:

- the stator is a slotless
- the flux excited by the current sheet flows radially in the air-gap
- there are only two flux paths, through
    1. the rotor iron only
    2. the center of the rotor pole

Following the same assumptions, with the inclusion of the infinite permeability of the stator and rotor iron, the reluctance variations due to the rotor slotting can be described as a square-wave function of the rotor angular displacement, shown in Figure 5.7. The reluctance over the magnet pole-arc, R_{pole}, is described in Equation (5.12), where h_s is the height of the slot. The reluctance over the remaining pole-pitch, R_{iron}, is described in Equation (5.13). The square-wave function is described using the trigonometric Fourier series, shown in Figure 5.8 and Equation (5.14).

$$R_{pole} = \frac{g}{\mu_0} + \frac{h_s}{\mu_0} \tag{5.12}$$

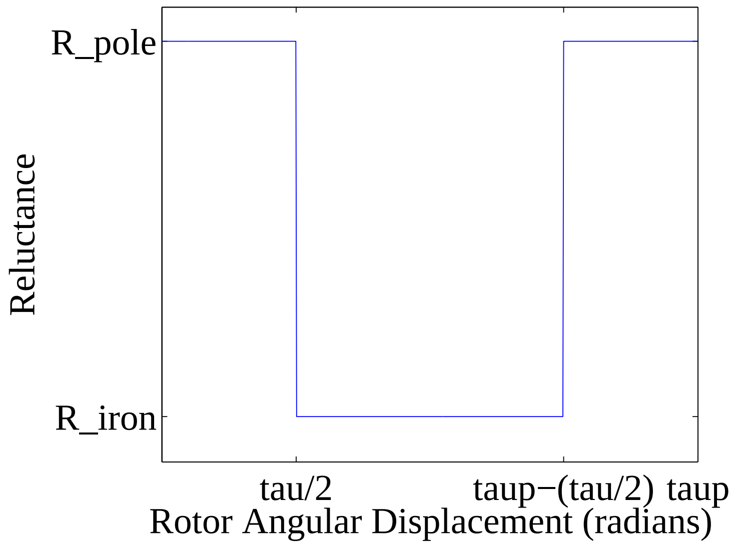

Figure 5.7: Square-wave Approximation of Reluctance Variation Due to Rotor Slotting in Singlelayer Fractional Slot Concentrated Winding PMSM

$$R_{iron} = \frac{g}{\mu_0} \tag{5.13}$$

$$R_r\left(\phi_r\right) = R_{iron} + \frac{\tau}{\tau_p}\left(R_{pole} - R_{iron}\right) + \sum_{\kappa=1}^{\infty} \frac{2}{\pi\kappa} \sin\left(\kappa p \tau\right)\left[R_{pole} - R_{iron}\right] cos\left(\kappa 2 p \phi_r\right) \tag{5.14}$$

5.4 Air-gap Permeance Variation Due to Stator Slotting

It is well known that the air-gap permeance varies due to the presence of slots in the stator. Carter's coefficient is conventionally used to account for the reduction of flux due to the stator slotting. As described in [25],Carter's coefficient, k_c, is multiplied by the physical measure of the air-gap, g, to find an equivalent air-gap length, g_e, which is constant,as

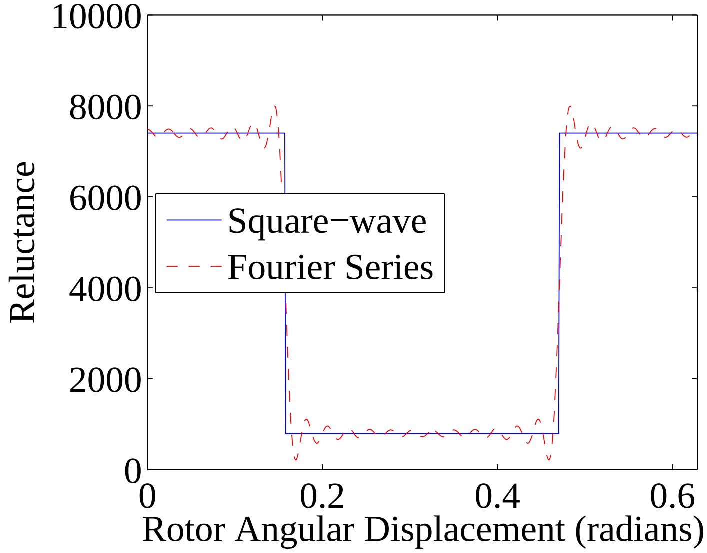

Figure 5.8: Square-wave Approximation of Reluctance Variation Due to Rotor Slotting in Singlelayer Fractional Slot Concentrated Winding PMSM

shown in Equation (5.15).

$$g_e = k_c g \tag{5.15}$$

An analytical description of the variations in the air-gap permeance due to stator slotting is desired. The authors of [47,48] describe a technique for including the effect of stator slotting in the permeance function. The magnetic reluctance is used to form a permeance function that captures the variations due to the stator slotting. In this technique the following assumptions are made:

- the rotor is slotless
- the flux excited by the magnets flows radially in the air-gap
- the flux excited by the magnets flows along a circular path around the slot opening to the stator tooth

The length of the path from the air-gap around the stator tooth is described in Equation (5.16), where r is the radius from the stator tooth.

$$l_s = \frac{1}{4} 2\pi r \tag{5.16}$$

The reluctance variations due to stator slotting are described for the $\frac{2}{5}SPP$ machine design following the same assumptions made in [47, 48], with the addition of infinite permeability of the stator and rotor iron. The radius around the stator tooth is assumed $\frac{1}{2}$ the width of the stator slot opening, w_{so}. The reluctance under a tooth is given in Equation (5.17). The reluctance under a slot opening is given in Equation (5.18). A square-wave function is used to describe the reluctance variations around the stator periphery. This function is shown in Figure 5.9 for one slot pitch, τ_s. This square-wave function is described by the trigonometric Fourier series is shown in Equation (5.19) and Figure 5.10.

$$R_t = \frac{g}{\mu_0} \tag{5.17}$$

$$R_{so} = \frac{g}{\mu_0} + \frac{\frac{1}{4}\left(2\pi\left(\frac{1}{2}w_{so}\right)\right)}{\mu_0} \tag{5.18}$$

$$R_s\left(\phi_s\right) = \frac{1}{\tau_s}\left(R_t w_t + R_{so} w_{so}\right) + \sum_{\kappa=1}^{\infty} \frac{2}{\pi\kappa} \sin\left(\kappa Q \frac{w_t}{2}\right)\left[R_t - R_{so}\right] cos\left(\kappa Q \phi_s\right) \tag{5.19}$$

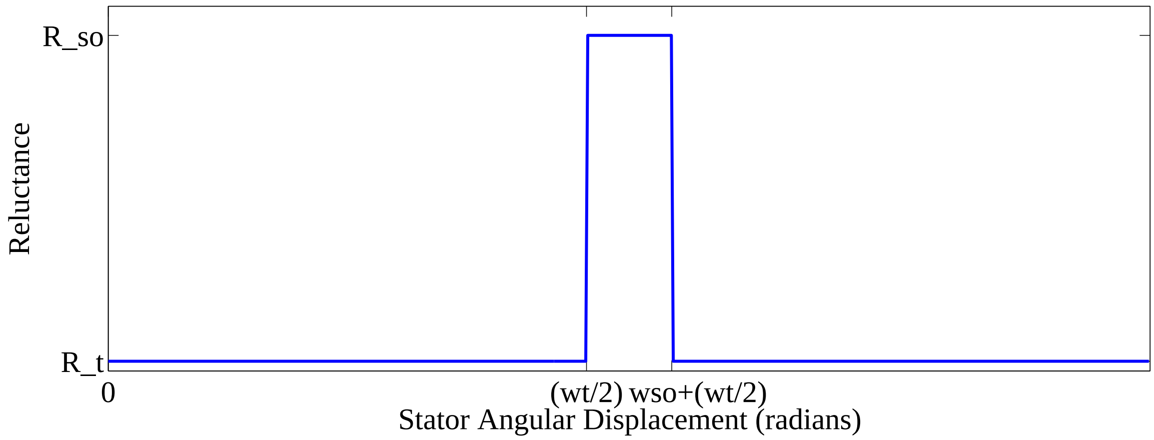

Figure 5.9: Square-wave approximation of Reluctance variations due to stator slotting over one slot pitch

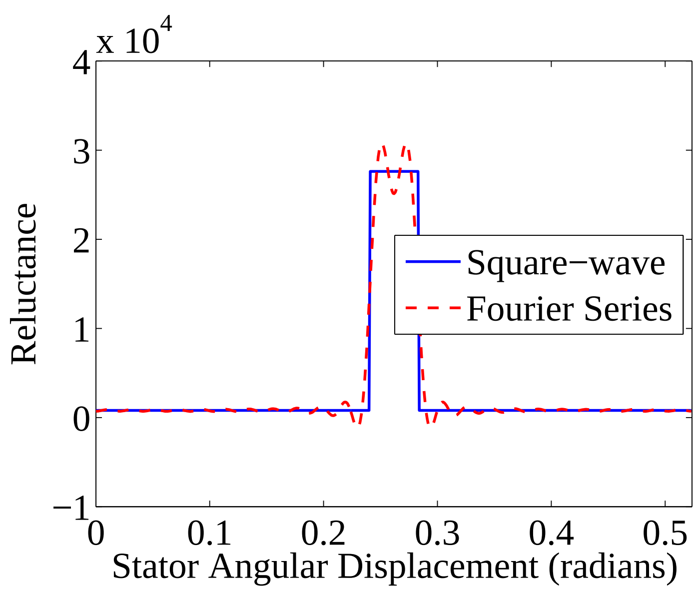

Figure 5.10: Square-wave approximation of Reluctance variations due to stator slotting over one slot pitch

5.5 Air-gap Flux Density

Air-gap flux density is the product of the air-gap MMF, $MMF_g(\phi_r)$, and the air-gap permeance, $\Lambda_g(\phi_r)$, as shown in Equation (5.27). The total air-gap MMF is the sum of the contributions from the stator, Equation (5.20), and rotor, Equation (5.21), as described in Equation (5.22).

$$\begin{aligned} MMF_s\left(\phi_r\right) &= \sum_{\nu=1}^{\infty} \frac{3N_t\hat{I}}{\nu\pi} \sin\left(\nu\frac{\pi}{Q}\right)\left[1-\cos\left(\nu\pi\right)\right]\cos\left(\nu\phi_r+(\nu-p)\theta_r-\delta\right) \\ &= \sum_{\nu=1}^{\infty} MMF_{s\nu}\cos\left(\nu\phi_r+\left(\nu-p\right)\theta_r-\delta\right) \end{aligned} \tag{5.20}$$

$$\begin{aligned} MMF_r\left(\phi_r\right) &= \sum_{\eta=1}^{\infty} \frac{2\mathcal{F}_r}{\pi\eta} \sin\left(\eta p\frac{\tau}{2}\right)\left[\cos\left(\eta\pi\right)-1\right] cos\left(\eta p\phi_r\right) \\ &= \sum_{\eta=1}^{\infty} MMF_{r\eta} cos\left(\eta p\phi_r\right) \end{aligned} \tag{5.21}$$

$$\begin{aligned} MMF_g\left(\phi_r\right) &= -MMF_s\left(\phi_r\right)+MMF_r\left(\phi_r\right) \\ &= \sum_{\eta=1}^{\infty} -MMF_{s\eta}\cos\left(\eta\phi_r+(\eta-p)\theta_r-\delta\right)+MMF_{r\eta} cos\left(\eta p\phi_r\right) \end{aligned} \tag{5.22}$$

The total air-gap permeance function is described as the inverse of the total air-gap reluctance variation, shown in Equation (5.26). The total air-gap reluctance variation is the sum of the reluctance variations due to rotor and stator slotting. However, since the reluctance variation due to rotor slotting assumed a smooth stator, it accounts for the reluctance below a stator tooth. For this reason, the reluctance under a stator tooth is subtracted from the the stator slotting contribution to the air-gap reluctance variations. The total air-gap reluctance is described in Equation (5.25).

$$\begin{aligned} R_s(\phi_r) &= \frac{1}{\tau_s}\left(R_t w_t + R_{so} w_{so}\right) + \sum_{\kappa=1}^{\infty} \frac{2}{\pi\kappa} \sin\left(\kappa Q \frac{w_t}{2}\right) \left[R_t - R_{so}\right] \cos\left(\kappa Q\left(\phi_r + \theta_r\right)\right) \\ &= R_{s0} + \sum_{\kappa=1}^{\infty} R_{s\kappa} \cos\left(\kappa Q\left(\phi_r + \theta_r\right)\right) \end{aligned} \tag{5.23}$$

$$\begin{aligned} R_r(\phi_r) &= R_{iron} + \frac{\tau}{\tau_p}\left(R_{pole} - R_{iron}\right) + \sum_{\kappa=1}^{\infty} \frac{2}{\pi\kappa} \sin\left(\kappa p \tau\right) \left[R_{pole} - R_{iron}\right] \cos\left(\kappa 2 p \phi_r\right) \\ &= R_{r0} + \sum_{\kappa=1}^{\infty} R_{r\kappa} \cos\left(\kappa 2 p \phi_r\right) \end{aligned} \tag{5.24}$$

$$\begin{aligned} R_g(\phi_r) &= \left(R_s(\phi_r) - R_t\right) + R_r(\phi_r) \\ &= R_{s0} - R_t + R_{r0} + \sum_{\kappa=1}^{\infty} R_{s\kappa} \cos\left(\kappa Q\left(\phi_r + \theta_r\right)\right) + R_{r\kappa} \cos\left(\kappa 2 p \phi_r\right) \\ &= R_{g0} + \sum_{\kappa=1}^{\infty} R_{s\kappa} \cos\left(\kappa Q\left(\phi_r + \theta_r\right)\right) + R_{r\kappa} \cos\left(\kappa 2 p \phi_r\right) \end{aligned} \tag{5.25}$$

$$\begin{aligned} \Lambda_g(\phi_r) &= \frac{1}{R_g(\phi_r)} \\ &= \Lambda_{g0} + \sum_{\kappa=1}^{\infty} \Lambda_{s\kappa} \cos\left(\kappa Q\left(\phi_r + \theta_r\right)\right) + \Lambda_{r\kappa} \cos\left(\kappa 2 p \phi_r\right) \end{aligned} \tag{5.26}$$

$$
\begin{aligned}
&B_g(\phi_r) = MMF_g(\phi_r)\,\Lambda_g(\phi_r) \\
&= \sum_{\kappa=1}^{\infty}\sum_{\eta=1}^{\infty}\Big\{\Lambda_{g0}MMF_{r\eta}\cos(\eta p\phi_r) - \Lambda_{g0}MMF_{s\eta}\cos(\eta\phi_r + (\eta - p)\theta_r - \delta) \\
&\qquad + \frac{\Lambda_{s\kappa}MMF_{r\eta}}{2}\left[\cos((\kappa Q - \eta p)\phi_r + \kappa Q\theta_r) + \cos((\kappa Q + \eta p)\phi_r + \kappa Q\theta_r)\right] \\
&\qquad - \frac{\Lambda_{s\kappa}MMF_{s\eta}}{2}\Big[\cos((\kappa Q - \eta)\phi_r + (\kappa Q - \eta + p)\theta_r + \delta) \\
&\qquad\qquad + \cos((\kappa Q + \eta)\phi_r + (\kappa Q + \eta - p)\theta_r - \delta)\Big] \\
&\qquad + \frac{\Lambda_{r\kappa}MMF_{r\eta}}{2}\Big[\cos((\kappa 2 - \eta)p\phi_r) + \cos((\kappa 2 + \eta)p\phi_r)\Big] \\
&\qquad - \frac{\Lambda_{r\kappa}MMF_{s\eta}}{2}\Big[\cos((\kappa 2p - \eta)\phi_r - (\eta - p)\theta_r + \delta) \\
&\qquad\qquad + \cos((\kappa 2p + \eta)\phi_r + (\eta - p)\theta_r - \delta)\Big]\Big\}
\end{aligned}
\tag{5.27}
$$

5.6 Analytical Torque Expression

Torque is described in Equation (5.29) where L is the motor stack length and r_{s-id} is the inner radius of the stator. Total air-gap flux density, $B_g(\phi_r)$ is shown in Equation (5.27). The linear current density, $K_s(\phi_r)$ is described in Equation (5.28). The integrand, shown in Equation (5.30), is only non-zero when the coefficient of ϕ_r is equal to zero. The conditions for non-zero torque are shown in Equation (5.31).

$$
K_s(\phi_r) = \sum_{\nu=1}^{\infty}\frac{3N_t\hat{I}}{\nu\pi r_{s-id}}\sin\left(\nu\frac{\pi}{Q}\right)\left[1 - \cos(\nu\pi)\right]\cos(\nu\phi_r + (\nu - p)\theta_r - \delta) \tag{5.28}
$$

$$
T = Lr_{s-id}^2\int_0^{2\pi} B_g(\phi_r)\,K_s(\phi_r)\,d\phi_r \tag{5.29}
$$

$$
\begin{aligned}
B_g(\phi_r)K_s(\phi_r) = \sum_{\kappa=1}^{\infty}\sum_{\eta=1}^{\infty}\sum_{\nu=1}^{\infty}\Bigg\{ & \frac{\Lambda_{g0}MMF_{r\eta}K_{s\nu}}{2}\Big[\cos\left((\eta p-\nu)\phi_r-(\nu-p)\theta_r+\delta\right) \\
& +\cos\left((\eta p+\nu)\phi_r+(\nu-p)\theta_r-\delta\right)\Big] \\
& -\frac{\Lambda_{g0}MMF_{s\eta}K_{s\nu}}{2}\Big[\cos\left((\eta-\nu)\phi_r+(\eta-\nu)\theta_r\right) \\
& +\cos\left((\eta+\nu)\phi_r+(\eta+\nu-2p)\theta_r-2\delta\right)\Big] \\
& +\frac{\Lambda_{s\kappa}MMF_{r\eta}K_{s\nu}}{4}\Big[\cos\left((\kappa Q-\eta p-\nu)\phi_r+(\kappa Q-\nu+p)\theta_r+\delta\right) \\
& +\cos\left((\kappa Q-\eta p+\nu)\phi_r+(\kappa Q+\nu-p)\theta_r-\delta\right) \\
& +\cos\left((\kappa Q+\eta p-\nu)\phi_r+(\kappa Q-\nu+p)\theta_r+\delta\right) \\
& +\cos\left((\kappa Q+\eta p+\nu)\phi_r+(\kappa Q+\nu-p)\theta_r-\delta\right)\Big] \\
& -\frac{\Lambda_{s\kappa}MMF_{s\eta}K_{s\nu}}{4}\Big[\cos\left((\kappa Q-\eta-\nu)\phi_r+(\kappa Q-\eta-\nu+2p)\theta_r+2\delta\right) \\
& +\cos\left((\kappa Q-\eta+\nu)\phi_r+(\kappa Q-\eta+\nu)\theta_r\right) \qquad (5.30) \\
& +cos\left((\kappa Q+\eta-\nu)\phi_r+(\kappa Q+\eta-\nu)\theta_r\right) \\
& +\cos\left((\kappa Q+\eta+\nu)\phi_r+(\kappa Q+\eta+\nu-2p)\theta_r-2\delta\right)\Big] \\
& +\frac{\Lambda_{r\kappa}MMF_{r\eta}K_{s\nu}}{4}\Big[\cos\left((\kappa 2p-\eta p-\nu)\phi_r-(\nu-p)\theta_r+\delta\right) \\
& +\cos\left((\kappa 2p-\eta p+\nu)\phi_r+(\nu-p)\theta_r-\delta\right) \\
& +\cos\left((\kappa 2p+\eta p-\nu)\phi_r-(\nu-p)\theta_r+\delta\right) \\
& +\cos\left((\kappa 2p+\eta p+\nu)\phi_r+(\nu-p)\theta_r-\delta\right)\Big] \\
& -\frac{\Lambda_{r\kappa}MMF_{s\eta}K_{s\nu}}{4}\Big[\cos\left((\kappa 2p-\eta-\nu)\phi_r+(2p-\eta-\nu)\theta_r+\delta\right) \\
& +\cos\left((\kappa 2p-\eta+\nu)\phi_r+(\nu-\eta)\theta_r-\delta\right)+\cos\left((\kappa 2p+\eta-\nu)\phi_r+(\eta-\nu)\theta_r\right) \\
& +\cos\left((\kappa 2p+\eta+\nu)\phi_r+(\nu+\eta-2p)\theta_r-2\delta\right)\Big]\Bigg\}
\end{aligned}
$$

$$T \neq 0 \begin{cases} \eta p = \nu \\ \eta p = \nu \quad \text{and } \kappa = \eta \\ \eta p = \nu \quad \text{and } \kappa = \frac{\eta(p-1)}{Q} \\ \eta p = \nu \quad \text{and } \kappa = \frac{\eta(1+p)}{2p} \\ \eta p = \nu \quad \text{and } \kappa = \frac{\eta(p-1)}{2p} \\ \eta = \nu \\ \eta = \nu \quad \text{and } \kappa = \frac{\eta(p-1)}{Q} \\ \eta = \nu \quad \text{and } \kappa = \frac{\eta(p+1)}{2p} \\ \eta = \nu \quad \text{and } \kappa = \frac{\eta(p-1)}{2p} \\ \eta = \nu \quad \text{and } \kappa = \frac{\eta}{p} \end{cases} \tag{5.31}$$

The resulting torque expression is shown in Equation (5.32).

$$
\begin{aligned}
T = \pi L r_{s-id}^2 \Bigg\{ \sum_{\eta=1}^{\infty} \Bigg[& \Lambda_{g0} MMF_{r\eta} K_{s\eta p} \cos\left(-(\eta p - p)\theta_r + \delta\right) \\
& - \Lambda_{g0} MMF_{s\eta} K_{s\eta} \\
& + \frac{\Lambda_{r\eta} MMF_{r\eta} K_{s\eta p}}{2} \cos\left(-(\eta p - p)\theta_r + \delta\right) \Bigg] \\
+ \sum_{\eta=3,9,15}^{\infty} \frac{1}{2} \Bigg[& - \Lambda_{s\frac{\eta(p-1)}{Q}} MMF_{s\eta} K_{s\eta p} \\
& + \Lambda_{s\frac{\eta(p-1)}{Q}} MMF_{r\eta} K_{s\eta} \cos\left((\eta p - p)\theta_r - \delta\right) \Bigg] \\
+ \sum_{\eta=5,15,25}^{\infty} \frac{1}{2} \Bigg[& - \Lambda_{r\frac{\eta(p+1)}{2p}} MMF_{s\eta} K_{s\eta p} \cos\left((2p - \eta - \eta p)\theta_r + \delta\right) \\
& + \Lambda_{r\frac{\eta(p+1)}{2p}} MMF_{r\eta} K_{s\eta} \cos\left(-(\eta - p)\theta_r + \delta\right) \\
& - \Lambda_{r\frac{\eta(p-1)}{2p}} MMF_{s\eta} K_{s\eta p} \cos\left((\eta - \eta p)\theta_r\right) \\
& + \Lambda_{r\frac{\eta(p-1)}{2p}} MMF_{r\eta} K_{s\eta} \cos\left((\eta - p)\theta_r - \delta\right) \\
& - \Lambda_{r\frac{\eta}{p}} MMF_{s\eta} K_{s\eta} \cos\left((2p - 2\eta)\theta_r + \delta\right) \Bigg] \Bigg\}
\end{aligned}
\tag{5.32}
$$

The analytical expression given in Equation (5.32) was simulated with MATLAB. The MATLAB FSCW machine model includes the first two non-zero harmonic interactions between the rotor and stator, $\eta = 1\&3$, as shown in Equation (5.33) at 300rpm. The results of the analytical model at two current levels are compared to the torque produced at the same current levels in the finite element model of the single-layer $\frac{2}{5}SPP$ machine. As shown in Figures 5.11 and 5.12, Equation (5.32) closely approximates the finite element results.

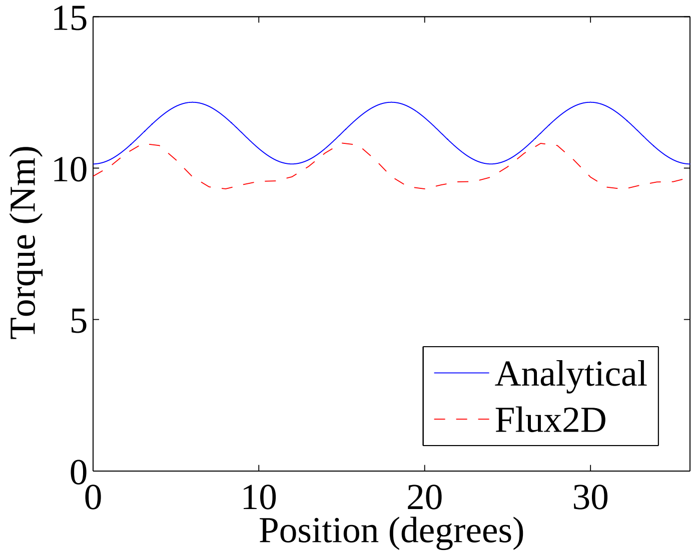

Figure 5.11: Simulink model of analytical torque expression

$$
\begin{aligned}
T = \pi L r_{s-id}^2 \Bigg\{ \sum_{\eta=1}^{3} MMF_{r\eta} K_{s\eta p} \cos\left(-(\eta p - p)\theta_r + \delta\right) \left[\Lambda_{g0} + \frac{\Lambda_{r\eta}}{2}\right] \\
+ \frac{1}{2} \Lambda_{s\frac{3(p-1)}{Q}} MMF_{r3} K_{s3} \cos\left((3p - p)\theta_r - \delta\right) \Bigg\}
\end{aligned}
\tag{5.33}
$$

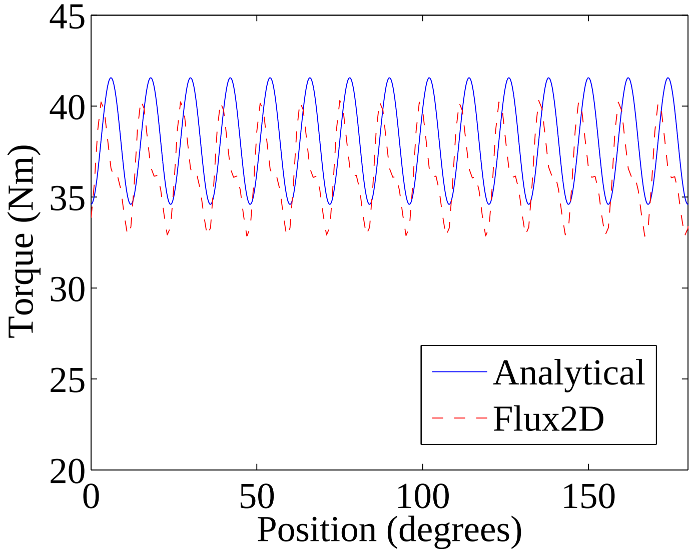

Figure 5.12: Simulink model of analytical torque expression

Chapter 6

Torque Ripple Reduction Control

The single-layer fractional slot concentrated winding design provides the best isolation between phases. In the event of a stator winding inter-turn short circuit, the single-layer design best limits circulating current. This winding configuration provides highest reliability; however, the torque ripple associated with this design is undesirable, nearly 30% of the average torque.

In this chapter, a permanent magnet synchronous machine controller is modified to include torque ripple estimation. The estimation is used to decrease the torque ripple of the single-layer fractional slot concentrated winding design. The losses associated with this controller are also evaluated.

6.1 PMSM Controller Development

Two regions of operation can be defined by the torque speed curve of the permanent magnet synchronous machine, shown in Figure 6.1:

1. the region below base speed or the constant torque region
2. the region above base speed or the field weakening region

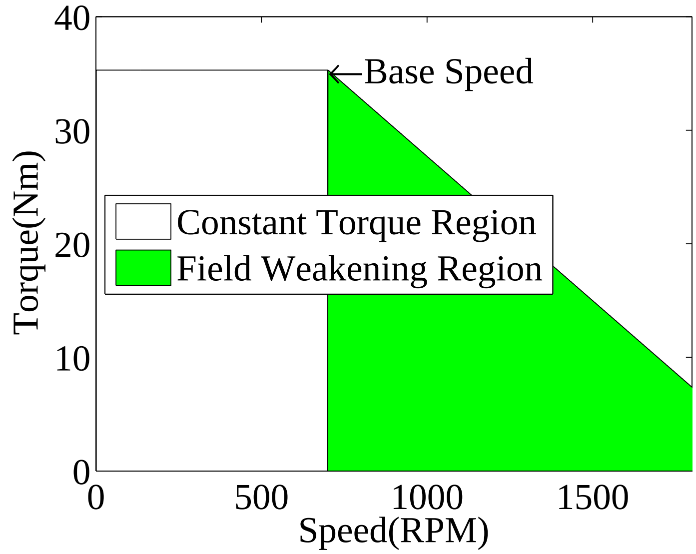

Figure 6.1: Permanent magnet synchronous machine regions of operation defined by the torque speed curve.

In the constant torque region, the maximum current, I_{max} is the only restriction because the induced voltage remains below the maximum. In this region, the angle at which the current is applied, δ, remains constant. Equation (6.3) is applied to Equation (6.4) to determine the current angle, δ, in this region, shown in Equation (6.5).

$$i_d = I_{max} \cos(\delta) \tag{6.1}$$

$$i_q = I_{max} \sin(\delta) \tag{6.2}$$

$$\frac{d\left(\frac{T}{I_{max}}\right)}{d\delta} = 0 \tag{6.3}$$

$$T = \frac{3p}{2}\left[\lambda_{pm} + \left(L_d - L_q\right) I_{max} \cos(\delta)\right] I_{max} \sin(\delta) \tag{6.4}$$

$$\delta = \cos^{-1}\left(\frac{-\lambda_{pm} + \sqrt{\lambda_{pm}^2 + 8\left(L_d - L_q\right)^2 I_{max}^2}}{4\left(L_d - L_q\right) I_{max}}\right) \tag{6.5}$$

Once the machine exceeds base speed, entering the field weakening region, the induced voltage reaches the maximum voltage, V_{max}, requiring that the magnet flux is controlled to restrict the voltage. Control of the magnet flux is achieved through adjustments in the angle at which the current, I_s, is applied. Substituting Equations (4.35) and (4.36) for maximum current (I_{max}) into the maximum steady-state voltage equation Equation (6.6), neglecting the resistive drop. Applying the quadratic equation results in Equation (6.7)

$$V_{max}^2 = v_d^2 + v_q^2 \tag{6.6}$$

$$\delta = \cos^{-1}\left(\frac{-2L_d\lambda_{pm}I_{max} \pm \sqrt{\left(2L_d\lambda_{pm}I_{max}\right)^2 - 4I_{max}^2\left(L_d^2 - L_q^2\right)\left(L_q^2 I_{max}^2 + \lambda_{pm}^2 - \frac{V_{max}^2}{\omega_e^2}\right)}}{2\left(L_d^2 - L_q^2\right) I_{max}^2}\right) \tag{6.7}$$

The model-based torque controller is shown in Figure 6.2. The performance of this control algorithm is directly dependent on the accuracy of the parameters. The machine parameters are included in the controller as piece-wise approximations. In this controller, the d- and q-axis inductances of the single-layer $\frac{2}{5}SPP$ machine found in finite element are separated into three sections to develop the piece-wise approximations, as shown in Figure 6.3. Inductances in section I and II are described as linear functions of current. In section III, the inductances are described as 2^{nd}-order polynomials. As shown in Figure 6.3, these function closely approximate the inductances.

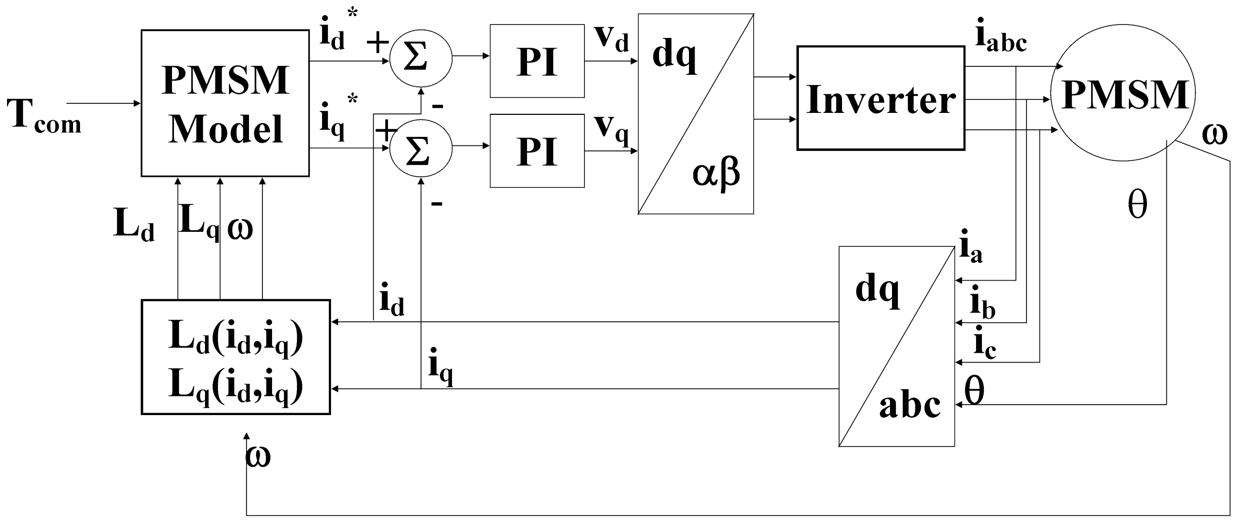

Figure 6.2: PMSM model-based controller

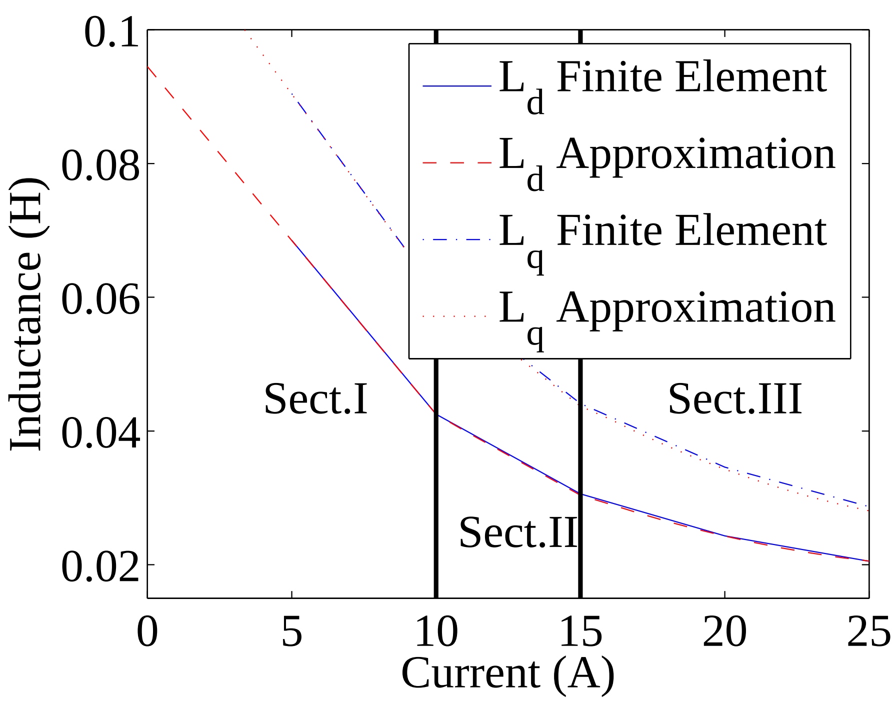

Figure 6.3: Comparison of finite element single-layer $\frac{2}{5}$ SPP PMSM inductances to piece-wise approximation.

6.2 Torque Ripple Estimation

The analytical description of torque given in Equation (5.32) can be divided into two components:

- DC Torque Component
- Torque Ripple Component

The DC component of torque is shown in Equation (6.8). All other values of η, ν and κ contribute to torque ripple as shown in Equation (6.9).

$$\begin{aligned} T_{DC} = \pi L r_{s-id}^2 \Bigg\{ & MMF_{r1} K_{sp} \cos(\delta) \left[\Lambda_{g0} + \frac{\Lambda_{r1}}{2} \right] \\ & - \sum_{\eta=1}^{\infty} \Lambda_{g0} MMF_{s\eta} K_{s\eta} \\ & - \sum_{\eta=3,9,15}^{\infty} \Lambda_{s\frac{\eta(p-1)}{Q}} MMF_{s\eta} K_{s\eta p} \Bigg\} \end{aligned} \tag{6.8}$$

$$
\begin{aligned}
T_{ripple} = \pi L r_{s-id}^2 \Bigg\{ \sum_{\eta=3}^{\infty} \Bigg[& \Lambda_{g0} MMF_{r\eta} K_{s\eta p} \cos\left(-(\eta p - p)\theta_r + \delta\right) \\
& + \frac{\Lambda_{r\eta} MMF_{r\eta} K_{s\eta p}}{2} \cos\left(-(\eta p - p)\theta_r + \delta\right) \Bigg] \\
\sum_{\eta=3,9,15}^{\infty} \frac{1}{2} \Bigg[& \Lambda_{s\frac{\eta(p-1)}{Q}} MMF_{r\eta} K_{s\eta} \cos\left((\eta p - p)\theta_r - \delta\right) \Bigg] \\
\sum_{\eta=5,15,25}^{\infty} \frac{1}{2} \Bigg[& - \Lambda_{r\frac{\eta(p+1)}{2p}} MMF_{s\eta} K_{s\eta p} \cos\left((2p - \eta - \eta p)\theta_r + \delta\right) \\
& + \Lambda_{r\frac{\eta(p+1)}{2p}} MMF_{r\eta} K_{s\eta} \cos\left(-(\eta - p)\theta_r + \delta\right) \\
& - \Lambda_{r\frac{\eta(p-1)}{2p}} MMF_{s\eta} K_{s\eta p} \cos\left((\eta - \eta p)\theta_r\right) \\
& + \Lambda_{r\frac{\eta(p-1)}{2p}} MMF_{r\eta} K_{s\eta} \cos\left((\eta - p)\theta_r - \delta\right) \\
& - \Lambda_{r\frac{\eta}{p}} MMF_{s\eta} K_{s\eta} \cos\left((2p - 2\eta)\theta_r + \delta\right) \Bigg] \Bigg\}
\end{aligned}
\tag{6.9}
$$

The largest rotor MMF component beyond the fundamental that contributes to the torque ripple is the 3^{rd} harmonic, as shown in Figure 6.4. This harmonic interacts with both the 3^{rd} and 15^{th} harmonic of the linear current density to produce torque ripple. Only using the 3^{rd} harmonic of the rotor MMF in the ripple estimator, $ripple_calc$, shown in Figure 6.5, the torque ripple is estimated for a 35Nm torque command, from the current command and rotor position. The peak-to-peak amplitude is approximately 7Nm. This nearly 70% of the torque ripple found with finite element for the same torque level. Finite element verified that the frequency of the torque ripple is a spatial quantity, as shown in Figure 6.7, the period of the torque ripple is not affected by machine speed.

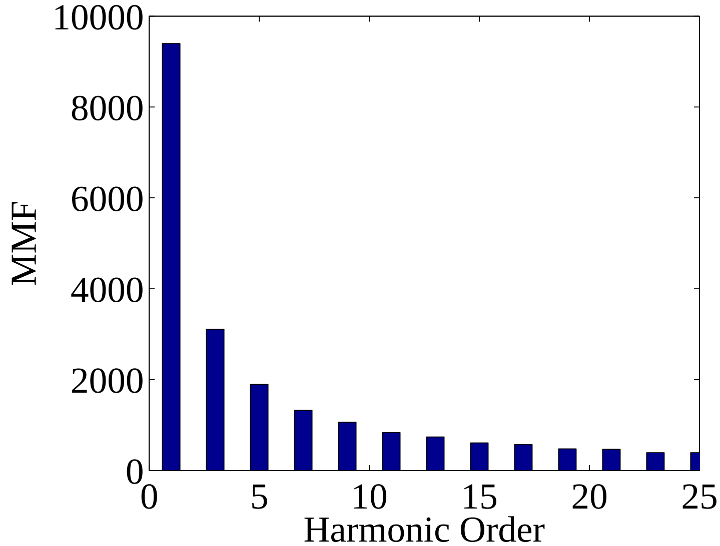

Figure 6.4: Magnitude of rotor MMF harmonic components in single-layer $\frac{2}{5}$ SPP PMSM

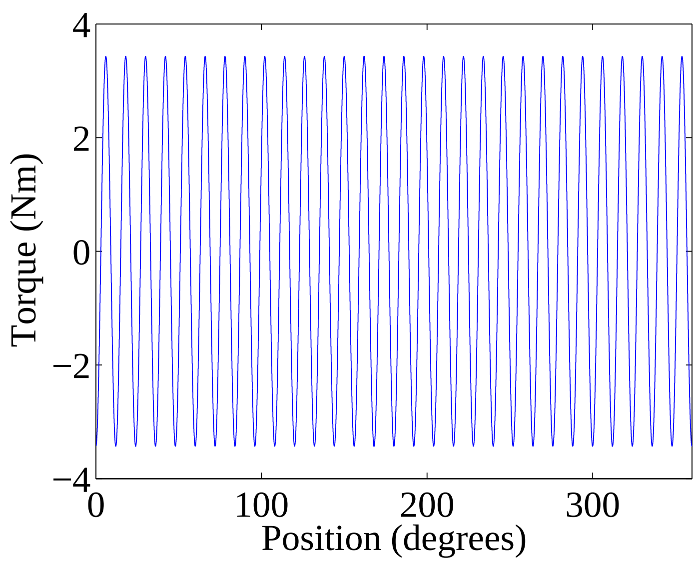

Figure 6.5: Estimated torque ripple for 35Nm command in single-layer $\frac{2}{5}$ SPP PMSM

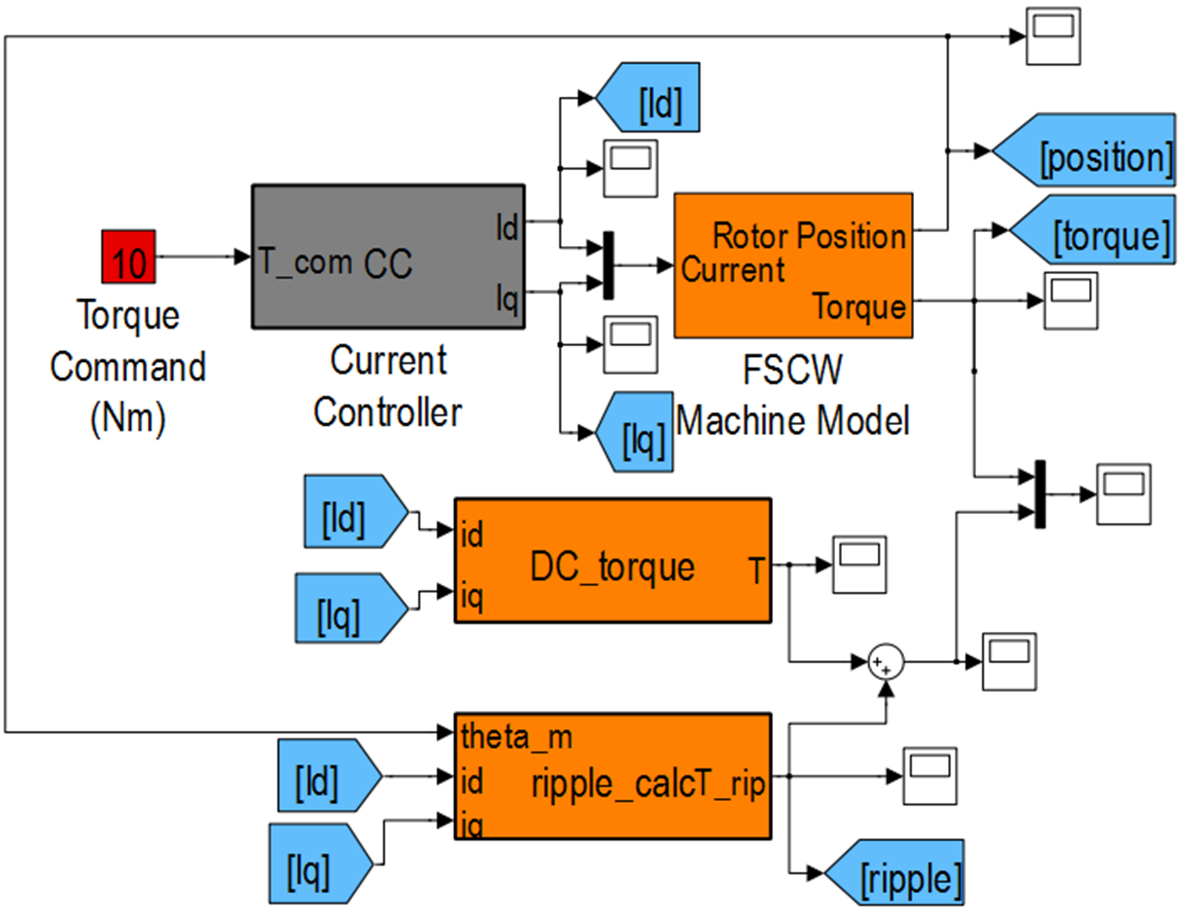

Figure 6.6: Analytical Torque Ripple Estimation

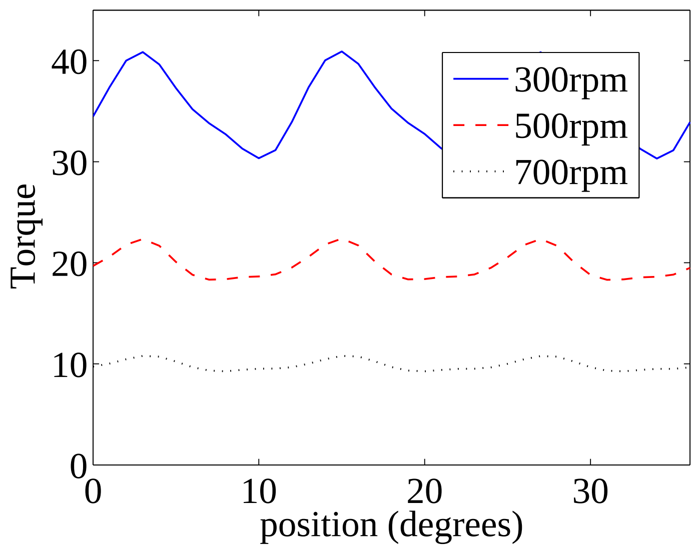

Figure 6.7: Finite element torque ripple at varying speeds and torques

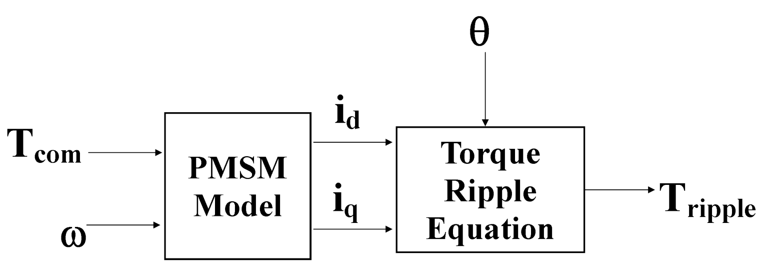

Figure 6.8: Torque ripple estimator

6.3 Ripple Reduction Technique

A priori estimation of torque ripple can be used to reduce torque ripple. In the PMSM controller presented in Section 6.1, i_d and i_q are determined from the PMSM model in Equation (6.4). The estimation of torque ripple can be implemented on-line with current, rotor position and the torque command, as shown in Figure 6.8. The PMSM model in Figure 6.8 is populated with ideal inductances.

The torque ripple estimation can be used to modify the torque command as shown

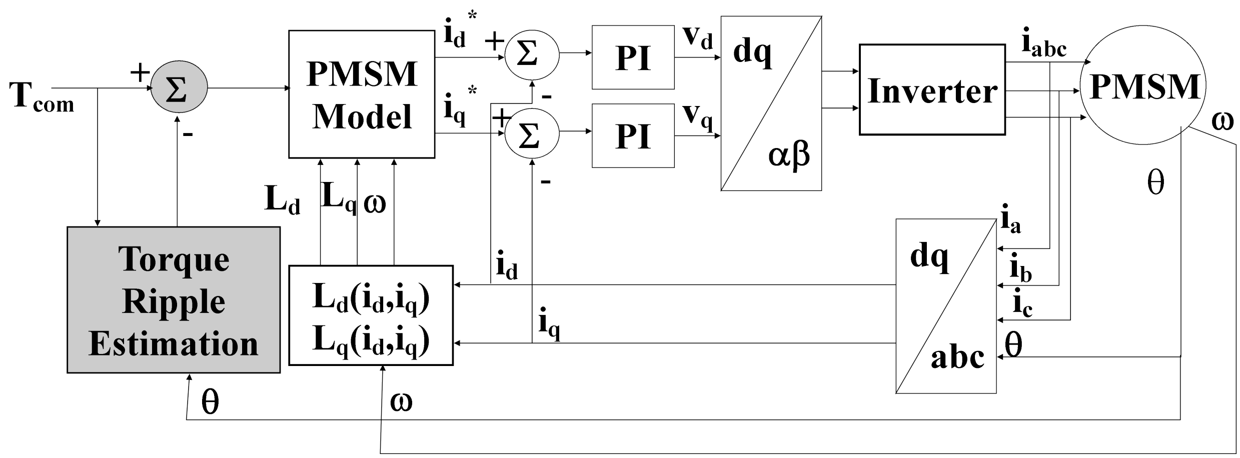

Figure 6.9: Torque ripple compensation controller

in Figure 6.9. This technique generates sinusoidal d- and q-axis current commands. This technique was verified in Simulink using the model shown in Figure 6.10. The resulting reduction is shown for a 10 Nm command in Figure 6.11

6.4 Finite Element Results

The ripple compensation controller, shown in Figure 6.9 was implemented with the single-layer $\frac{2}{5}$ SPP machine model in finite element. The torque ripple estimation only includes the contribution from the 3^{rd} harmonic of the rotor MMF. The results are shown for the 10Nm, 20Nm and 35Nm cases in Figures 6.12 to 6.14. A priori estimation of reduced torque ripple in the single-layer design by as much as 70%, see Table 6.1. The frequency of the torque ripple increased in some cases, however the amplitude is reduced. The increased frequency is a result of remaining higher order harmonic content.

This technique increase the harmonic content of the current commands, which may result

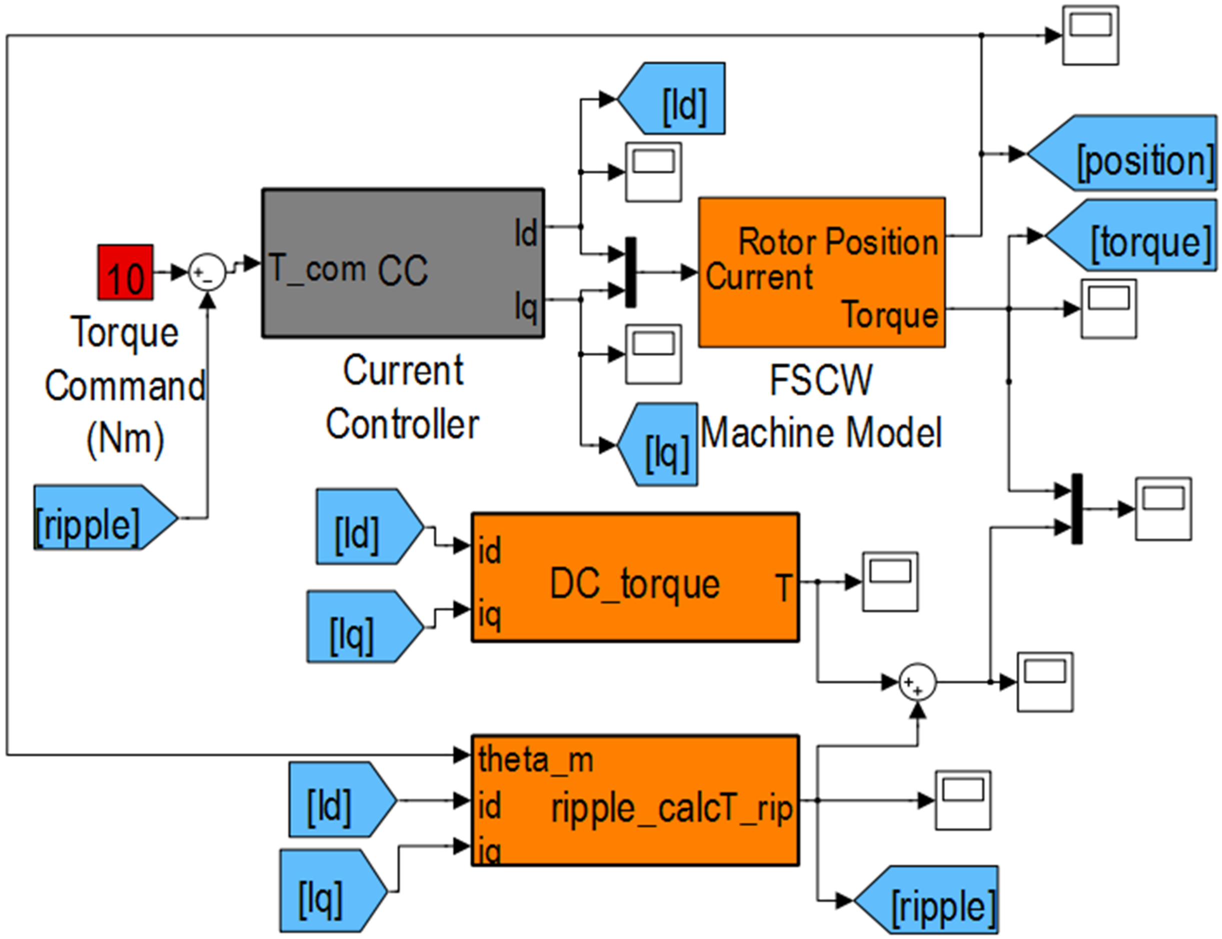

Figure 6.10: Simulink model of torque compensation

Torque Command (Nm)	Torque Ripple		Percent Change (%)
	Without Compensation	With Compensation	
10	1.53	.453	-70%
20	4.11	1.44	-64.96%
35	10.59	3.92	-62.98%

Table 6.1: Change in torque ripple due to implementation of the ripple compensation control on $\frac{2}{5}$ SPP PM machine.

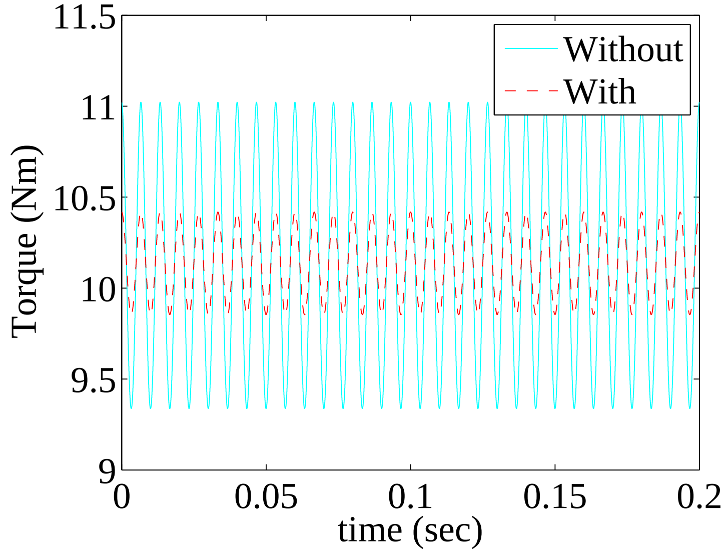

Figure 6.11: Torque for 10Nm command with and without the torque ripple compensation controller.

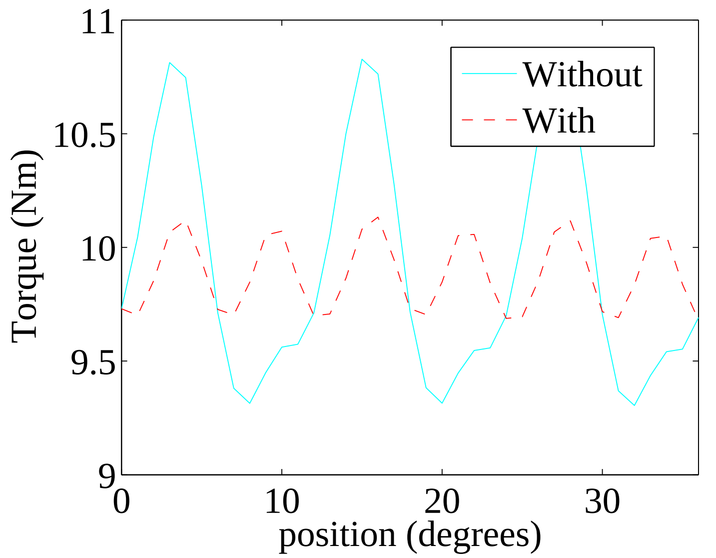

Figure 6.12: Finite element results 10Nm torque command with and without the torque ripple compensation controller.

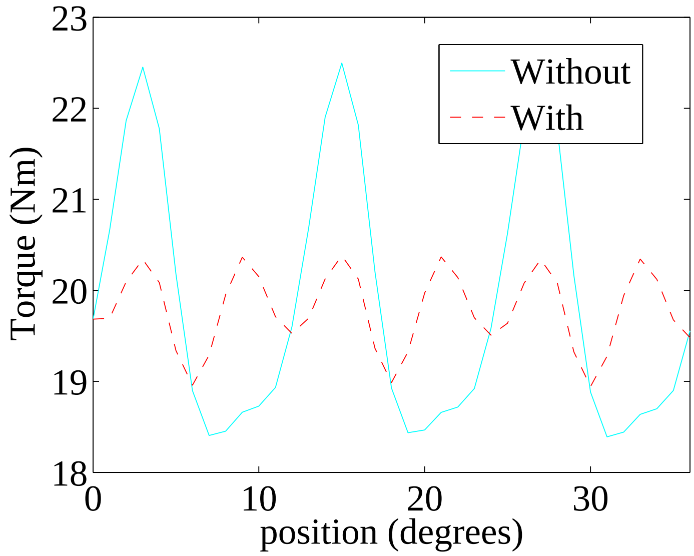

Figure 6.13: Finite element results 20Nm torque command with and without the torque ripple compensation controller.

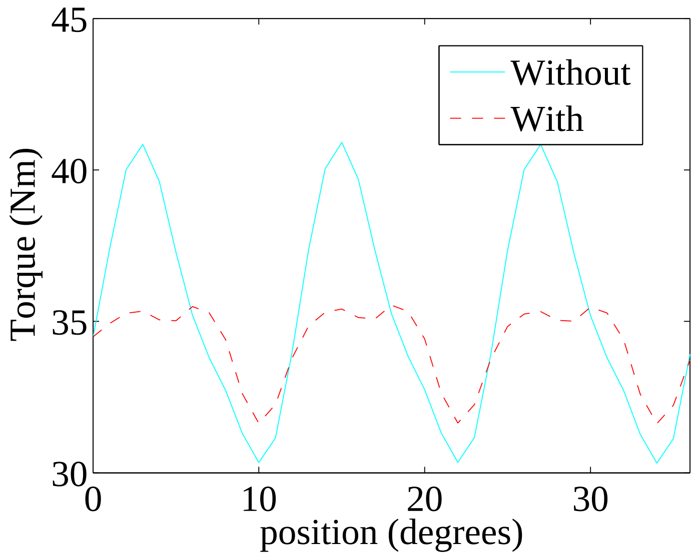

Figure 6.14: Finite element results 35Nm torque command with and without the torque ripple compensation controller.

Torque Command (Nm)	Loss Type			
			Iron	
	Magnet	Copper	Hysteresis	Eddy Current
10	0%	+.5%	+3%	+2%
20	+2%	+1.5%	+.5%	+3%
35	+15%	+8%	0%	+4%

Table 6.2: Change in machine losses due to implementation of the ripple reduction control on $\frac{2}{5}$ SPP PM machine.

in higher losses. The losses associated with the decreased torque ripple were evaluated in finite element. Magnet losses increase by as much as 15% at high torque, as shown in Table 6.2.; however, the ripple compensation control is effective for reducing torque ripple in the single-layer $\frac{2}{5}$ SPP machine design.

Chapter 7

Detection of Stator Winding Insulation Degradation in Fault Tolerant PM Machines

Most winding faults are caused by insulation deterioration, resulting from thermal stress due to aging, overloading, cycling or fast switching of the inverter, which implies that designing fault tolerant machines will not eliminate winding fault occurrences. Deteriorated winding insulation will lead to an inter-turn short circuit overtime, without corrective measures. The time between a single inter-turn short circuit and catastrophic failure of the machine is short. Without knowledge of degrading stator winding insulation, a stator inter-turn short could develop and lead to catastrophic failure. Catastrophic permanent magnet machine failure can be avoided if degrading stator winding insulation is detected during normal operation. Detecting the degradation prior to the existence of a turn-to-turn short circuit would allow for timely maintenance and repair.

Off-line techniques for detecting insulation degradation are commonly implemented as part of the machine's preventive maintenance schedule. The surge test, DC conductivity test, insulation resistance test, DC/AC HiPot test and the polarization index test are examples of off-line techniques used to check health of stator winding insulation [2].

In this chapter, the effect of degrading insulation on the machine performance is evaluated. Parametric changes due to degraded insulation is demonstrated. Extracted machine parameters are used to identify a means to monitor the condition of the stator winding insulation.

7.1 Winding Insulation Degradation and Machine Performance

The open-circuit voltage is affected as winding insulation degrades, even before the presence of a short-circuit. The changes in open-circuit voltage are directly related to the circulating current. Varying the fault resistance in the finite element model simulates insulation degradation. Machine speed and the number of turns in which the insulation has degraded affect the magnitude of the circulating current, as shown in Figures 7.1 and 7.2. The shape of the open-circuit voltage deformation is consistent regardless of machine speed, as shown in Figures 7.3 and 7.4. However, the number of turns with degraded insulation determines the level of deformation, or the harmonic spectrum, as shown in Figures 7.5 to 7.7.

As with shorted inter-turns, the machine torque ripple increases with the number of turns with degraded insulation, shown in Table 7.1. The ability to detect that the winding insulation is degrading during machine operation offers opportunity to mitigate the fault and maintain decent machine performance.

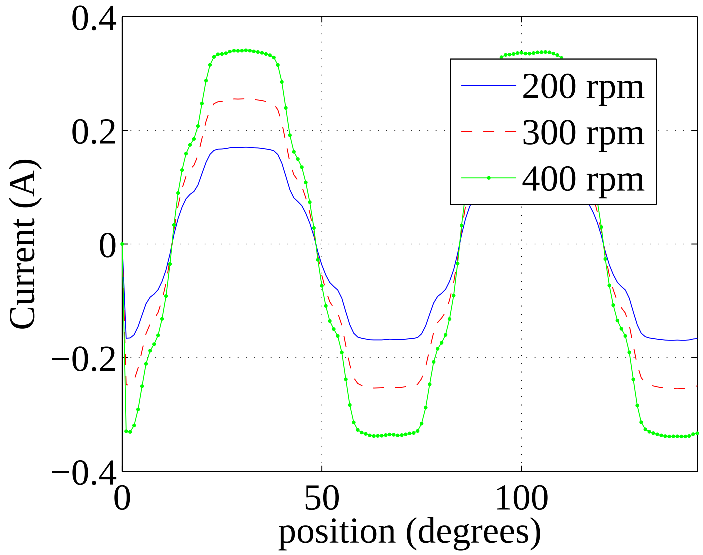

Figure 7.1: Circulating Current in Single-layer $\frac{2}{5}$SPP Permanent Magnet Synchronous Machine with Single-turn Insulation Degraded at Different Speeds - (a)200 rpm (b)300 rpm (c)400 rpm (finite element results)

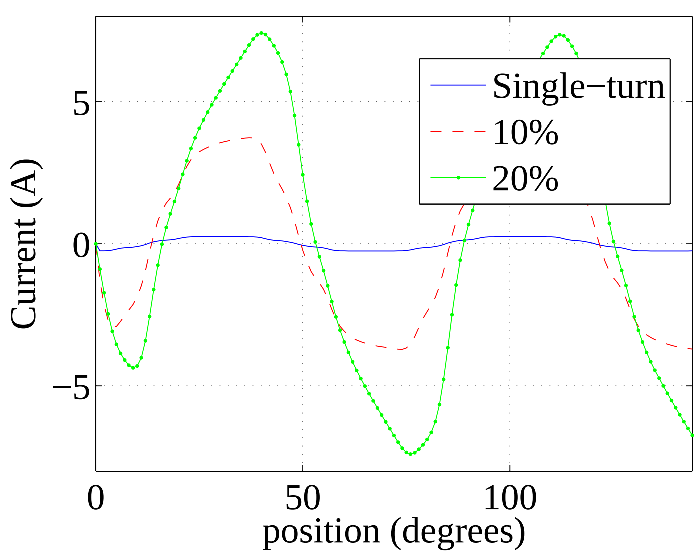

Figure 7.2: Circulating Current in Single-layer $\frac{2}{5}$SPP Permanent Magnet Synchronous Machine with Insulation Degraded in Different Number of Turns at 300 rpm - (a)Single-turn in Slot (b)10% Turns in Slot (c)20% Turns in Slot (finite element results)

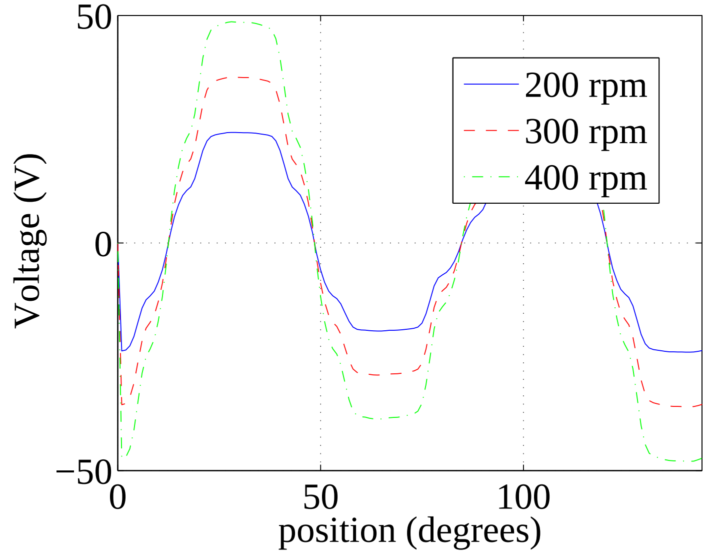

Figure 7.3: Open-Circuit Voltage (at Different Speeds) in Single-layer $\frac{2}{5}$SPP Permanent Magnet Synchronous Machine with the Insulation on a Single-turn in a Slot Degraded - (a)200 rpm (b)300 rpm (c)400 rpm (finite element results)

Figure 7.4: Open-Circuit Voltage (at Different Speeds) in Single-layer $\frac{2}{5}$SPP Permanent Magnet Synchronous Machine with the Insulation of 20% of the Turns in a Slot Degraded - (a)200 rpm (b)300 rpm (c)400 rpm (finite element results)

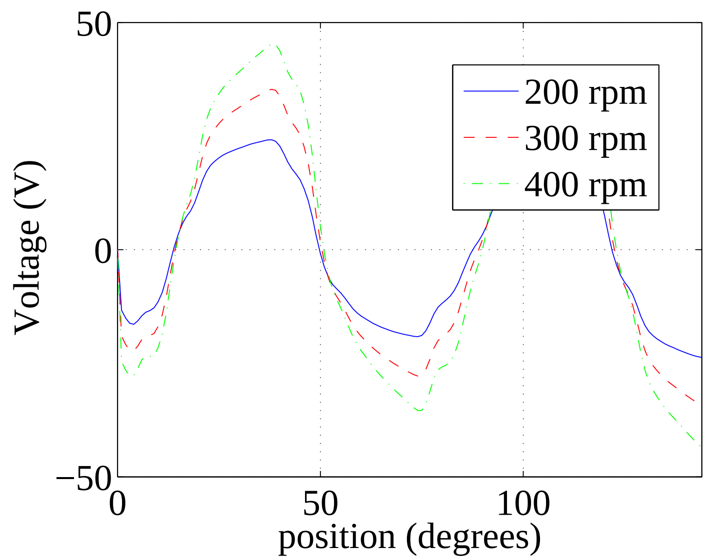

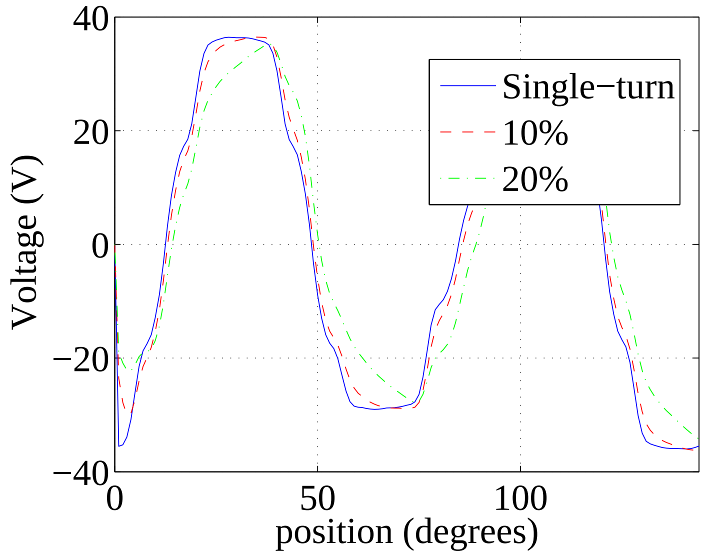

Figure 7.5: Open-Circuit Voltage in Single-layer $\frac{2}{5}$SPP Permanent Magnet Synchronous Machine with Insulation Degraded in Different Number of Turns at 300 rpm - (a)Single-turn in Slot (b)10% Turns in Slot (c)20% Turns in Slot (finite element results)

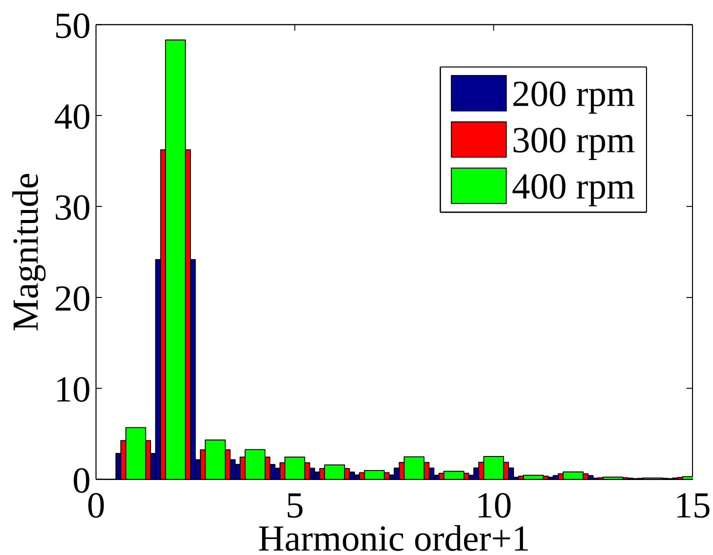

Figure 7.6: Harmonic Spectrum of Open-Circuit Voltage in Single-layer $\frac{2}{5}$SPP Permanent Magnet Synchronous Machine with Insulation Degraded Across a Single-turn in a Slot

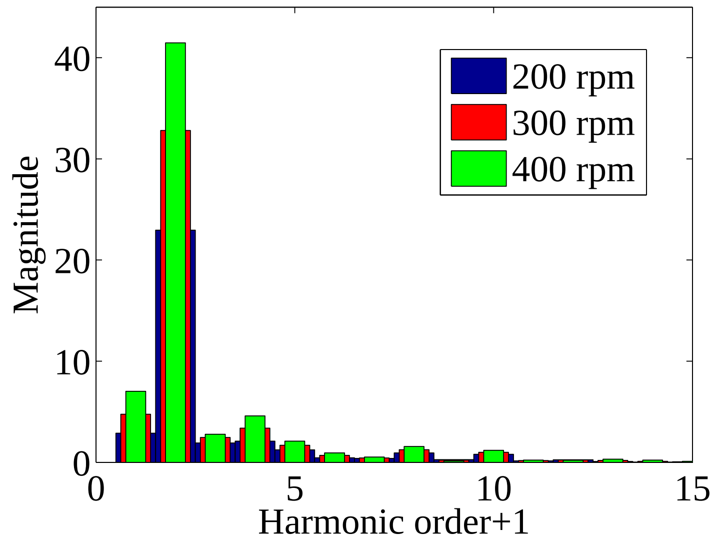

Figure 7.7: Harmonic Spectrum of Open-Circuit Voltage in Single-layer $\frac{2}{5}$SPP Permanent Magnet Synchronous Machine with Insulation Degraded Across 20% of Turns in a Slot

Machine Design	Machine Condition			
		Number in Slot Short-Circuited		
	Healthy	Single-Turn	10% Turns	20% Turns
Double-layer $\frac{1}{2}$ SPP	18.18%	19.5%	19.67%	20.55%
Single-layer $\frac{2}{5}$ SPP	30.21%	31.29%	31.4%	32.17%

Table 7.1: Torque Ripple in PM Machines Designed with Fractional Slot Concentrated Windings with Degraded Insulation (As a Percentage of the Average Torque of a Healthy Machine).

7.2 Experimental Setup and Results

It is observed in [39] that the location of the shorted turn in the slot affects the magnitude of the circulating current. It was shown that shorted turns nearest the slot opening develop the highest short-circuit current. For this reason, the windings of the double-layer $\frac{1}{2}$ and single-layer $\frac{2}{5}$ slot per pole per phase permanent magnet machines were designed to allow for

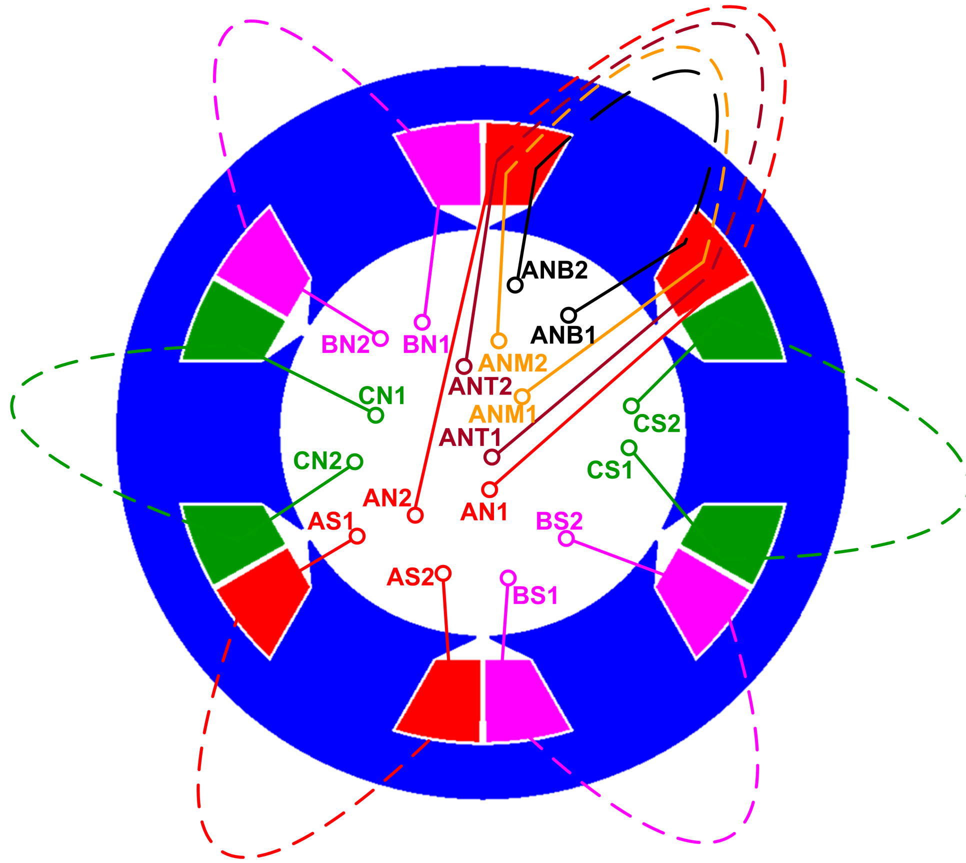

Figure 7.8: Winding Schematic of Double-layer $\frac{1}{2}$SPP PM Machine Prototype

introducing faults of varying severity in a slot nearest the air gap, as shown in Figures 7.8 and 7.9,respectively. The leads of several turns are separate coils brought out of the housing to allow the introduction of a single-turn fault, a fault involving 10% of the turns in the slot and a fault involving 20% of the turns in the slot.

The resistance of a single turn of the winding for each design was estimated using Equations (7.1) and (7.2) where ρ is the resistivity of copper, L is the length of a turn (estimated using the machine geometry) and A is the estimated cross-section of the wire. Both stators were wound with 4 parallel 22AWG wires. The resistance of a turn for both machine designs is shown in Table 7.2.

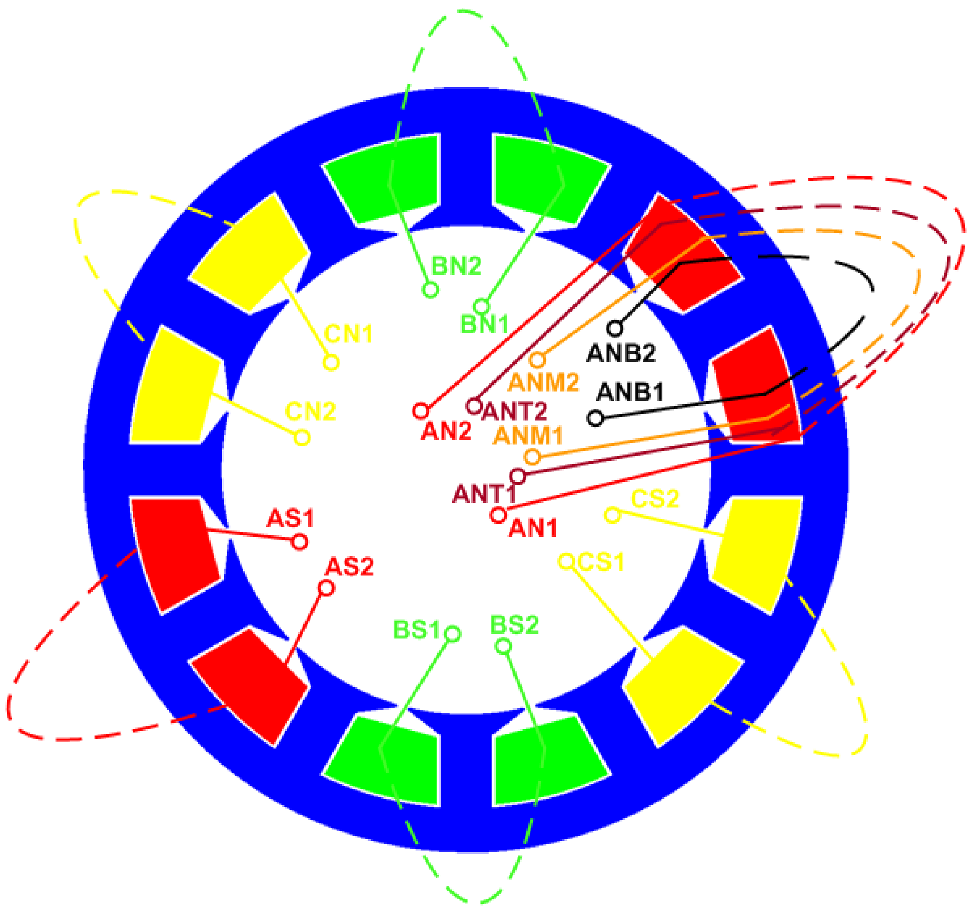

Figure 7.9: Winding Schematic of Single-layer $\frac{2}{5}$SPP PM Machine Prototype.

Machine Design	Turn Resistance
Double-layer $\frac{1}{2}$ SPP	3.7mΩ
Single-layer $\frac{2}{5}$ SPP	3.06mΩ

Table 7.2: Resistance of a Single Turn for Both Machine Designs

$$R_{wire} = \frac{\rho L}{A} \tag{7.1}$$

$$R_{turn} = \frac{R_{wire}}{4} \tag{7.2}$$

Varying the number of turns involved in the fault is accomplished by connecting a resistor, as shown in Figure 7.10. The level of insulation degradation is controlled by the value of the resistor connected. The experimental setup used to characterize the machines with insulation degradation is shown in Figure 7.11. The insulation degradation connector includes a LEM current transducer for monitoring the circulating current due to the fault on the oscilloscope.

The experimental procedure described in Section 4.4.2 is repeated for both machines under various inter-turn fault conditions. Both a $\frac{1}{2}\Omega$ and $\frac{1}{4}\Omega$ resistor are used to simulate insulation degradation. The experimental data processing method described in Section 4.4.3 is modified slightly. It was shown in Sections 4.6 and 7.1 that the open-circuit voltage is affected by circulating current due to the fault so the permanent magnet flux is not calculated from the open-circuit voltage in the faulty cases. The permanent magnet flux calculated with the healthy machine acquired data instead.

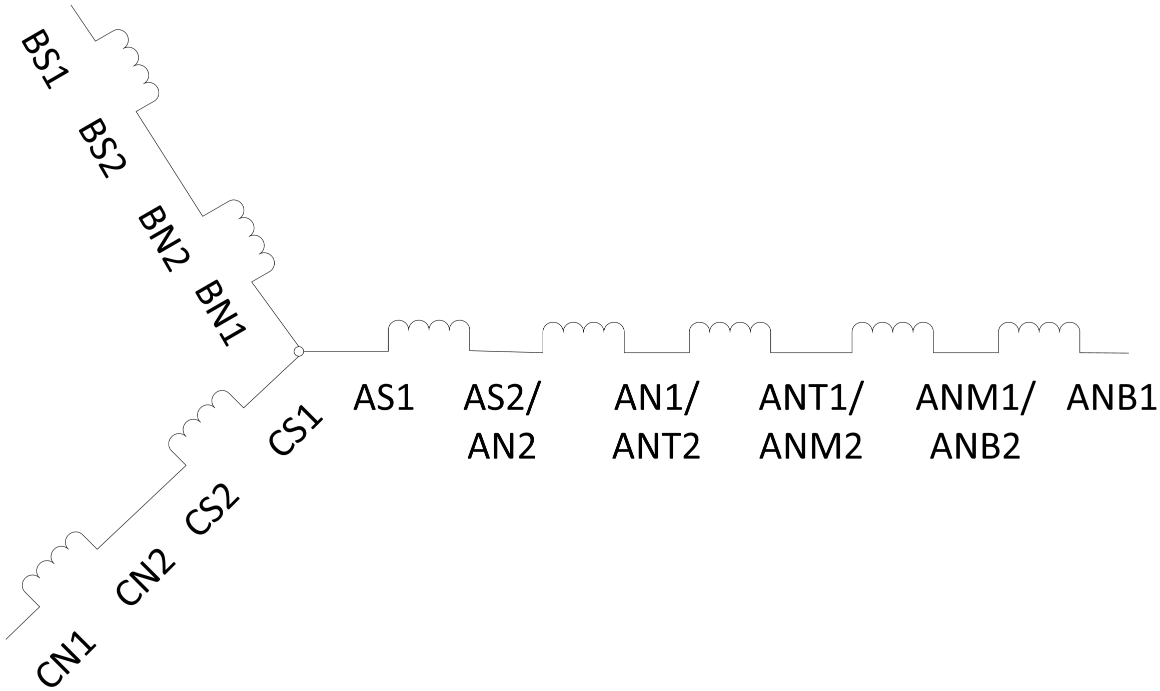

Figure 7.10: Circuit Diagram for Introducing Faults of Varying Severity

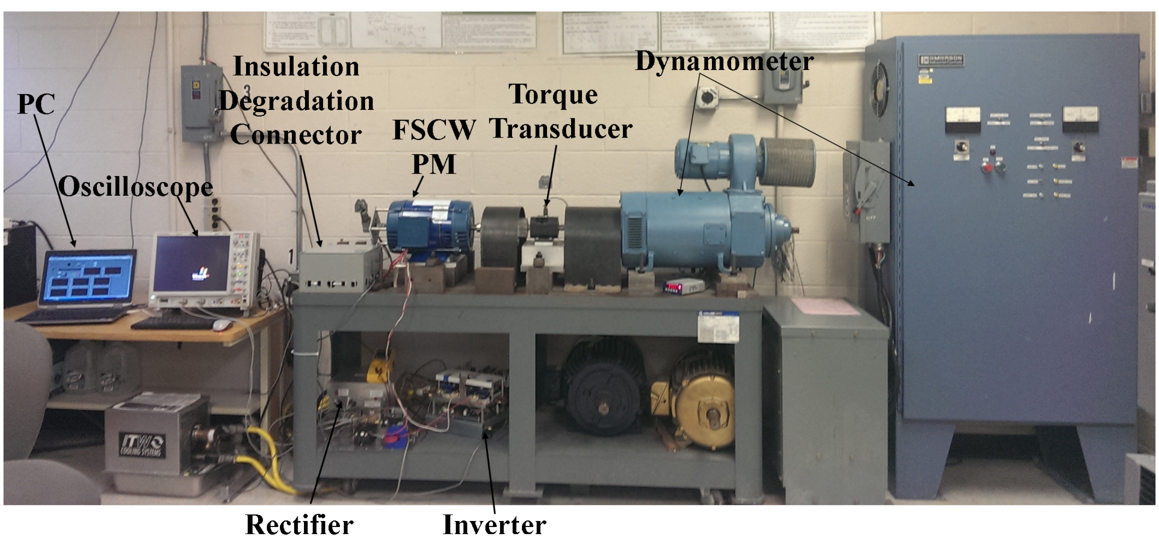

Figure 7.11: Experimental Setup

The circulating current and resulting flux linkages for the double-layer $\frac{1}{2}$ and single-layer $\frac{2}{5}$ slot per pole per phase machine varying the number of turns with degraded insulation were evaluated. As indicated by finite element analysis, circulating current is a function of the number of turns with degraded insulation and the machine speed.

It is shown in Figures 7.12 to 7.23 that the insulation degradation was reflected in the extracted flux linkages. The effects of saturation in the d- and q-axis flux linkages of the double-layer $\frac{1}{2}$ slot per pole per phase machine change as the insulation of more turns degrade. Insulation degradation in the single-layer $\frac{2}{5}$ slot per pole per phase machine also affects saturation in both the d- and q-axis flux linkages. The resulting flux linkages reveal a means for early detection of incipient stator inter-turn faults.

7.3 Online Detection of Winding Insulation Degradation

The parametric changes due to degrading winding insulation result in variations in the estimated voltage. The $\frac{1}{2}$ slot per pole per phase design voltage variations, in an electrical cycle, observed in finite element are shown in Figure 7.24. Voltage variations in an electrical cycle for the $\frac{2}{5}$ slot per pole per phase design are shown in Figure 7.25. The changes due to the insulation on a single-turn degrading doesn't vary much from the healthy voltage; however, this is a result of the low value of circulating current.

Degrading insulation leads to variations in the machine characteristic parameters; the flux

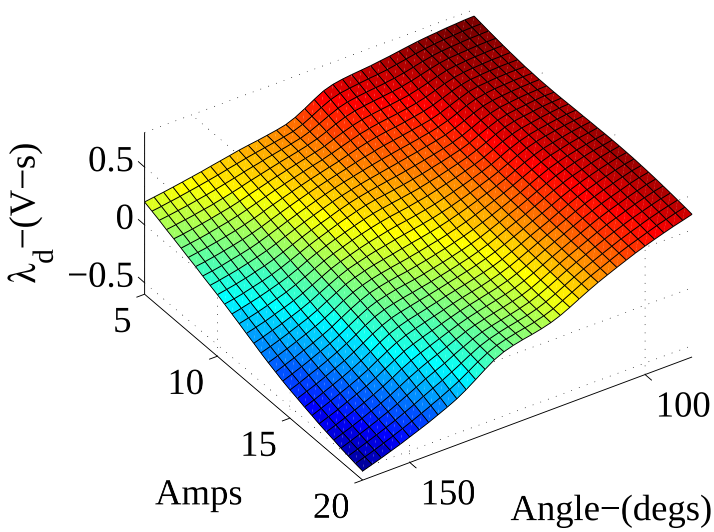

(a) d-axis

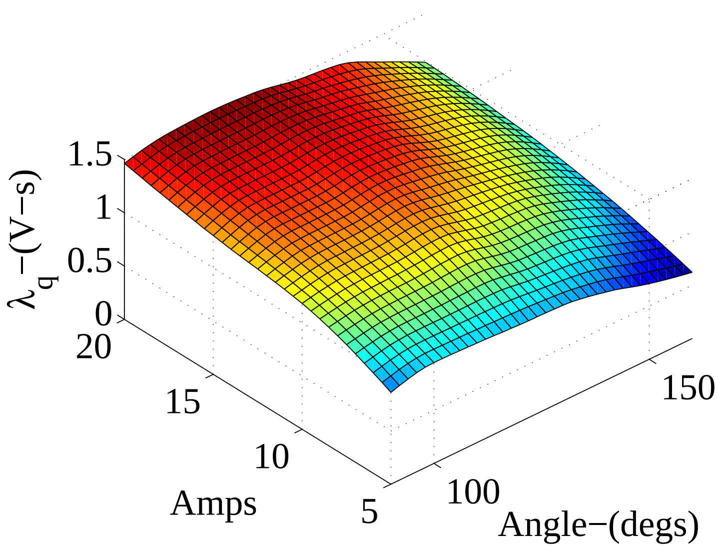

(b) q-axis

Figure 7.12: Double-layer $\frac{1}{2}$ SPP PM Machine with Insulation on a Single-turn Degraded($\frac{1}{2}\Omega$) (experimental results).

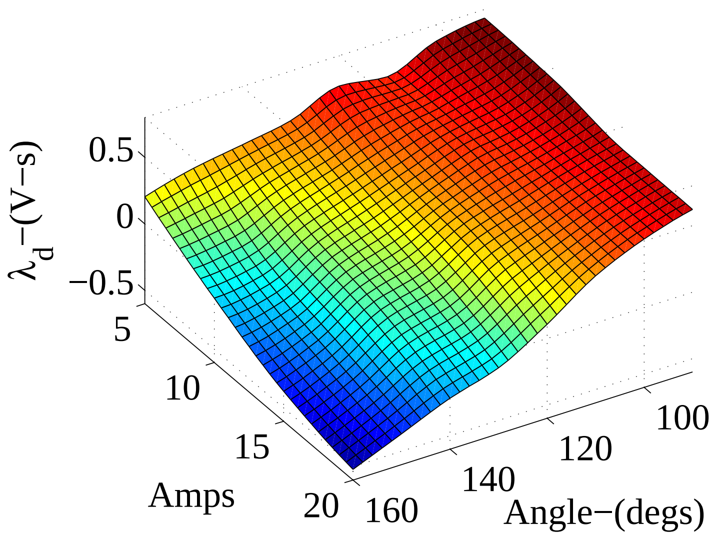

(a) d-axis

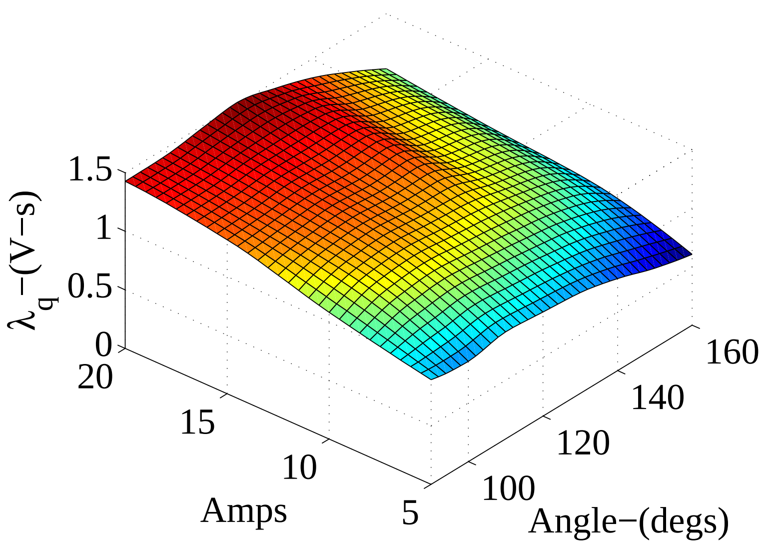

(b) q-axis

Figure 7.13: Double-layer $\frac{1}{2}$ SPP PM Machine with Insulation on a Single-turn Degraded($\frac{1}{4}\Omega$) (experimental results).

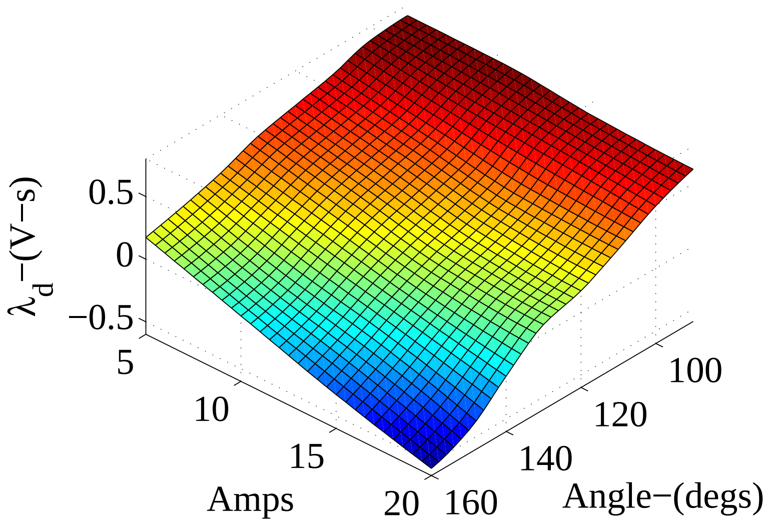

(a) d-axis

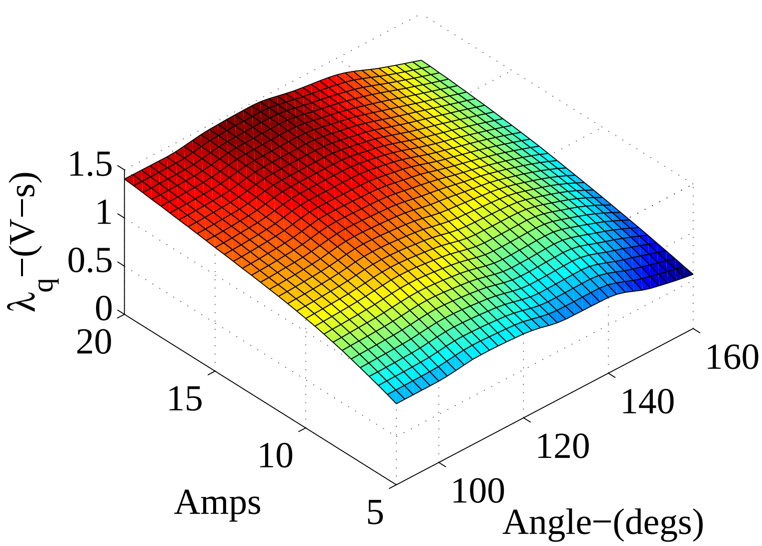

(b) q-axis

Figure 7.14: Double-layer $\frac{1}{2}$ SPP PM Machine with Insulation on 10% of turns in a slot Degraded($\frac{1}{2}\Omega$) (experimental results).

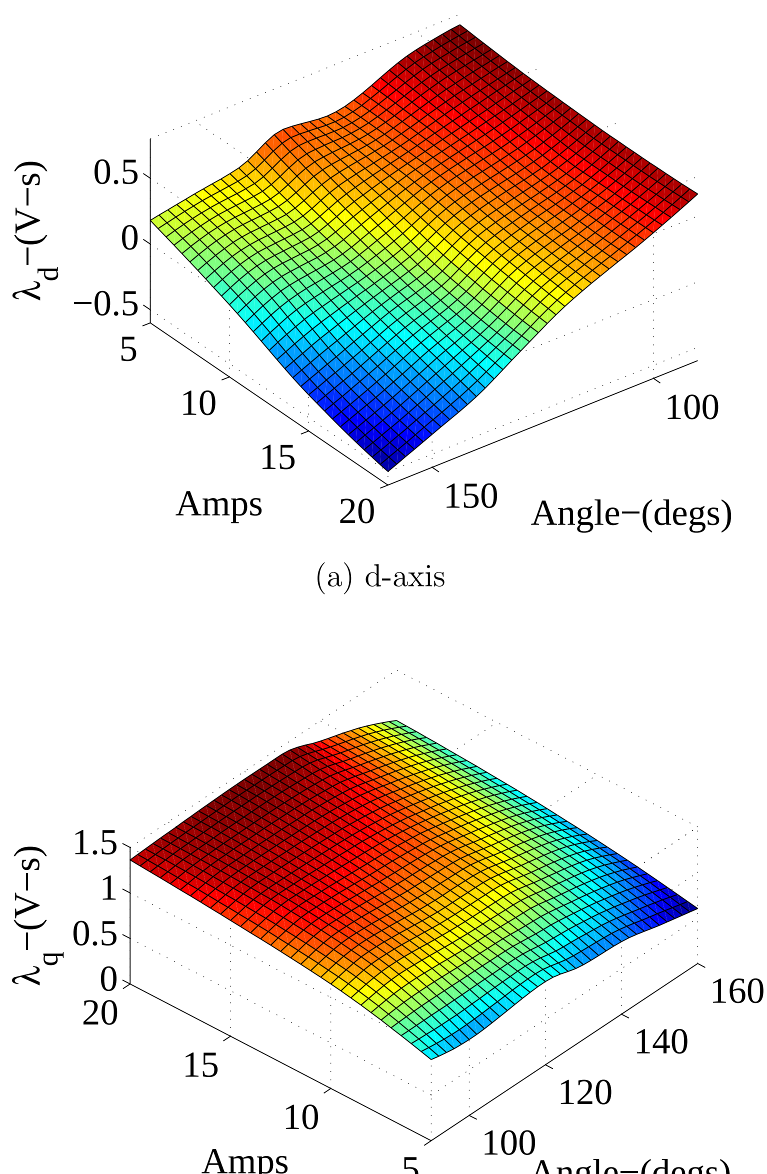

(a) d-axis

(b) q-axis

Figure 7.15: Double-layer $\frac{1}{2}$ SPP PM Machine with Insulation on 10% of turns in a slot Degraded($\frac{1}{4}\Omega$) (experimental results).

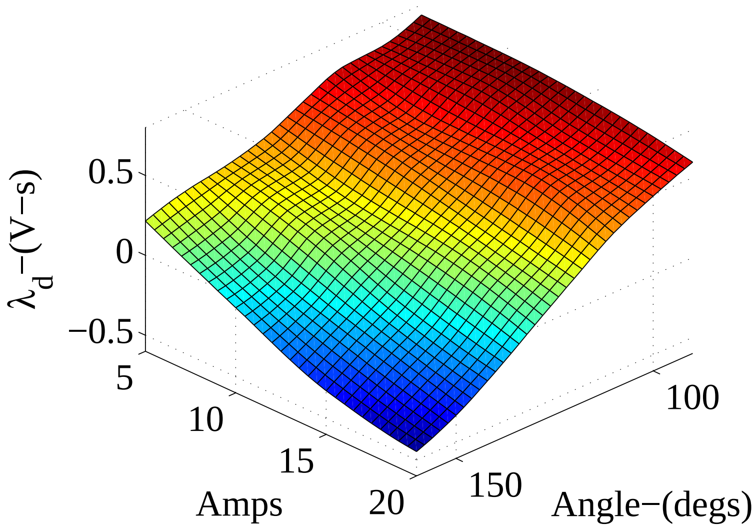

(a) d-axis

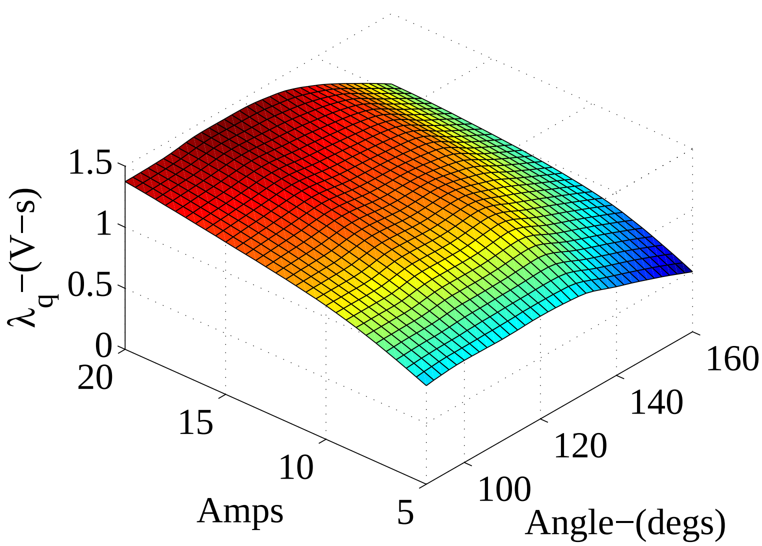

(b) q-axis

Figure 7.16: Double-layer $\frac{1}{2}$ SPP PM Machine with Insulation on 20% of turns in a slot Degraded($\frac{1}{2}\Omega$) (experimental results).

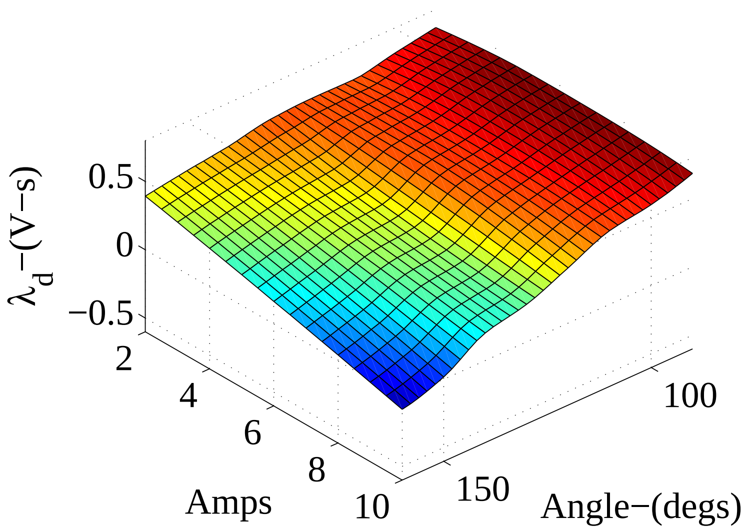

(a) d-axis

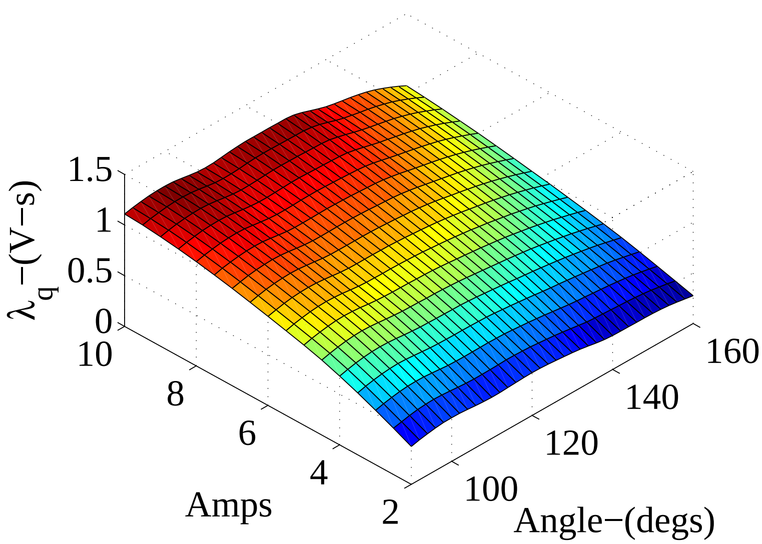

(b) q-axis

Figure 7.17: Double-layer $\frac{1}{2}$ SPP PM Machine with Insulation on 20% of turns in a slot Degraded($\frac{1}{4}\Omega$) (experimental results).

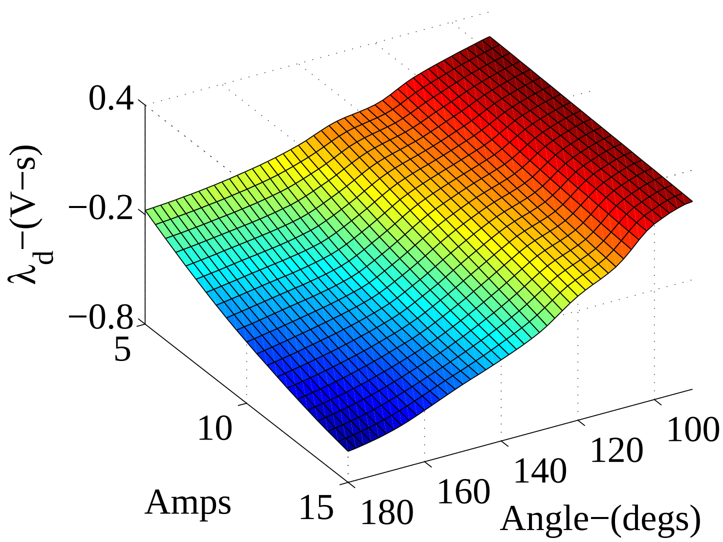

(a) d-axis

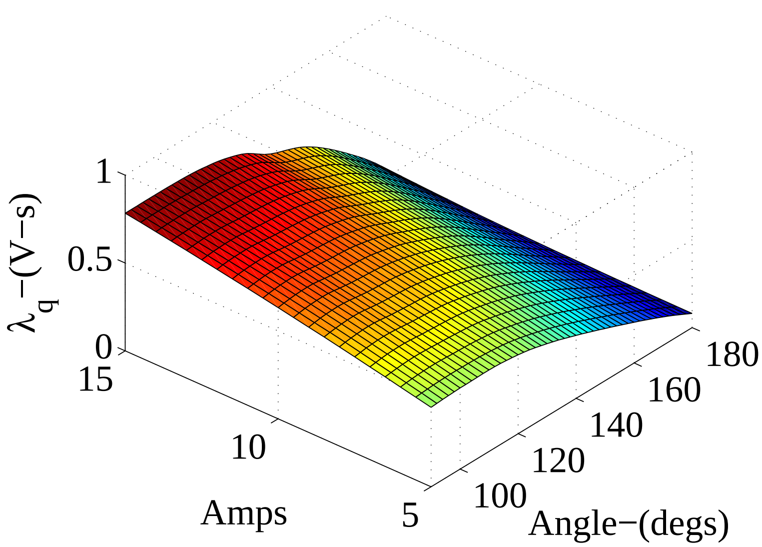

(b) q-axis

Figure 7.18: Single-layer $\frac{2}{5}$ SPP PM Machine with Insulation on a Single-turn Degraded($\frac{1}{2}\Omega$) (experimental results).

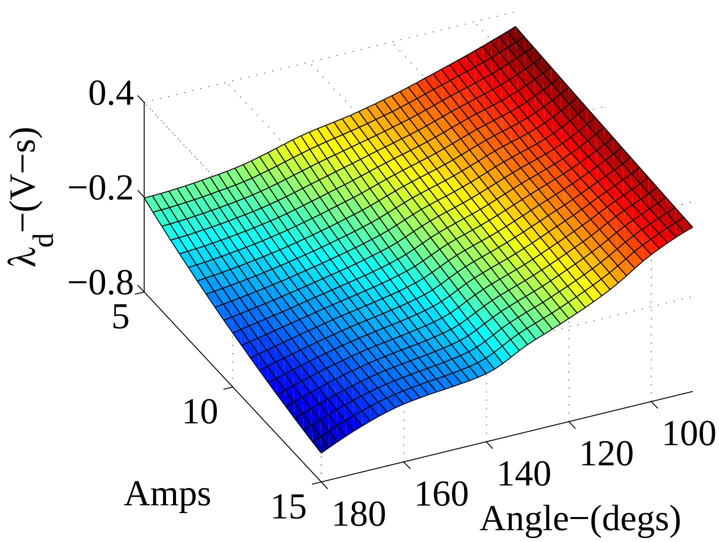

(a) d-axis

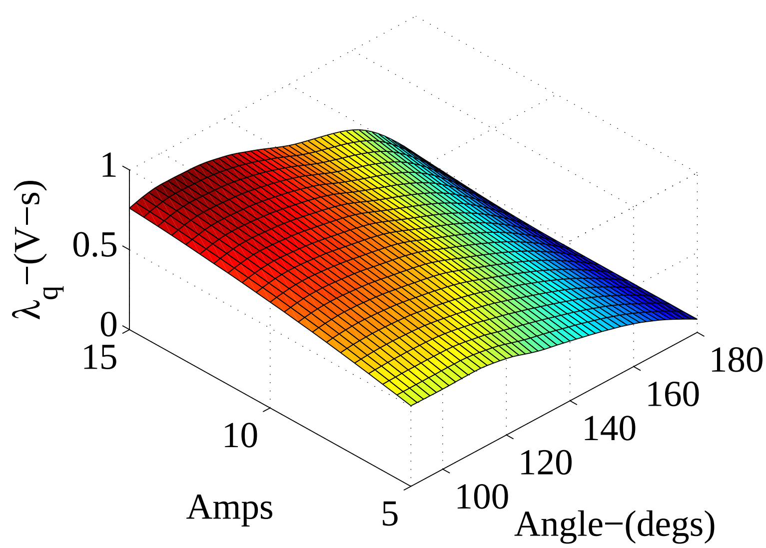

(b) q-axis

Figure 7.19: Single-layer $\frac{2}{5}$ SPP PM Machine with Insulation on a Single-turn Degraded($\frac{1}{4}\Omega$) (experimental results).

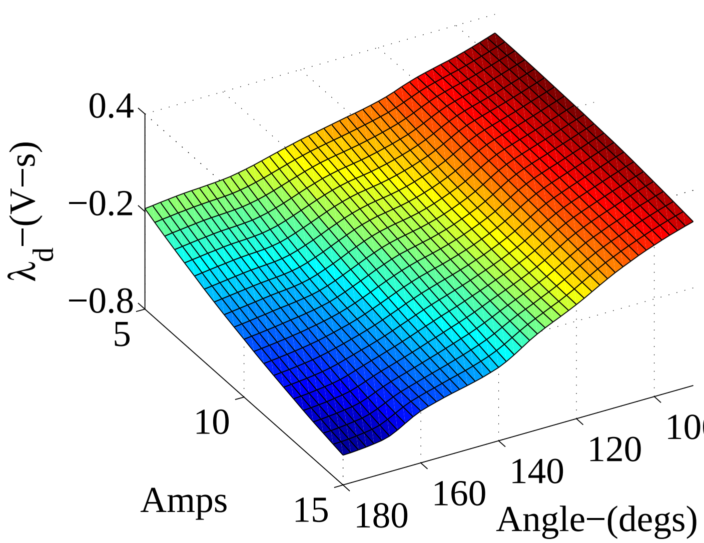

(a) d-axis

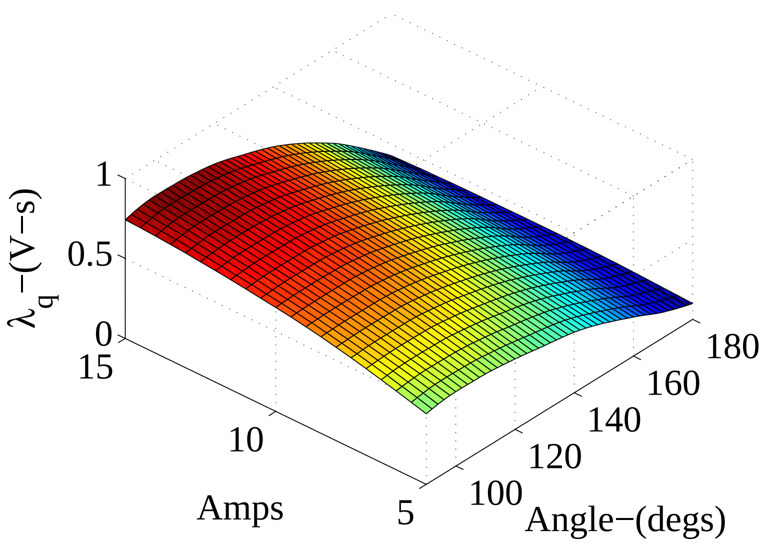

(b) q-axis

Figure 7.20: Single-layer $\frac{2}{5}$ SPP PM Machine with Insulation on 10% of turns in a slot Degraded($\frac{1}{2}\Omega$) (experimental results).

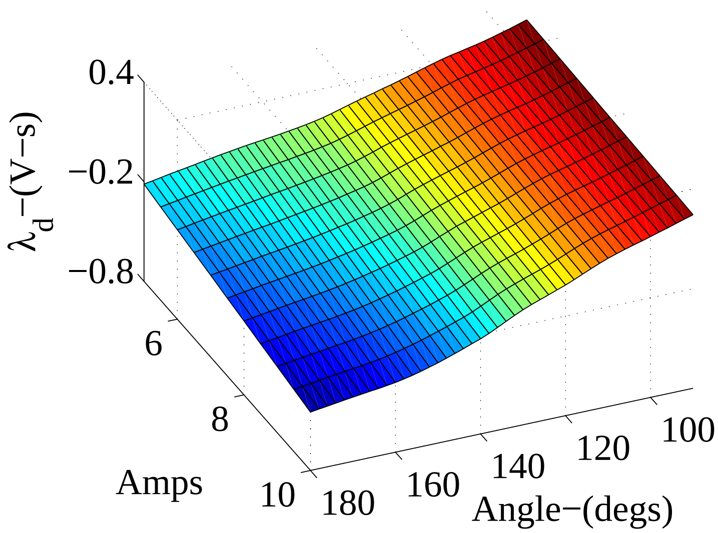

(a) d-axis

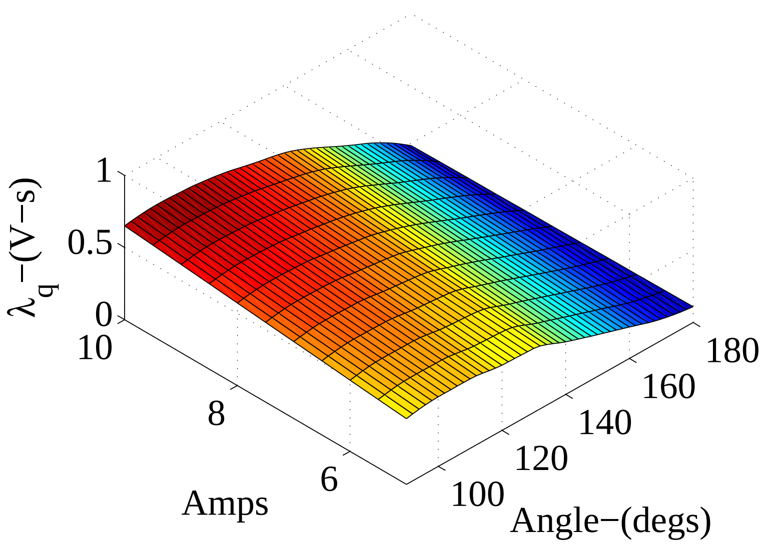

(b) q-axis

Figure 7.21: Single-layer $\frac{2}{5}$ SPP PM Machine with Insulation on 10% of turns in a slot Degraded($\frac{1}{4}\Omega$) (experimental results).

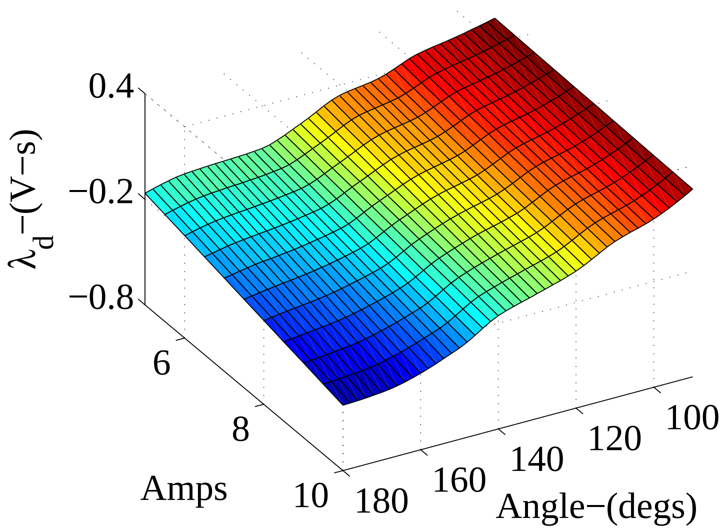

(a) d-axis

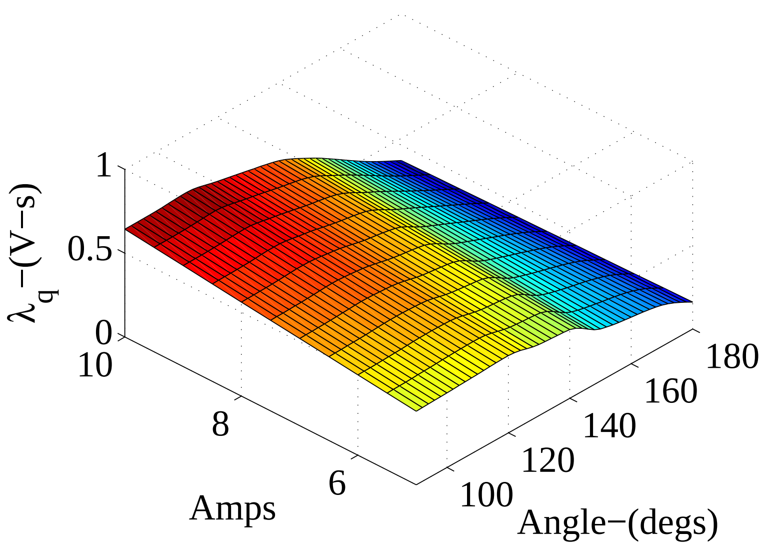

(b) q-axis

Figure 7.22: Single-layer $\frac{2}{5}$ SPP PM Machine with Insulation on 20% of turns in a slot Degraded($\frac{1}{2}\Omega$) (experimental results).

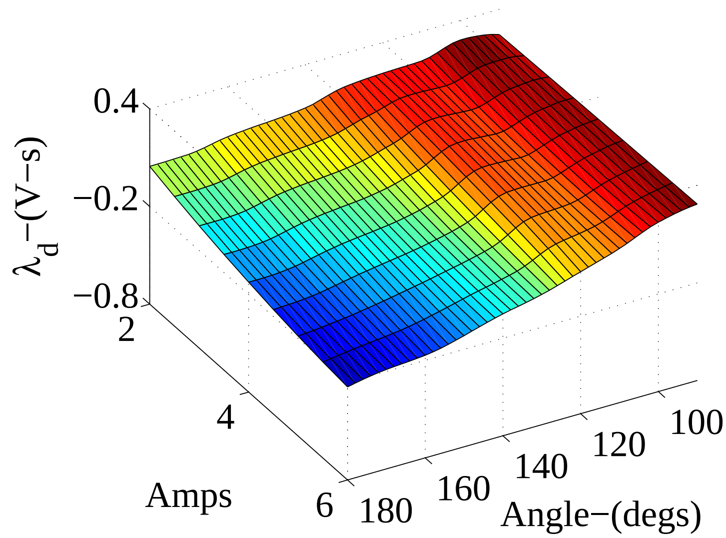

(a) d-axis

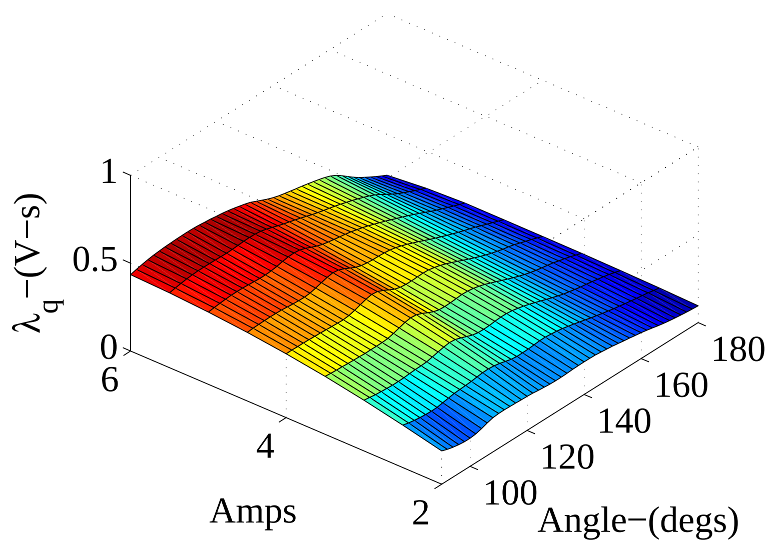

(b) q-axis

Figure 7.23: Single-layer $\frac{2}{5}$ SPP PM Machine with Insulation on 20% of turns in a slot Degraded($\frac{1}{4}\Omega$) (experimental results).

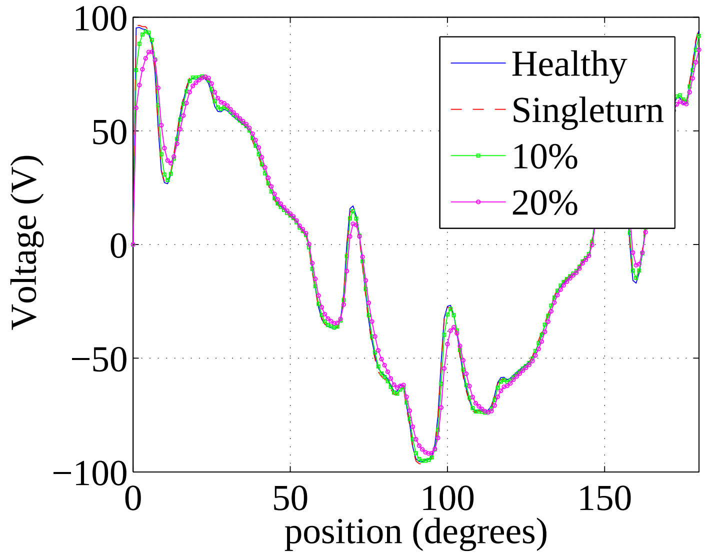

Figure 7.24: Phase voltage of Double-layer $\frac{1}{2}$ SPP PM Machine with Varying Number of Turns Having Degraded Insulation from Finite Element Simulation.

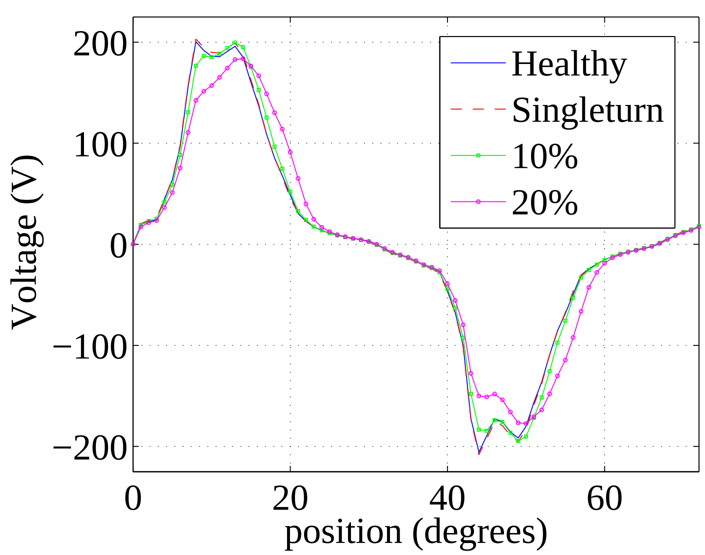

Figure 7.25: Phase voltage of Single-layer $\frac{2}{5}$ SPP PM Machine with Varying Number of Turns Having Degraded Insulation from Finite Element Simulation.

linkages will change as the fault progresses. It is well known that the use of accurate machine parameters for control improves a machine's operating performance. Accurate knowledge of the parameters is useful for more than control. Monitoring the condition of the winding insulation can be accomplished online, if accurate knowledge of the machine parameters is available. The machine model populated with accurate parameters together with measured phase currents and machine speed provide voltage estimates, Equations (4.35) and (4.36). Circulating current in windings with degraded insulation affect the machine parameters, which will be reflected in the voltage estimations. The ability to detect that the winding insulation is degrading during machine operation offers opportunity to mitigate the fault and avoid machine failure, thereby increase machine reliability. Additionally, early detection of winding insulation deterioration should reduce the occurrence of secondary faults and provide opportunity for planned maintenance.

Chapter 8

Conclusion

Fractional slot concentrated windings can be designed to provide thermal, magnetic and physical isolation between phases; however, machine performance is a direct trade-off. Single-layer fractional slot concentrated windings provide the best isolation between phases; however, the inherent characteristics of this design negatively impacts the torque performance, due to the high ripple. In this work, a torque ripple compensation technique was developed to improve the torque performance of this reliable design.

An analytical torque expression was developed in this work. The resulting torque expression was divided into DC and ripple components. The ripple component was used as an a priori estimator of torque ripple calculated from the current command and rotor position. The estimated torque ripple was used to modify the torque command effectively decreasing the ripple torque contributed by the harmonic of the rotor MMF with highest magnitude. Finite element results demonstrated that the torque ripple can be decreased by as much as 70% with the technique. It was shown that the ripple compensation technique increases the machine losses, affecting efficiency. At high torque, the magnet losses increase by as much as 15%. The model-based controller used in this work was populated with parameters that only include the self-saturation effect. Additionally, both self- and cross-saturation were neglected in the torque ripple estimator.

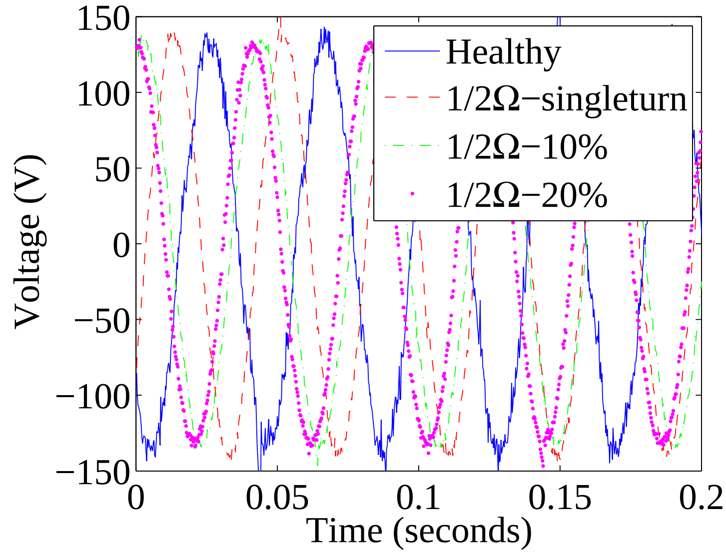

Figure 8.1: Experimental Voltage Estimate for Single-layer $\frac{2}{5}$ SPP PM Machine Applying a $15A@120^{\circ}$ Current Command

Designing a machine with magnetic, thermal and physical isolation of the phases does not guarantee that the winding insulation will not wear. Increased machine reliability is gained by monitoring the condition of the winding insulation during operation. Circulating current begins to flow in the windings with worn insulation before the presence of a short-circuit. The circulating current affects the machine characteristic parameters. In this work, insulation degradation was introduced experimentally with a resistor to two permanent magnet machines with fractional slot concentrated windings. Experimental results demonstrated changes in the characteristic flux linkages due to winding degradation. Finite element results showed that these changes are reflected in the machine voltage. The number of turns with degraded insulation affects the shape of the machine voltage. Voltage variations, due to degraded winding insulation, are not easily observed in the experimental voltage estimates, as demonstrated in Figure 8.1.

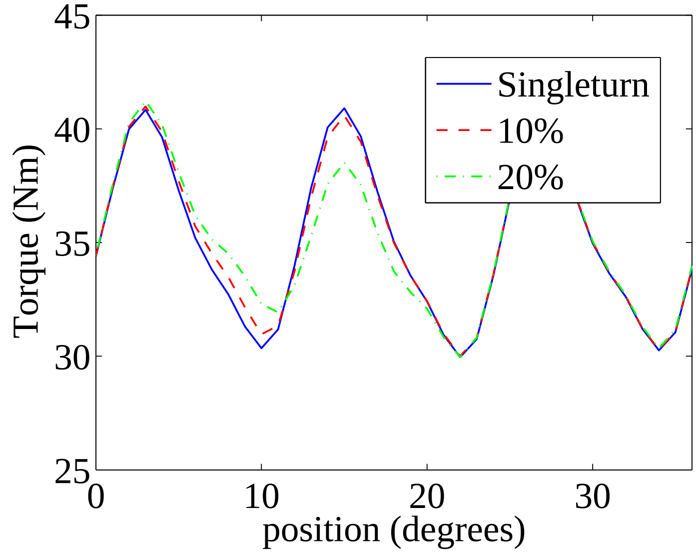

Figure 8.2: Finite Element Torque for Single-layer $\frac{2}{5}$ SPP PM Machine with incipient faults

The incipient fault in finite element is placed in phase a and physically located in the slot between 4.87° and 25.12°. The machine torque reduces near the fault location, as shown in Figure 8.2.

Permanent magnet synchronous machines equipped with single-layer fractional slot windings provide low possibility of failure. Of the machine designs evaluated in this work, the single-layer design has the lowest value of circulating current in the event of stator winding failure. The torque performance of this machine design is improved with the ripple compensation technique presented in this work. Prior to stator winding failure, the machine characteristic parameters change as a result of incipient faults. These parametric changes are reflected in the machine voltages and can be used to detect pending failures online, allowing for timely maintenance and repair.

Future work will demonstrate the use of experimental voltage estimates to detect incipient faults in the fault tolerant machines designed with fractional slot concentrated windings. Additionally, methods for accurately identifying the fault location and improving the performance of the torque ripple compensation technique over the machine's entire range of operation.

Self- and cross-saturation are non-linear effects that have been proven important for development of high performance permanent magnet synchronous machine controllers. These effects will be included in both the model-based controller and the torque ripple estimator.

During the parametric identification process for the $\frac{1}{2}$ slot per pole per phase permanent magnet machine, acoustic noise was noted when applying high d-axis current, angles close to 180°. Once the insulation of the winding was degraded, the acoustic noise was noted earlier, as the number of turns with degraded insulation increased. Acoustic noise was also noted when applying high d-axis current to the $\frac{2}{5}$ slot per pole per phase machine with incipient stator faults. Future work will explore the relationship between the angle of the applied current and the acoustic noise, as well as its relation to insulation degradation.

BIBLIOGRAPHY

BIBLIOGRAPHY

[1] J. Nandan and R. Gobbi, "High reliability for electric machines driving critical loads: A review," in *Applied Power Electronics Colloquium (IAPEC), 2011 IEEE*, 2011, pp. 132–137.

[2] P. Nussbaumer, A. Mitteregger, and T. Wolbank, "Detecting changes of the insulation state of variable speed drive systems based on inverter-built-in current sensors," in *Power Electronics, Electrical Drives, Automation and Motion (SPEEDAM), 2012 International Symposium on*, 2012, pp. 1017–1022.

[3] M. Shah, A. EL-Refaie, and K. Sivasubramaniam, "Analysis of turn-to-turn faults in surface pm machines with multi-layer fractional-slot concentrated windings," in *Electrical Machines, 2008. ICEM 2008. 18th International Conference on*, 2008, pp. 1–4.

[4] F. Meier and J. Soulard, "dq theory applied to a permanent magnet synchronous machine with concentrated windings," in *Power Electronics, Machines and Drives, 2008. PEMD 2008. 4th IET Conference on*, 2008, pp. 194–198.

[5] Z. Aza, Z. Q. Zhu, and G. Ombach, "Torque-speed performance analysis of fractional slot pm machines having concentrated windings using alternate methods," in *Power Electronics, Machines and Drives (PEMD 2012), 6th IET International Conference on*, 2012, pp. 1–6.

[6] S. Nandi and H. Toliyat, "Condition monitoring and fault diagnosis of electrical machines-a review," in *Industry Applications Conference, 1999. Thirty-Fourth IAS Annual Meeting. Conference Record of the 1999 IEEE*, vol. 1, 1999, pp. 197–204 vol.1.

[7] A. Djerdir, J. Farooq, A. Rezig, and A. Miraoui, "Faults in permanent magnet traction motors: state of the art and modelling approaches," in *Power and Energy Society General Meeting, 2010 IEEE*, 2010, pp. 1–5.

[8] "Report of large motor reliability survey of industrial and commercial installations, part ii," *Industry Applications, IEEE Transactions on*, vol. IA-21, no. 4, pp. 865–872, 1985.

[9] L. Romeral, J. Urresty, J.-R. Riba Ruiz, and A. Garcia Espinosa, "Modeling of surface-mounted permanent magnet synchronous motors with stator winding interturn faults," *Industrial Electronics, IEEE Transactions on*, vol. 58, no. 5, pp. 1576–1585, 2011.

[10] Y. Lee and T. Habetler, "A phase variable simulation model for interior pm synchronous motor drives with stator turn faults," in *Power Electronics and Motion Control Conference, 2006. EPE-PEMC 2006. 12th International*, 2006, pp. 1074–1079.

[11] B. Vaseghi, B. Nahid-Mobarakeh, N. Takorabet, and F. Meibody-Tabar, "Experimentally validated dynamic fault model for pmsm with stator winding inter-turn fault," in *Industry Applications Society Annual Meeting, 2008. IAS '08. IEEE*, 2008, pp. 1–5.

[12] B.-G. Gu, J.-H. Choi, and I.-S. Jung, "A dynamic modeling and a fault detection scheme of a pmsm under an inter turn short," in *Vehicle Power and Propulsion Conference (VPPC), 2012 IEEE*, 2012, pp. 1074–1080.

[13] B. Mecrow, A. Jack, J. Haylock, and J. Coles, "Fault-tolerant permanent magnet machine drives," *Electric Power Applications, IEE Proceedings* -, vol. 143, no. 6, pp. 437–442, 1996.

[14] M. Abolhassani and H. Toliyat, "Fault tolerant permanent magnet motor drives for electric vehicles," in *Electric Machines and Drives Conference, 2009. IEMDC '09. IEEE International*, 2009, pp. 1146–1152.

[15] A. Jack, B. Mecrow, and J. Haylock, "A comparative study of permanent magnet and switched reluctance motors for high-performance fault-tolerant applications," *Industry Applications, IEEE Transactions on*, vol. 32, no. 4, pp. 889–895, 1996.

[16] B. McCrow, A. Jack, D. Atkinson, and J. Haylock, "Fault tolerant drives for safety critical applications," in *New Topologies for Permanent Magnet Machines (Digest No: 1997/090), IEE Colloquium on*, 1997, pp. 5/1–5/7.

[17] D. Fodorean, M. Ruba, D.-C. Popa, and A. Miraoui, "Fault tolerant permanent magnet machines used in automobile applications," in *Electrical Machines (ICEM), 2010 XIX International Conference on*, 2010, pp. 1–6.

[18] M. Villani, M. Tursini, G. Fabri, and L. Castellini, "High reliability permanent magnet brushless motor drive for aircraft application," *Industrial Electronics, IEEE Transactions on*, vol. 59, no. 5, pp. 2073–2081, 2012.

[19] N. Bianchi, S. Bolognani, and M. Pre, "Impact of stator winding of a five-phase permanent-magnet motor on postfault operations," *Industrial Electronics, IEEE Transactions on*, vol. 55, no. 5, pp. 1978–1987, 2008.

[20] L. Parsa and H. Toliyat, "Fault-tolerant interior-permanent-magnet machines for hybrid electric vehicle applications," *Vehicular Technology, IEEE Transactions on*, vol. 56, no. 4, pp. 1546–1552, 2007.

[21] C. Gerada, K. Bradley, and M. Summer, "Winding turn-to-turn faults in permanent magnet synchronous machine drives," in *Industry Applications Conference, 2005. Fourtieth IAS Annual Meeting. Conference Record of the 2005*, vol. 2, 2005, pp. 1029–1036 Vol. 2.

[22] A. EL-Refaie, "Fractional-slot concentrated-windings synchronous permanent magnet machines: Opportunities and challenges," *Industrial Electronics, IEEE Transactions on*, vol. 57, no. 1, pp. 107–121, 2010.

[23] N. Bianchi, M. Pre, G. Grezzani, and S. Bolognani, "Design considerations on fractional-slot fault-tolerant synchronous motors," in *Electric Machines and Drives, 2005 IEEE International Conference on*, 2005, pp. 902–909.

[24] J. Tangudu, T. Jahns, and A. El-Refaie, "Unsaturated and saturated saliency trends in fractional-slot concentrated-winding interior permanent magnet machines," in *Energy Conversion Congress and Exposition (ECCE), 2010 IEEE*, 2010, pp. 1082–1089.

[25] J. Pyrhonen, T. Jokinen, and V. Hrbovocova, *Design of Rotating Electrical Machines.* Wiley, 2008.

[26] R. Dutta, M. F. Rahman, and L. Chong, "Winding inductances of an interior permanent magnet (ipm) machine with fractional slot concentrated winding," *Magnetics, IEEE Transactions on*, vol. 48, no. 12, pp. 4842–4849, 2012.

[27] F. Magnussen and C. Sadarangani, "Winding factors and joule losses of permanent magnet machines with concentrated windings," in *Electric Machines and Drives Conference, 2003. IEMDC'03. IEEE International*, vol. 1, 2003, pp. 333–339 vol.1.

[28] N. Bianchi, S. Bolognani, and E. Fornasiero, "An overview of rotor losses determination in three-phase fractional-slot pm machines," *Industry Applications, IEEE Transactions on*, vol. 46, no. 6, pp. 2338–2345, 2010.

[29] M. Barcaro, N. Bianchi, and F. Magnussen, "Remarks on torque estimation accuracy in fractional-slot permanent-magnet motors," *Industrial Electronics, IEEE Transactions on*, vol. 59, no. 6, pp. 2565–2572, 2012.

[30] G. Dajaku and D. Gerling, "Different novel methods for reduction of low space harmonics for the fractional slot concentrated windings," in *Electrical Machines and Systems (ICEMS), 2012 15th International Conference on*, 2012, pp. 1–6.

[31] P. Reddy, K.-K. Huh, and A. El-Refaie, "Effect of stator shifting on harmonic cancellation and flux weakening performance of interior pm machines equipped with fractional-slot concentrated windings for hybrid traction applications," in *Energy Conversion Congress and Exposition (ECCE), 2012 IEEE*, 2012, pp. 525–533.

[32] S.-H. Han, T. Jahns, and W. Soong, "Torque ripple reduction in interior permanent magnet synchronous machines using the principle of mutual harmonics exclusion," in *Industry Applications Conference, 2007. 42nd IAS Annual Meeting. Conference Record of the 2007 IEEE*, 2007, pp. 558–565.

[33] G. Pellegrino, P. Guglielmi, A. Vagati, and F. Villata, "Core losses and torque ripple in ipm machines: Dedicated modeling and design tradeoff," *Industry Applications, IEEE Transactions on*, vol. 46, no. 6, pp. 2381–2391, 2010.

[34] S. Lee, Y.-J. Kim, and S.-Y. Jung, "Numerical investigation on torque harmonics reduction of interior pm synchronous motor with concentrated winding," *Magnetics, IEEE Transactions on*, vol. 48, no. 2, pp. 927–930, 2012.

[35] N. Bianchi, M. Dai Pre, L. Alberti, and E. Fornasiero, *Theory and Design of Fractional-Slot PM Machines*. Sponsored by the IEEE-IAS Electrical Machines Commitee, Ed. Padova: CLEUP (ISBN 978-88-6129-122-5), 2007.

[36] Y. Lee and T. Habetler, "An on-line stator turn fault detection method for interior pm synchronous motor drives," in *Applied Power Electronics Conference, APEC 2007 - Twenty Second Annual IEEE*, 2007, pp. 825–831.

[37] A. Gandhi, T. Corrigan, and L. Parsa, "Recent advances in modeling and online detection of stator interturn faults in electrical motors," *Industrial Electronics, IEEE Transactions on*, vol. 58, no. 5, pp. 1564–1575, 2011.

[38] N. Leboeuf, T. Boileau, B. Nahid-Mobarakeh, N. Takorabet, F. Meibody-Tabar, and G. Clerc, "Inductance calculations in permanent-magnet motors under fault conditions," *Magnetics, IEEE Transactions on*, vol. 48, no. 10, pp. 2605–2616, 2012.

[39] P. Arumugam, T. Hamiti, and C. Gerada, "Fault tolerant winding design - a compromise between losses and fault tolerant capability," in *Electrical Machines (ICEM), 2012 XXth International Conference on*, 2012, pp. 2559–2565.

[40] K. Liu, Z. Zhu, and D. Stone, "Parameter estimation for condition monitoring of pmsm stator winding and rotor permanent magnets," *Industrial Electronics, IEEE Transactions on*, vol. 60, no. 12, pp. 5902–5913, 2013.

[41] M. Khov, J. Regnier, and J. Faucher, "Detection of turn short-circuit faults in stator of pmsm by on-line parameter estimation," in *Power Electronics, Electrical Drives, Automation and Motion, 2008. SPEEDAM 2008. International Symposium on*, 2008, pp. 161–166.

[42] W. Tang, G. Liu, and J. Ji, "Winding turn-to-turn faults detection of five-phase fault-tolerant permanent-magnet machine based on parametric model," in *Electrical Machines and Systems (ICEMS), 2012 15th International Conference on*, 2012, pp. 1–6.

[43] J. Cintron-Rivera, A. Babel, E. Montalvo-Ortiz, S. Foster, and E. Strangas, "A simplified characterization method including saturation effects for permanent magnet machines," in *Electrical Machines (ICEM), 2012 XXth International Conference on*, 2012, pp. 837–843.

[44] A. Babel, S. Foster, J. Cintron-Rivera, and E. Strangas, "Parametric sensitivity in the analysis and control of permanent magnet synchronous machines," in *Electrical Machines (ICEM), 2012 XXth International Conference on*, 2012, pp. 1034–1040.

[45] J. Haylock, B. Mecrow, A. Jack, and D. Atkinson, "Operation of fault tolerant machines with winding failures," *Energy Conversion, IEEE Transactions on*, vol. 14, no. 4, pp. 1490–1495, 1999.

[46] L. Zhu, S. Z. Jiang, Z. Zhu, and C. Chan, "Analysis and modeling of open-circuit airgap field distributions in multi-segment and multilayer interior permanent magnet machines," in *Vehicle Power and Propulsion Conference, 2008. VPPC '08. IEEE*, 2008, pp. 1–6.

[47] G. Dajaku and D. Gerling, "Determination of air-gap flux density due to magnets using the new analytical model," in *Electrical Machines (ICEM), 2010 XIX International Conference on*, 2010, pp. 1–6.

[48] G. Dajaku and D. Gerling, "Stator slotting effect on the magnetic field distribution of salient pole synchronous permanent-magnet machines," *Magnetics, IEEE Transactions on*, vol. 46, no. 9, pp. 3676–3683, 2010.